



Orbital Decay in Triaxial Shaped Dark Matter Haloes

Jalpesh Sachania

Submitted in total fulfilment of the requirements of the degree of
Doctor of Philosophy

October 2009

Theoretical Astrophysics Group
Department of Physics and Astronomy
The University of Leicester

UMI Number: U559403

All rights reserved

INFORMATION TO ALL USERS

The quality of this reproduction is dependent upon the quality of the copy submitted.

In the unlikely event that the author did not send a complete manuscript and there are missing pages, these will be noted. Also, if material had to be removed, a note will indicate the deletion.



UMI U559403

Published by ProQuest LLC 2013. Copyright in the Dissertation held by the Author.
Microform Edition © ProQuest LLC.

All rights reserved. This work is protected against
unauthorized copying under Title 17, United States Code.



ProQuest LLC
789 East Eisenhower Parkway
P.O. Box 1346
Ann Arbor, MI 48106-1346

Orbital Decay in Triaxial Shaped Dark Matter Haloes

by

Jalpesh Sachania

In cosmological simulations of structure formation of the universe, the dark matter halos in which galaxies are embedded in, are triaxial in shape. Simulations which focus in on galaxies in isolation do not use triaxial dark matter halos but use spherical shaped halos instead, as triaxial equilibrium models are hard to create.

Using a new method of creating initial conditions, which is able to create triaxial equilibrium models, the effect of using a triaxial halo in simulations of satellite accretion will be studied. In previous studies with a spherical shaped dark matter halo, the initial position of the satellite is unimportant due to the symmetry of the system, however in a triaxial halo this is not the case and the initial position becomes important. A study of the parameter space of the initial position and velocity of a satellite is undertaken and the orbital decay is compared in each case.

The different mergers will also have different effects upon the halo itself as the orbital energy of the satellite is transferred to the halo. The effects of a minor merger onto the halo is investigated and compared to the scenario more commonly used when the halo is spherical.

This study is then extended to find out whether the orbital decay in a triaxial potential, which can differ significantly from that in a spherical halo, can be used to explain the observations of polar ring galaxies and gas discs in elliptical galaxies.

Acknowledgements

I would like to thank the people that are most important to me, first and foremost my mum, dad and brother whom without I would not be the person I am today and without their support and encouragement I would not have gotten this far in my life. I'd like to thank my Vanisha, who has made my life complete and changed it in so many ways for the better. Also, my two sagaas Bharat and Dharam for giving me nothing but lip!

A big thank you to guys that I have shared an office in during my Ph.D. and made everyday different and enjoyable with all the lively banter flying around. In order of time spend along side from the start. Patrick - who suffered with me from the start, Lee - who knows it all, Alex - the orangeness never got old! Pete - our resident engineer, Fergus - for letting me get massive with him on so many occasions! Paul - my guide through the first stages of the Ph.D., Yohann, Dave, Emma, Matthew, Fabrizio. Others in the group who have helped me have a great time in the Ph.D., Dean, Jim, Martin, James, Andrew, Sergei, Giuseppe, Seung-Hoon, Andreas, Chris, Celine and David. To Lisa, for always having the time to have a gossip session! Also, those outside the group too, Mike, Matt, Rich, Andy, Jonny, and the rest of the physics guys that I played football and won championships in cricket with.

I would like to extend my deepest gratitude to Walter and Mark, whom without their supervision, knowledge, wisdom and patience; this thesis would not even exist.

Finally, big, big thank you to the legend that is Graham who is directly responsible for making my time at Leicester very enjoyable and offered much guidance when it was needed.

Contents

Abstract	i
Acknowledgements	ii
1 Introduction	1
1.1 Galaxies	2
1.2 Dark Matter in the Universe	4
1.2.1 Baryonic Dark Matter	6
1.2.2 Non-Baryonic Dark Matter Candidates	6
1.2.3 Cosmological Evidence	7
1.3 Cosmological Simulations of Dark Matter	9
1.3.1 Structure Formation in the Universe	9
1.4 Shapes of Dark Matter Haloes	12
1.4.1 Triaxial Haloes	13
1.4.2 Orbital Structure in Triaxial Potentials	14
1.5 Mergers of Galaxies	15
1.6 Dynamical Friction	17
1.7 Orbital Decay in Triaxial Haloes	18
2 Methods	20
2.1 Collisionless Systems	21
2.1.1 Relaxation Time	21
2.1.2 The Collisionless Boltzmann Equation	22
2.2 N -body Simulations	22
2.2.1 Force Calculation	23
2.3 Force Softening	24
2.3.1 Particle Based codes	24
2.4 Grid Based Codes	25
2.5 Self-Consistent Field	26
2.6 falcON	27
2.6.1 Approximating Gravity	27
2.7 gyrfalcON	29
2.8 Made to Measure N -body method	30
2.8.1 Dehnen’s Novel M2M Method	33

2.8.2	Creating Triaxial Initial Conditions	34
2.9	Analysis Methods	34
2.9.1	Orbital Analysis	34
2.9.2	Halo Profiles using Density	36
3	Orbital Decay of a Satellite Galaxy in a Triaxial Halo	39
3.1	Introduction	40
3.2	Initial Conditions	41
3.2.1	Dark Matter Halo	41
3.2.2	Satellite and Orbital Setup	42
3.3	Comparison of Orbital Decay	44
3.3.1	Dependance on Orbit Type in the Initial Conditions	46
3.4	Determination of Infall Time	47
3.4.1	Dynamical Time	48
3.4.2	Density at Pericentre	49
3.5	Phase Dependance	53
3.6	Conclusions	53
4	Dynamical Friction in Flattened Haloes	56
4.1	Introduction	57
4.1.1	Kinematically Decoupled Cores	57
4.1.2	Polar Ring Galaxies	59
4.2	Decay to the Equatorial Plane	60
4.2.1	Comparison with Axisymmetric Equatorial Decay	63
4.2.2	Changing the Satellite Mass	66
4.3	Polar Orbits	68
4.4	Conclusions and Discussion	72
5	Effects of Minor Mergers on Triaxial Haloes	74
5.1	Introduction	75
5.2	Infall Time Revisited	78
5.3	Halo Response of Satellite Accretion	79
5.4	Cusp Reduction	82
5.4.1	Mass Excavation	85
5.5	Halo Shape	87
5.5.1	Resultant Orbital Structure	90
5.6	Conclusions and Discussion	93
A	Deriving the Relaxation Time	95

असतो मा सद्गमया तमसो मा ज्योतिर्गमया ।
मृत्योर् मा अमृतं गमया ॥

-बृहदारण्यक उपनिषद् १ ३ २८

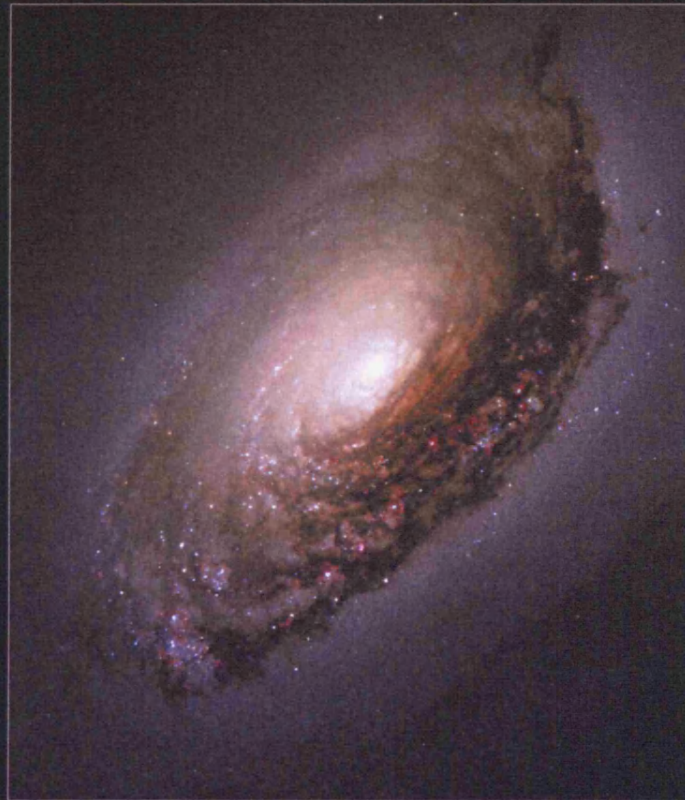
*From ignorance, lead me to truth;
From darkness, lead me to light;
From death, lead me to immortality*

-Brihadaranyaka Upanishad 1.3.28

1

Introduction

Spiral Galaxy M64



Hubble
Heritage

NASA and The Hubble Heritage Team (STScI/AURA) • Hubble Space Telescope WFPC2 • STScI-PRC04-04

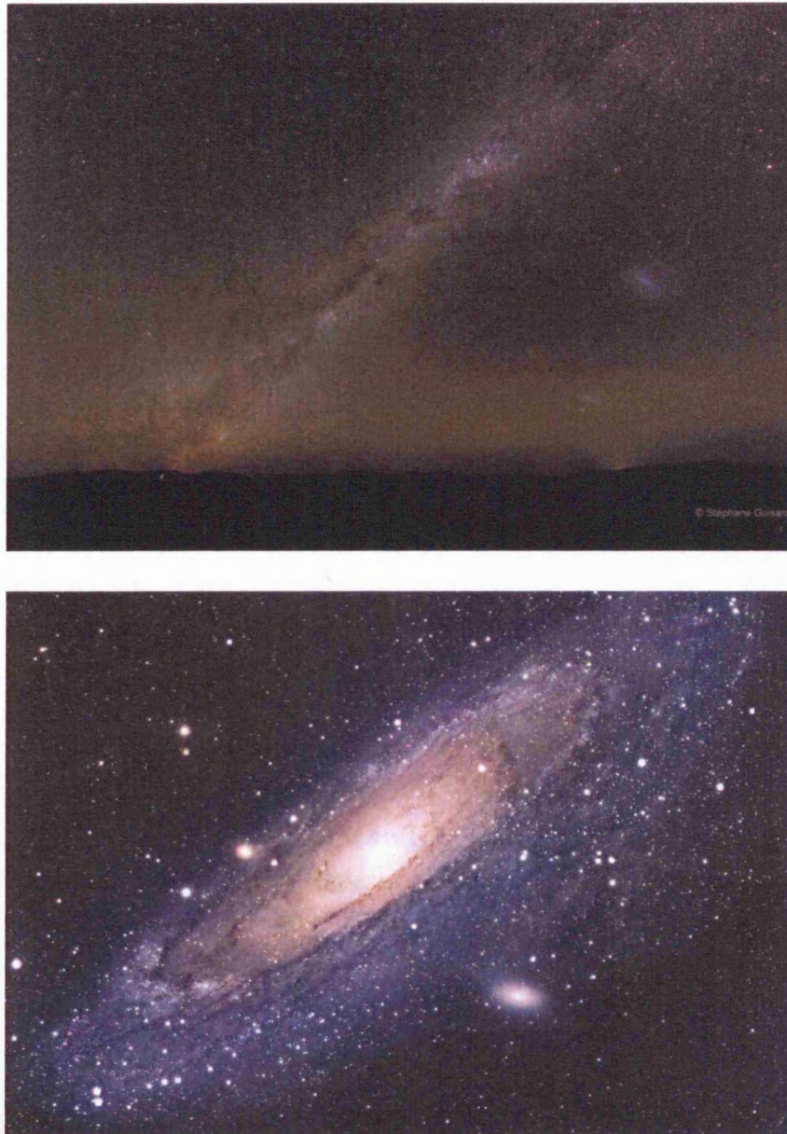


Figure 1.1: Image of the Milky Way and the Magellanic clouds (*top*). Image of the Andromeda galaxy taken by Robert Gendler (*bottom*).

1.1 Galaxies

Galaxies are some of the most beautiful and complex objects in the universe (chapter title pages) and they are one of the fundamental building blocks of the universe. They provide powerful tools for investigating some of the most important and fundamental problems in physics.

In the night sky, there is a continuous prominent white band that is visible to the

naked eye (Figure 1.1). The Ancient Hindu Vedic texts, which are the oldest sacred texts in Hinduism, refer to this band as being a pathway to heaven. It is the path that the Gods take to move to and from Heaven and Earth. It was made from a milky drink called Soma that made the Gods immortal. This notion that it was made from milk and was there because of the Gods was also shared by the Ancient Greeks who referred to this band as Γαλαξίας κύκλος or *Galaxias Kyklos* which translates to the Milky Circle. It is from this Greek name that we derive the word galaxy. The Ancient Romans, called this band *Via Lactea*, which literally translates to the Milky Way and is where we get the name for our own galaxy. It wasn't until 1610, when Galilei turned his telescope toward the band, that it was realised that it was composed of a huge number of faint stars. Wright (1750) correctly hypothesised that the Galaxy was a rotating body of a huge number of stars held together by gravitational forces, similar to the solar system but on a much larger scale, and that the resulting disk of stars can be seen as a band on the sky from our perspective inside the disk.

The nearest massive external galaxies to us, the Andromeda galaxy (M31, Figure 1.1 *bottom*) and the Magellanic clouds (Figure 1.1 *top*) can be seen with the naked eye. The first record of observations of the Andromeda galaxy and the Magellanic clouds was by Al Sufi (964), who described Andromeda as a “little cloud”. As the Magellanic clouds are only visible in the southern hemisphere, European astronomers were not aware of them until Ferdinand Magellan's attempt to circumnavigate the globe between 1519 and 1522, where they were observed by some of the crew. These galaxies were all thought just to be nebulae and it was Wright (1750) who hypothesised that some of the nebulae visible in the night sky might be separate Milky Ways. This was followed up by Kant (1755), who suggested that Andromeda, the Magellanic clouds and other nebulae that had been discovered might be “island universes”, like the Milky Way but viewed from a greater distance. This view was not widely accepted, as the observational evidence that these were indeed extragalactic sources was unclear, until the 1920s. Opik (1922) gave a distance determination that supported the theory that the Great Andromeda Nebula (as it was then known) was a distant extragalactic object. Hubble (1929b) was able to partially resolve the outer parts of Andromeda as “swarms of faint stars”. He identified and observed 50 Cepheid variable stars in these outer parts of Andromeda and was able to conclusively show that Andromeda was external to the Milky Way.

Today with modern day telescopes, we are able to probe the universe to much larger distances. The Hubble Ultra Deep Field which was an image taken by the Hubble Space Telescope from data accumulated over a period from September 24, 2003 through January 16, 2004, in an area with low density of stars. The depth of the image corresponds to looking at the universe to a depth of approximately 13 billion years (Redshifts between 7 and 12) (Figure 1.2). It took an image of an area of roughly one thirteen millionth of the



Figure 1.2: Image of the Hubble Ultra Deep Field showing the deepest view of the universe. In the picture, every bright point is a distant galaxy. Image credit to NASA, ESA, S. Beckwith and B.Mobasher (STScI).

total area of the sky, and contained around 10,000 galaxies. This shows that there could be $\sim 10^{11}$ galaxies in the visible cosmos.

Modern observations show that the Milky Way has around 10^{11} stars, with a total combined mass $\simeq 5 \times 10^{10} \mathcal{M}_{\odot}$; where $1 \mathcal{M}_{\odot} = 1.99 \times 10^{30}$ kg is the mass of the Sun (referred to as Solar mass unit). Most of the visible mass is contained in a thin disk with a radius of about 10 kiloparsecs and thickness of 0.5 kiloparsecs. The Sun is located at about 8 kiloparsecs away from the centre of the Galaxy. The Milky Way is estimated to have a total mass of $2 \times 10^{12} \mathcal{M}_{\odot}$, inferred from distant globular clusters and nearby satellite galaxies (Wilkinson & Evans, 1999), as it is embedded in a dark matter halo. Dark matter can only be observed through its gravitational effect on luminous matter.

1.2 Dark Matter in the Universe

Zwicky (1933, 1937) measured the mass-to-light ratio (Υ) of the Coma cluster of galaxies using the virial theorem (Clausius, 1870). He calculated $\Upsilon \sim 500 \mathcal{M}_{\odot} / \mathcal{L}_{\odot}$ (where \mathcal{L}_{\odot} is the Solar luminosity), which was extremely large compared to the local Galactic $\Upsilon \sim 3 \mathcal{M}_{\odot} / \mathcal{L}_{\odot}$ of the ordinary stellar population. The galaxies in the Coma cluster seemed to be moving in relation to one another at rates that violated the law of gravity unless the cluster

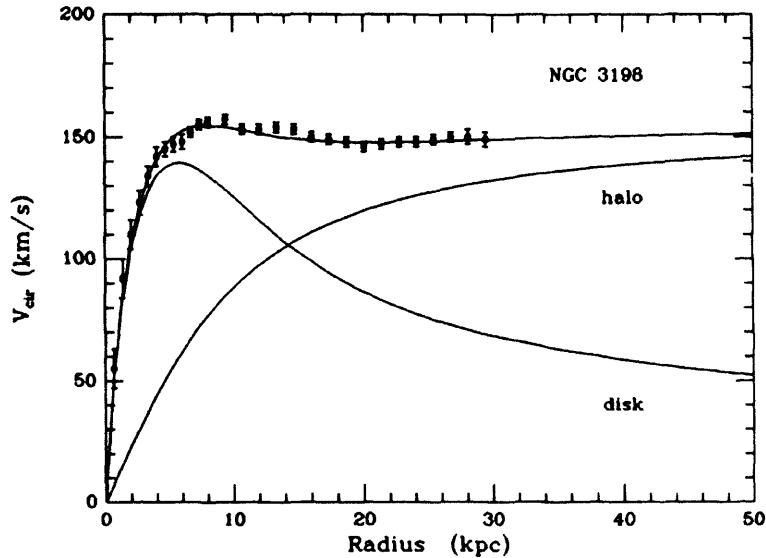


Figure 1.3: Figure from van Albada et al. (1985) showing the observed rotation curve of NGC 3198 (*dots with error bars*) and a fit of the disk and halo rotation curves.

contains a great deal of *Dunkle Materie* or dark matter.

After Zwicky's observations there were no other corroborating observations indicating that the mass-to-light ratio was anything other than around unity. The situation persisted until Volders (1959) demonstrated that the spiral galaxy M33 does not spin as expected according to Keplerian dynamics. Rubin et al. (1978) and Bosma (1978) looked at the rotation curves of galaxies to find that they did not have the expected Keplerian turnover but that the rotational velocity stayed roughly constant in the outer parts (Figure 1.3). This indicated that the radial mass profile of the galaxy, which is how the mass of the galaxy evolves with the radius, continues to increase beyond the observed visible edges of these galaxies.

Effects from dark matter haloes can be seen in observations of gravitational lensing. When the total mass of an object is very large, the gravitational field of the object is strong enough to “bend” light which creates multiple images or distorted arcs of an object along our line of sight. This effect is known as strong lensing. Strong lensing has been observed around a few distant galaxy clusters like Abell 1689. The mass of the cluster can be calculated by measuring the distortion geometry of the lensing system. The estimated masses from these strong lensing phenomena correspond with mass-to-light ratios obtained from measurements of velocities of galaxies within clusters.

X-ray observations of colliding clusters, for example the Bullet Cluster (Clowe et al., 2006), show that most of the hot gas and hence most of the baryonic matter is in the middle of the cluster. However, gravitational lensing maps of the background objects show that lensing is highest near the two visible components of the clusters. As the

lensing map infers the distribution of the dark matter, it shows that the clusters must be embedded in two separate dark matter haloes to produce the observed gravitational lensing map.

The precise nature of dark matter still remains a mystery. The particle that dark matter is comprised of does not interact with ordinary matter via electromagnetic forces, making it “dark”, and must have a mass as the observed interactions with ordinary matter are through the gravitational force. Candidates for dark matter particles are usually split into two broad categories, Baryonic and Non-Baryonic dark matter.

1.2.1 Baryonic Dark Matter

The favoured baryonic dark matter candidates are massive compact halo objects (MACHOs). Astrophysical objects like the relics of stars, dim stars such as white dwarfs, neutron stars, black holes, brown dwarfs are all contained in the haloes of galaxies. These objects are invisible, or extremely hard to detect so they are very good candidates for dark matter, and they are already known to exist.

MACHOs can be detected by looking at gravitational microlensing. If a MACHO in our galaxy’s halo passes across the line of sight between the Earth and a distant star, then the light from that star will be “bent” by the MACHO as it acts as a gravitational lens. Unlike strong lensing, the multiple images are separated by microarcseconds and so the distortion in shape is very difficult to observe, but the star will appear to brighten as it is lensed and this brightening can be detected.

Searches for microlensing due to MACHOs (Alcock et al., 2001) show a great deal of evidence that MACHOs cannot make up most of the dark matter halo. Additionally, the abundance of Deuterium in low-metallicity high redshift hydrogen clouds was measured to be in excellent agreement with the abundances predicted from Standard Big Bang Nucleosynthesis (Songaila et al., 1994). This suggests that most of the baryonic matter in the Universe is actually being observed and is thus not dark, Hence most of the matter contained in the universe must be non-baryonic matter.

1.2.2 Non-Baryonic Dark Matter Candidates

Non-Baryonic dark matter candidates can be split up into two distinct groups. The classification is based on the mass of the particle and the velocity of the particle after recombination. Recombination is the time in the history of the universe when the temperature of the universe had dropped sufficiently for electrons to be captured by hydrogen and helium ions. At the end of recombination, most of the atoms were neutral allowing the photons to travel freely. The photons emitted right after recombination are those that are seen in the cosmic microwave background (CMB) radiation.

Hot dark matter (HDM) particles move at ultra-relativistic velocities, (ie. most of the energy of the particle is due to the momentum component in $E^2 = m^2c^4 + p^2c^2$ or $pc \gg mc^2$), so the velocity is very close to the speed of light, c . The best candidate for HDM particles is the neutrino. Neutrinos have small masses ($\sim 2\text{eV}$ for an electron neutrino) and do not interact via electromagnetic forces. In a universe containing neutrino dark matter, just after the Big Bang, neutrinos are ultra-relativistic, so the density fluctuations are smoothed out as they stream through the universe. Structure formation then occurs in a “top-down model”. Due to the smoothing of the density fluctuations which reduces the density inhomogeneity, as the universe evolves the density fluctuations grow slowly. This leads to large scale structures forming first and the smaller structures, like galaxies and satellite galaxies forming from the fragmentation of these large scale structures.

This type of structure formation does not correspond to the large scale structure we see today in the universe around us, which tends to rule out the HDM scenario (White et al., 1983). Also, the observations of high redshift galaxies also rule out a HDM cosmology as the top-down structure formation requires large timescales for fragmentation down to galaxy scales.

Cold dark matter (CDM) particles move at nonrelativistic speeds. There are many different possible candidate CDM particles. The most likely candidate is a weakly interacting massive particle (WIMP), whose existence in nature is currently still hypothetical. WIMPs only interact via the weak force and gravity. The most commonly proposed WIMP dark matter candidate is the neutralino, which has a theoretical mass range of 30-5000GeV. A neutralino is the lightest particle from the supersymmetric extension to the standard model of particles. Other possible CDM candidates include: Axions, which are bosons with spin = 0; WIMPzillas, which are the heavier particles from the supersymmetric extension of the standard model and even more exotic candidates like Q-balls, Gravitinos and many more.

With CDM, structure formation occurs in the opposite order to the HDM case. The large scale structures are formed via hierarchical merging, where small objects merge to form larger objects, which in turn merge to form clusters. Comparisons of numerical simulations of CDM cosmology and observations are discussed in Section 1.3. The results from both match very well, which shows that the nature of dark matter is most likely cold. However a caveat to CDM is that none of the candidate particles have yet been found in nature.

1.2.3 Cosmological Evidence

Einstein (1917) found that his newly developed theory of relativity indicated that the universe must either be contracting or expanding and so he introduced a cosmological constant to allow the universe to remain stationary. This cosmological constant was aban-

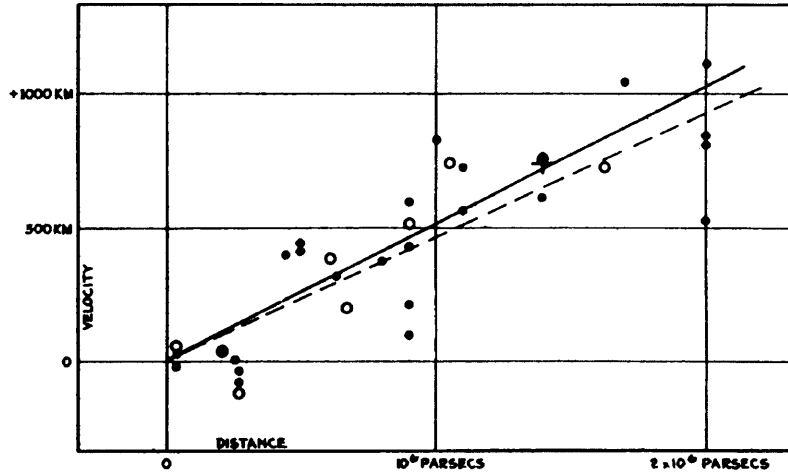


Figure 1.4: Figure from Hubble (1929a) showing the radial velocity and distance to 46 galaxies estimated from stars within the galaxy and mean luminosities. The filled circles and full line represent the solution for solar motion using the galaxies individually and the open circles and dashed line represent the solution combining the galaxies into groups. The cross represents the mean velocity and distance to 22 galaxies that could not be individually determined. The velocity-distance relation became known as Hubble’s Law.

done after Hubble (1929a) discovered that the universe was still expanding (Figure 1.4). Einstein labelled this introduction of the cosmological constant as the “biggest blunder” of his life. More recently, observations of Type 1A supernovae suggested that the expansion of the universe is accelerating (Riess et al., 1998; Perlmutter et al., 1999). Supernovae of this type are believed to be good standard candles across cosmological distances and so their distances away from us along with their redshifts give an indication of the expansion history of the universe. This result required the cosmological constant to be put back into the field equation in the general theory of relativity, with the cosmological constant being positive to describe the negative pressure that is accelerating the expansion of the universe and this phenomenon became known as dark energy. This cosmological constant was added to the CDM model, and Lambda Cold Dark Matter (Λ CDM) became the generally accepted concordance model for Big Bang cosmology.

The Wilkinson Microwave Anisotropy Probe (WMAP) was launched in 2001, to measure the anisotropy of the CMB in order to infer the geometry, content and evolution of the universe. The CMB is remarkably close to isotropic, the largest fractional RMS anisotropies are $\lesssim 10^{-4}$. These anisotropies are believed to arise from the quantum fluctuations introduced by inflation in the early universe. The current best fit for the WMAP data (Dunkley et al., 2009) gives estimates of the cosmological parameters of the universe (Hinshaw et al., 2009). The estimated age of the universe $t_0 = 13.72 \pm 0.12$ Gyr and the Hubble Constant, which defines the rate at which the universe is expanding, $H_0 = 70.5 \pm 1.3 \text{ km s}^{-1} \text{ Mpc}^{-1}$. The baryonic matter density $\Omega_b = 0.0456 \pm 0.0015$, the cold

dark matter density $\Omega_c = 0.02267 \pm 0.0013$ and the dark energy density $\Omega_\Lambda = 0.726 \pm 0.015$, all values being given as the ratio with the critical density (ie. $\Omega_i = \rho_i/\rho_0$), which is the density required to keep the universe from either contracting or expanding and therefore having a flat spatial (Euclidean) geometry. The ratio of the energy density of curvature Ω_k is in the range $-0.0179 < \Omega_k < 0.0081$ showing that the universe is very close to being flat. This shows that in a Λ CDM universe 72.6% of the energy density is made up of dark energy, and that there is ≈ 5 times more non-baryonic dark matter than there are baryons. What we see in the universe around us only makes up $\sim 4\%$ of the universe itself, so the universe has much more in it than we can see.

1.3 Cosmological Simulations of Dark Matter

Cosmological simulations are a very important tool for testing whether the proposed dark matter models match the observations. These simulations of structure formation follow the evolution of dark matter through time as the universe expands. As shown from the mapping of the temperature fluctuations in the CMB the density distribution was inhomogeneous due to fluctuations in the early universe, so the dark matter distribution of cosmological simulations starts with a distribution of small deviation from homogeneity. The dark matter is allowed to evolve under gravity using an N -body code (Chapter 2) sometimes with prescriptions to follow the hydrodynamics of gas within the universe.

1.3.1 Structure Formation in the Universe

Simulations of structure formation using Λ CDM cosmology (Press & Schechter, 1974; Davis et al., 1985; White et al., 1987; Evrard et al., 2002; Springel et al., 2005) agree very well with observations on megaparsec (Mpc) scales and by producing the filamentary structure and voids that are seen in galaxy surveys like the 2-degree Field Galactic Redshift Survey (Colless et al., 2001) and Sloan Digital Sky Survey (York et al., 2000). Figure 1.5 shows the distribution of galaxies produced from the 2-degree Field Galactic Redshift Survey and from the ‘‘Millennium’’ cosmological simulation (Springel et al., 2005). However on galactic scales there are discrepancies between the predictions of Λ CDM in simulations and the observational data. The two main discrepancies are the missing satellite problem and the cusp/core problem.

The cusp/core problem refers the difference between the simulated and observationally inferred distribution of dark matter in the centre of haloes. High resolution cosmological N -body simulations consistently predict that the density profile of dark matter is divergent at the centre and forms a cuspy peak, where the density profile is of the form $\rho(r) \propto r^{-\alpha}$ with $\alpha \gtrsim 1$ (Navarro et al., 1997; Moore et al., 1998; Fukushige & Makino, 1997; Power et al., 2003). However observations of rotation curves of dwarf spiral and LSB galaxies

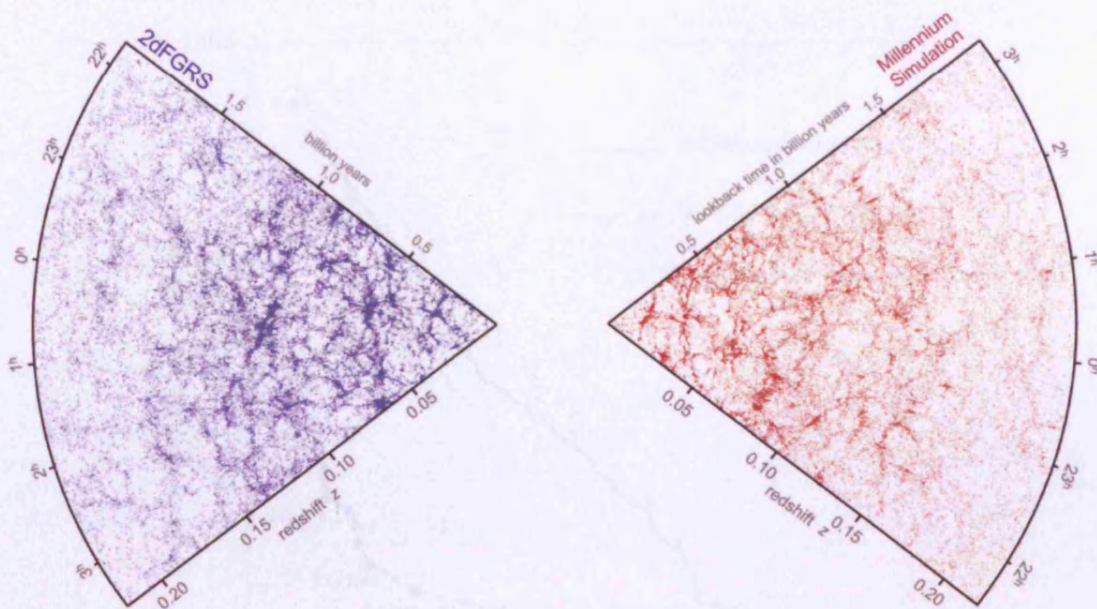


Figure 1.5: Figure showing the structure of the universe as from the 2-degree Field Galactic Redshift Survey and simulated from the Millenium simulation.

seem to show that the shape of the density profile at small scales is significantly shallower (Flores & Primack, 1994; Moore, 1994; Moore et al., 1999; de Blok & Bosma, 2002; de Blok et al., 2003). The cusp/core problem along with possible solutions will be discussed in more detail in Chapter 5.

The Λ CDM cosmological simulations have shown that structure formation in the universe is a bottom-up hierarchical process. The overdensities in the dark matter distribution gravitationally influences the surrounding areas and the dark matter begins to collapse into small haloes around these overdense areas. These small dense haloes collapse at high redshift and successively merge to form larger haloes. Moore et al. (1999) used simulations to examine the substructure within galactic and cluster mass haloes that form in a hierarchical universe and compared them with observations. When the simulated cluster halo mass function was compared with observations of the Virgo Cluster of galaxies, the two matched extremely well. However when the observed mass function for the simulated galaxy halo was compared to observations of the Milky Way and its satellites, the simulations overpredicted the number of satellite dwarf spheroidals by a factor of 50 (Figure 1.6). This figure also shows that the simulated cluster and galaxy halo have a similar mass function, despite the fact that the cluster halo is nearly a thousand times more massive and forms 5 Gyr later in the simulation. Klypin et al. (1999) did a similar simulation and found that within a 1.5Mpc radius the simulations overpredict the number of satellites by a factor of ~ 7.5 .

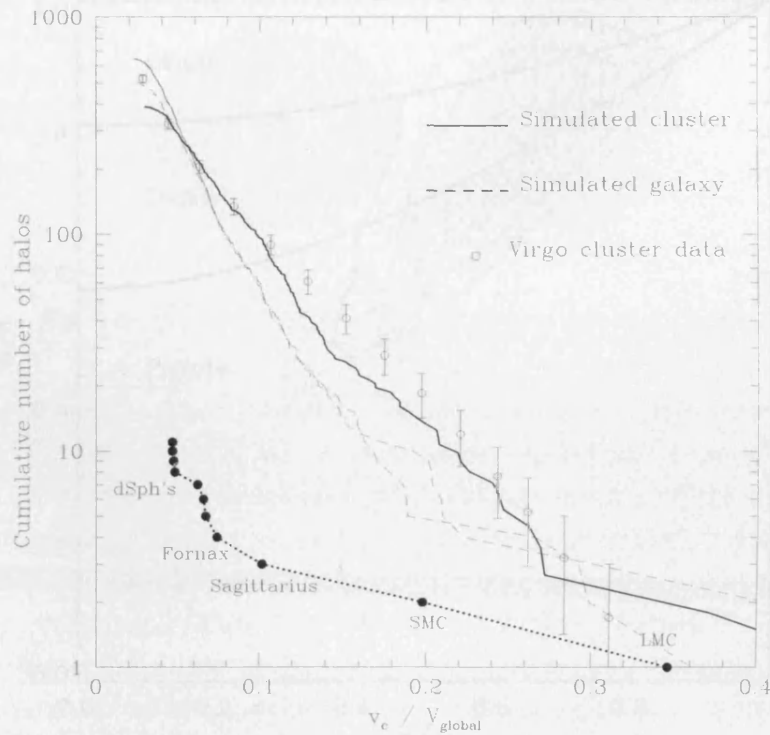


Figure 1.6: Figure taken from Moore et al. (1999), which plots the cumulative number of haloes as a function of their circular velocity, v_c which is normalised to the circular velocity of the parent haloes V_{global} which they inhabit. The dotted curve shows the distribution of satellites within the Milky Way's halo (Mateo, 1998), the open circles with Poisson errors are data for the Virgo Cluster of galaxies (Binggeli et al., 1985), the solid curve is simulated cluster halo and the two dashed lines show the simulated galactic mass halo at two different times, one at the current epoch and the other 4 billion years earlier.

There have been many proposed cosmological and astrophysical solutions to the missing satellites problem. Dekel & Silk (1986) were able to show that supernova feedback were able to suppress dwarf galaxy formation by blowing out the gas in low mass halos. Zentner & Bullock (2003) suppressed the number of satellite haloes by modifying the power spectrum at small scales. Colín et al. (2000) and Bode et al. (2001) had also been able to reduce the number of satellites by making the dark matter particles warm which also damps out the small scale density fluctuations. Bullock et al. (2000), Ricotti & Gnedin (2005) and Moore et al. (2006) showed that the formation of dwarf galaxies could be suppressed by reionisation of the universe preventing low-mass dark matter haloes from acquiring enough gas to form stars after $z \sim 10$. Mayer et al. (2001b,a) and Kravtsov et al. (2004) believed that the dwarf galaxies that are observed in their present appearance are the remnants of much larger objects that have been tidally stripped leaving the remnants we see today.

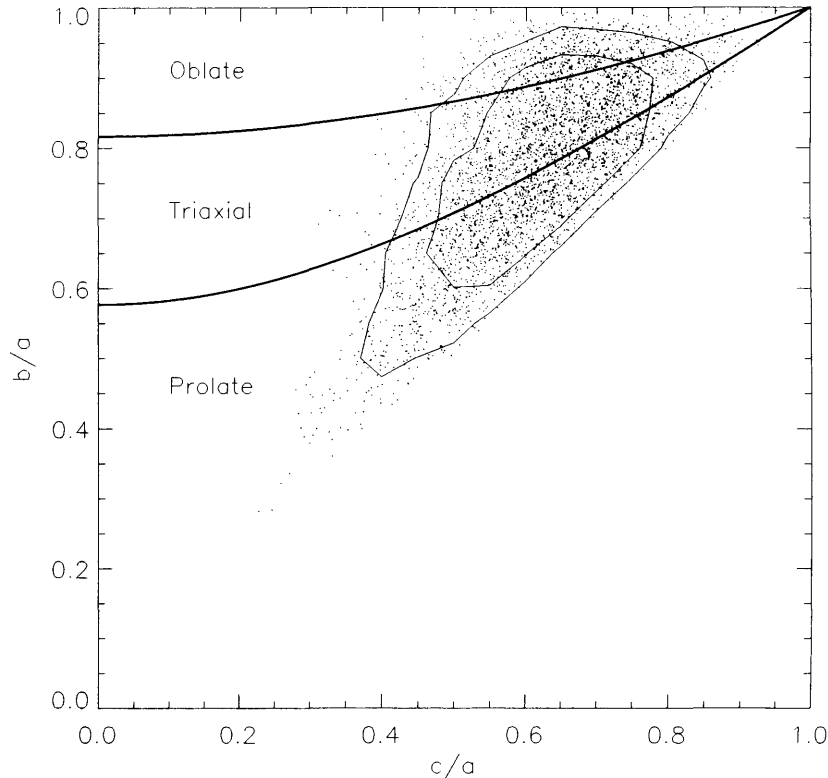


Figure 1.7: Plot taken from Bailin & Steinmetz (2005) showing the minor to major axis ratio c/a and the intermediate to major axis ratio b/a values at the radius $R = 0.4r_{\text{vir}}$ of all the haloes in their simulations, where r_{vir} is the virial radius of the halo. The inner and outer contours contain 68% and 90% of the haloes, respectively.

Recent observations from the SDSS have reduced the severity of the missing satellites problem as 21 new dwarf galaxies have been identified. Only a portion of the sky was observed in the SDSS. Hence the possible number of dwarfs likely to be discovered could increase by a factor of ~ 5 thus reducing the satellite deficit compared to the cosmological simulations by a factor ~ 4 (Simon & Geha, 2007). Tollerud et al. (2008) was able to reduce the deficit completely by correcting for the luminosity bias.

1.4 Shapes of Dark Matter Haloes

Cosmological N -body simulations have also shown that the dark matter haloes of galaxies and clusters are flattened triaxial systems (Frenk et al., 1988; Warren et al., 1992; Thomas et al., 1998; Jing & Suto, 2002; Springel et al., 2004; Bailin & Steinmetz, 2005; Allgood et al., 2006). Bailin & Steinmetz (2005) used a sample of 3869 simulated haloes with masses ranging from $1.4 \times 10^{11} \mathcal{M}_{\odot}$ to $4 \times 10^{14} \mathcal{M}_{\odot}$. They found that most of the haloes in

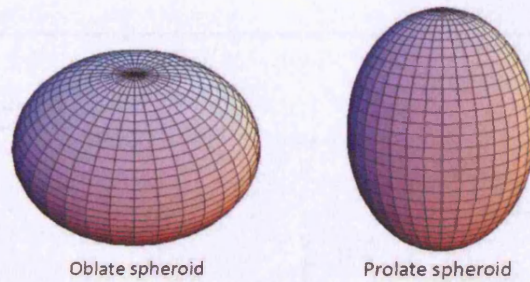


Figure 1.8: An example of an oblate and prolate ellipsoid

their study were mostly either triaxial or prolate in shape and with only a small fraction being oblate (Figure 1.7). The larger mass haloes tended to be more flattened at the virial radius. The virial radius is taken when average density of the halo is 200 times greater than the critical density of the Universe. The dynamical time at the virial radius is approximately the Hubble time. The minor to major axis ratio (c/a) had a near normal distribution peaking at 0.6, with a tail toward very flattened haloes.

Baryonic matter which dominates within the scalelength of the galactic disc will have an effect on the shape of the dark matter halo. Kazantzidis et al. (2004) and Debattista et al. (2008) showed that the condensation of baryons to the centres of haloes lead to rounder haloes.

1.4.1 Triaxial Haloes

The equation of an ellipsoid that is aligned with its principle axes along the Cartesian coordinate axes is

$$\frac{x^2}{a^2} + \frac{y^2}{b^2} + \frac{z^2}{c^2} = m \quad (1.1)$$

where a is the long (sometimes referred to as the major) principle axis, b the intermediate principle axis and c is the short (minor) principle axis and m is the triaxial radius. The principle axes are used to classify the shape of the ellipsoid. If $a = b = c$ then the ellipsoid is classed as a sphere. When two of the principle axes are equal then the ellipsoid is an axisymmetric spheroid. It is oblate when $a = b > c$ and prolate when $b = c < a$ (Figure 1.8). For the case when $a > b > c$, the ellipsoid is triaxial.

Triaxiality in a dark matter halo can arise in many ways. Examples include mergers of binary mergers of spherical haloes (White, 1978; Fulton & Barnes, 2001; Moore et al., 2004) and disk galaxies (Gerhard, 1981; Barnes & Hernquist, 1996; Naab & Burkert, 2003) and multiple mergers of haloes (Weil & Hernquist, 1996; Dubinski, 1998).

For a triaxial halo, the triaxiality can be quantified by the triaxiality parameter T :

$$T = \frac{a^2 - b^2}{a^2 - c^2} \quad (1.2)$$

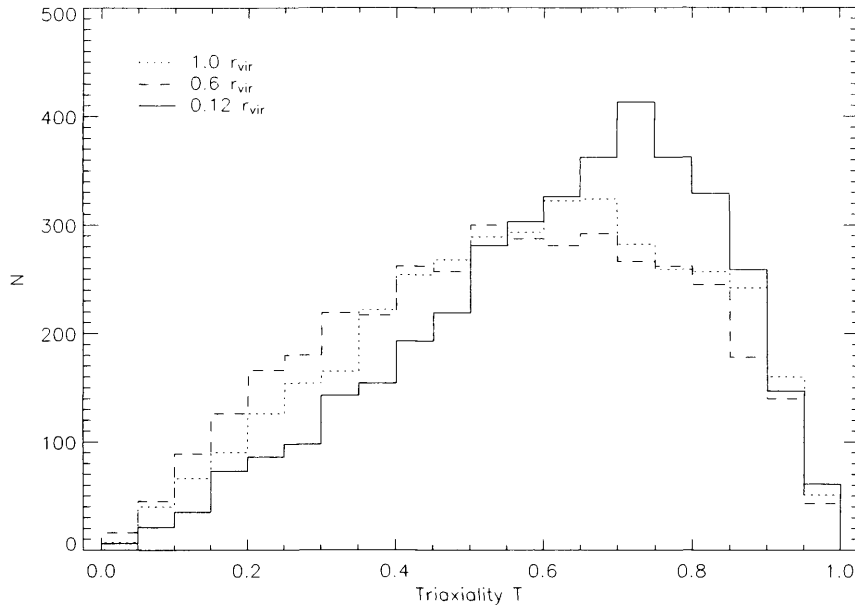


Figure 1.9: Plot taken from Bailin & Steinmetz (2005) of histograms of the triaxiality T of their sample of simulated haloes. The solid, dashed, and dotted histograms represent the haloes measures at $0.12r_{\text{vir}}$, $0.6r_{\text{vir}}$ and $1.0r_{\text{vir}}$, respectively.

(Franx et al., 1991). Purely prolate haloes have $T = 1$, while purely oblate haloes have $T = 0$. Cosmological simulations show that triaxiality arises via mergers with different amounts of angular momentum. Mergers with low angular momentum (radial mergers) produce prolate haloes, while high angular momentum mergers produce oblate systems. In cosmological simulations, haloes undergo a sequence of mergers with varying amounts of angular momentum so the haloes have arbitrary triaxiality that varies with radius (Moore et al., 2001). Figure 1.9 shows that the interior regions of haloes tend to be prolate (*solid histogram*). The c/a axis ratio decreases at large radii so many of the haloes become more oblate (*dashed histogram*) although there are more prolate haloes than oblate. At the virial radius, there is a small shift back to prolate haloes (*dotted histogram*).

1.4.2 Orbital Structure in Triaxial Potentials

The dynamical structure of a galaxy may be represented by a collection of orbits. The orbital content of triaxial potentials has long been of interest to dynamicists. In a triaxial potential, there is no obvious symmetry as each axis is different and the only isolating integral is energy. However, a special family of potentials exists called Stäckel Potentials (Stäckel, 1890). In these potentials, by changing the coordinate system to confocal ellipsoidal coordinates, the equations of motions become separable. de Zeeuw (1985) showed

that in integrable potentials there are four regular orbital families: box orbits, short axis tube orbits, inner long axis tube orbits and outer short axis tube orbits. These orbital families in the potential of a triaxial Stäckel potential are bound within a volume that is created from the focal hyperbola and the focal ellipses of the coordinate system (Figure 1.10). The box orbits are able to pass arbitrarily close to the centre of the potential (centrophilic) while loop orbits never pass through the centre (centrophobic).

In non-integrable triaxial potentials the situation is slightly more complex. In addition to the regular orbits from the integrable potential, periodic orbits and irregular orbits appear (Goodman & Schwarzschild, 1981; de Zeeuw & Merritt, 1983; Valluri & Merritt, 1998). Periodic (resonant) orbits occur when all the orbital frequencies are rational multiples of one frequency. In a triaxial potential, the resonant box orbits are known as boxlets. However unlike the regular box orbits, the boxlets are centrophobic.

The orbital structure of separable potentials becomes progressively richer with a decrease in the degree of symmetry of the models. In spherical models all orbits are in loops in planes through the centre (every spherical potential is a Stäckel potential). In axisymmetric models the loops become three dimensional tube orbits around the symmetry axis. The triaxial models contain tube orbits around the short and long axis, but also contain box orbits. It is the centrophilic box orbits that really make the triaxial dynamical structure unique.

1.5 Mergers of Galaxies

Cosmological simulations have shown that there is an abundance of low mass satellite haloes and that galactic haloes have strong substructure. These small haloes are accreted by the large host halo because of orbital decay of the satellite, a process known as a minor merger. Due to the number of satellite haloes, the host halo will undergo multiple minor mergers. Minor mergers between a satellite and its host can play a key role in the formation and growth of discs (Bekki & Chiba, 2001; Abadi et al., 2003; Martin et al., 2004; Navarro et al., 2004; Helmi et al., 2006). If a disc is already present then a minor merger can heat and increase the thickness of the disc (Quinn et al., 1993; Mihos et al., 1995; Walker et al., 1996; Velazquez & White, 1999; Wyse et al., 2006). Minor mergers can transport gas to the centre of the halo feeding active galactic nuclei which can play a key role in galaxy formation by triggering bursts of star formation.

Minor mergers are observed to be happening with the Milky way halo and satellite galaxies. The Magellanic clouds are greatly distorted from the tidal interaction with the Milky Way. The tidal interactions will produce stellar streams, Wannier & Wrixon (1972) discovered the H_I tidal Magellanic stream. The Sagittarius dwarf galaxy (Ibata et al., 1994) is one of the closest satellite galaxies to the Milky Way. The stellar stream that has

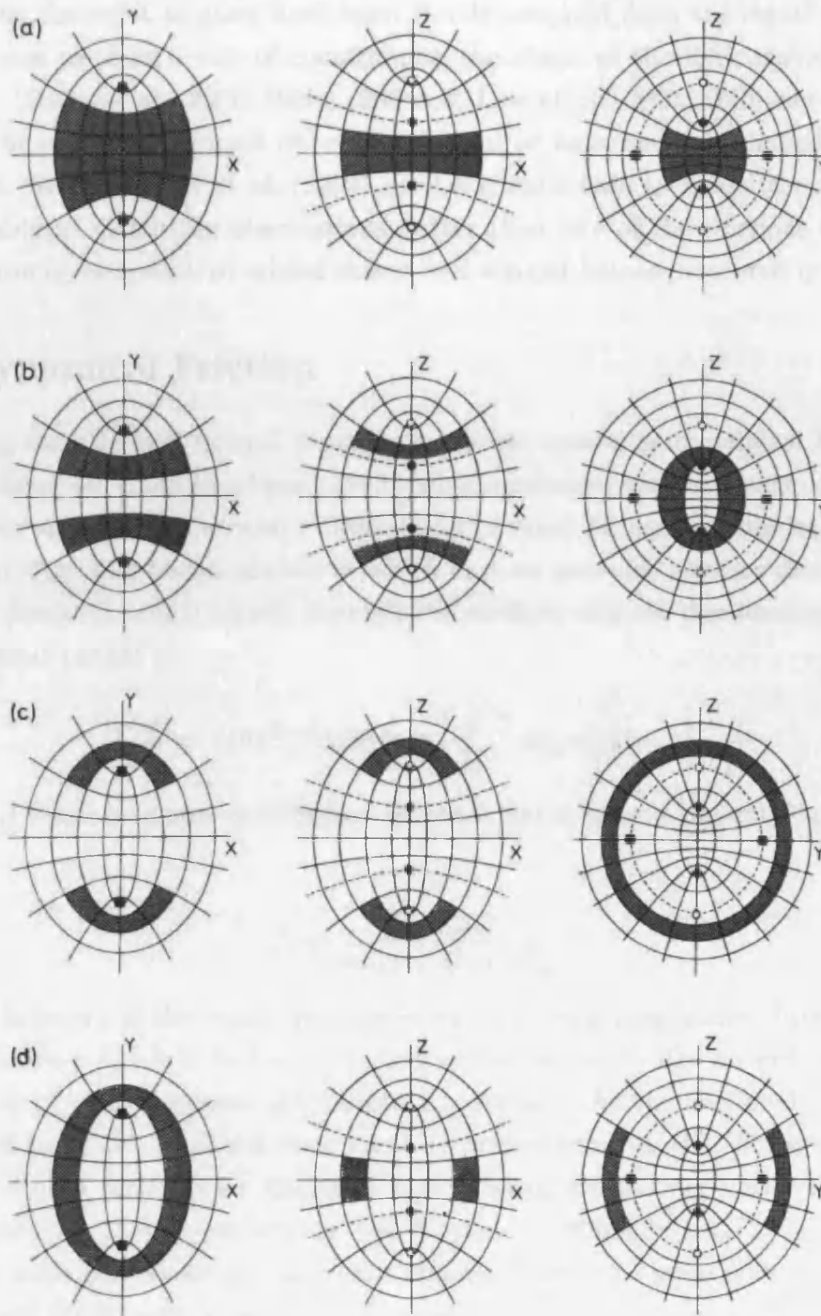


Figure 1.10: Plot from de Zeeuw (1985) showing the cross-sections with the three principle planes of a perfect ellipsoid. The shaded areas are the volumes allowed to the four general orbits by the values of the integrals of motion in an integrable triaxial potential. The three pairs of foci in the ellipsoidal coordinate system are denoted by the open and filled circles and the filled squares. The dashed curves indicated the focal hyperbola in the x-y plane and the focal ellipse in the y-z plane. (a) Box orbit; (b) inner long axis tube; (c) outer long axis tube; (d) short axis tube.

formed along the orbit as stars have been tidally stripped from the dwarf by the Milky Way, has been used as a way of constraining the shape of the dark matter halo of the Milky Way (Ibata et al., 2001; Helmi, 2004a,b; Law et al., 2005; Fellhauer et al., 2006). However, the studies only used either a spherical or axisymmetric shaped dark matter halo model. Recently, Law et al. (2009) used a triaxial halo to model the stellar stream and were able to match the observations better than any of the previous studies. This motivates the investigation of orbital decay in a triaxial haloes presented in this thesis.

1.6 Dynamical Friction

The driving force behind orbital decay is a process known as dynamical friction which was introduced by Chandrasekhar (1943) who considered the exchange of momentum via two-body encounters between a large body of mass M and an infinite, homogenous distribution of smaller bodies of mass m which have an isotropic velocity distribution. The large mass decelerates as it travels through the medium and the deceleration obtained by Chandrasekhar (1943) is

$$\frac{d\mathbf{v}_M}{dt} = -16\pi^2 G^2 M m \ln \Lambda \left[\int_0^{v_M} dv_m v_m^2 f(v_m) \right] \frac{\mathbf{v}_M}{v_M^3} \quad (1.3)$$

where $f(v_m)$ is the field star distribution function and Λ is the Coulomb logarithm and is defined by

$$\Lambda \equiv \frac{b_{\max}}{\max(r_h, GM/v_{\text{typ}}^2)} \quad (1.4)$$

where b_{\max} is known as the impact parameter which is the perpendicular distance of closest approach between the two bodies. Dynamical friction works like an ordinary frictional drag force as it always opposes the direction of motion. As the frictional acceleration is proportional to M the frictional force must be proportional to M^2 . The integral term in Equation 1.3 only accounts for the small bodies which are moving slower than the large body and so only they contribute to the friction. In Chandrasekhar's view, dynamical friction is a local process as only a limited volume around the large body is considered.

Marochnik (1968) and Kalnajs (1972) investigated the problem of dynamical friction from a different point of view. They looked at the density response of an infinite, homogeneous medium to a large moving body. They found that the particles form a wake behind the body. The attraction exerted on the body by the increase medium density of the wake results in a drag force that causes dynamical friction.

Tremaine & Weinberg (1984) and Weinberg (1986, 1989) investigated satellites moving within spherical systems using linear perturbation analysis. In the Chandrasekhar regime the dominant contribution to the drag comes from the distant encounters, perturbation

theory can be used to derive the drag force on the large body. They found that the satellite induces a global change in the distribution of matter in the galaxy. The frictional drag force on the satellite is almost all from the particles that are in resonance with the satellite's orbit.

1.7 Orbital Decay in Triaxial Haloes

The scientific problems that will be investigated within this thesis concerns the orbital decay of satellite galaxies. Satellite galaxies orbiting within the dark matter halo of a host galaxy will experience dynamical friction and so the orbit will decay until the satellite reaches the centre of the host galaxy where it merges with the host. Simulations of isolated equilibrium models are a very useful way of studying the dynamical evolution of gravitational systems in a controlled environment. This also allows the halo to be modelled with a higher resolution than the typical resolution of a single halo in a cosmological simulation. Most N -body simulations of isolated galaxies assume initially spherical dark matter haloes. This is due to the fact that creating N -body realisations of triaxial equilibrium models is difficult as they have no analytical distribution functions. For scenarios where the area of interest is within the scalelength of the galactic disc, the assumption of a spherical dark matter halo may be valid. However, in simulations that are concerned with the outer parts of the halo, like minor mergers, using triaxial shaped dark matter haloes may alter the results of the simulations and this will be investigated within this thesis.

The derivation of the Chandrasekhar dynamical friction formula assumes very idealised conditions which, in the real world, break down. Therefore, the orbital decay of satellite galaxies will be investigated using initial conditions that match what has been seen in cosmological simulations, e.g., the shape of the dark matter halo. In minor mergers within a triaxial dark matter halo, the initial condition of the trajectory of the satellite becomes much more important, as different trajectories will have different dynamical frictional forces due to the differing density background that the satellite travels through. The rich dynamical structure within a triaxial potential also affects the dynamical friction as the satellites may not be on simple loop orbits but on centrophilic box orbits. These properties of the initial conditions of the satellite placement will be investigated in Chapter 3.

Certain observational phenomena like polar ring galaxies and gas discs in elliptical galaxies can be explained via the process of minor mergers. As the nature of the mergers could be different in a triaxial potential, the consequences on the process of creating these phenomena will be investigated in Chapter 4.

Finally, in Chapter 5, the effect of the minor mergers on the host halo will be looked at. Again, we will focus on the impact of having halo triaxiality in a minor merger, and compare with previous studies which used a spherical shaped dark matter halo. The orbital

decay seen in a full N -body simulation will also be compared with the approximation that is given from the Chandrasekhar (1943) dynamical friction formula.

2.1 Collisionless Systems

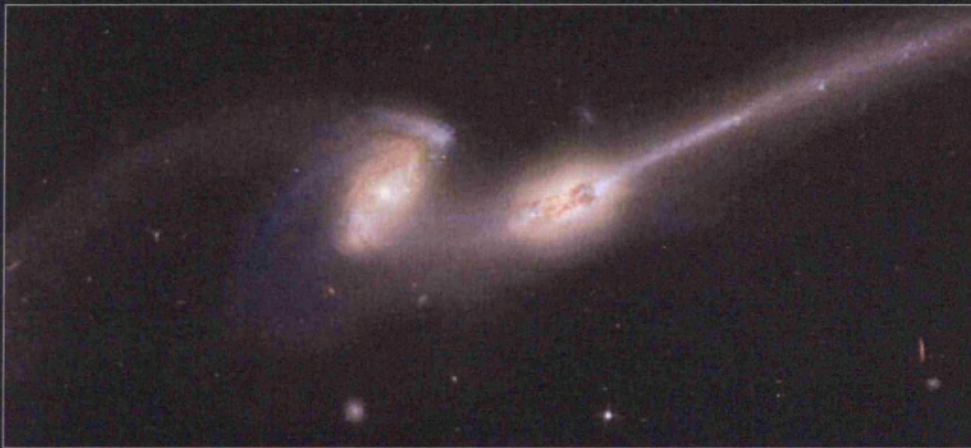
Apart from binaries or higher multiple stars and globular clusters, the distances between stars are enormous compared to the size of the stars themselves. Our nearest neighbour to the Sun, Proxima Centauri is ~ 4.3 pc away, which is 3×10^5 higher than the radius of the Sun. If we consider a system of radius R made up of N number of stars, with the stars having a radius r , we can look at the mean free path λ so that we can estimate when collisions will occur. The mean free path of a star is $\lambda = \frac{1}{n\sigma}$, where n is the number of stars per unit volume, in this case $n = \frac{N}{\frac{4}{3}\pi R^3}$, and σ is the individual cross section area of a star $\sigma = \pi r^2$. Putting this all together gives us a mean free path of

$$\lambda = \frac{3}{4} \frac{R^3}{Nr^2}$$

If we were to take some typical values for a galaxy, with $R = 10$ kpc and $N = 10^{11}$ and using $r = 5000$, which is a typical radius of a red giant star, we have a mean free path of $\lambda = 2.6 \times 10^6$ pc, which shows that direct collisions are extremely rare.

2

Methods



The Mice • Interacting Galaxies NGC 4676
Hubble Space Telescope • Advanced Camera for Surveys

NASA, H. Ford (JHU), G. Illingworth (UCSC/LO), M. Clampin (STScI), G. Hartig (STScI) and the ACS Science Team • STScI-PRC02-11d

2.1 Collisionless Systems

Apart from binaries or higher multiple stars and globular clusters, the distances between stars are enormous compared to the size of the stars themselves. Our nearest neighbour to the Sun, Proxima Centuari is $\sim 1.3\text{pc}$ away, which is 5×10^7 bigger than the radius of the Sun. If we consider a system of radius R made up of N number of stars, with the stars themselves having a radius r , we can look at the mean free path (λ) so gauge an idea of when collisions will occur. The mean free path of a star is $\lambda = \frac{1}{\rho\sigma}$, where ρ is the density of the system, in this case $\rho = \frac{3N}{4\pi R^3}$, and σ is the collisional cross section area, here it is $\sigma = 4\pi r^2$. Putting this all together gives us a mean free path of:

$$\lambda = \frac{R^3}{3Nr^2} \quad (2.1)$$

If we were to introduce some typical values for a galaxy, with $R = 10\text{kpc}$ and $N = 10^{11}$ and using $r = 500R_\odot$ which is a typical radius of a red giant star, we have a mean free path of $\lambda = 2.5 \times 10^7\text{kpc}$, which shows that direct collisions are extremely rare.

As gravity is a long range force, for a system like this where direct interactions are weak, it is reasonable to make the approximation that the force on a star is dominated by the bulk distribution of the galaxy, and not if the star lies close to another star. This means that the force acting upon the star will not vary rapidly and so we can say that gravitational force acting upon the star is from a smoothed density distribution rather than a collection of point masses.

2.1.1 Relaxation Time

It is important to explore the consequences of approximating a galaxy of N stars by a smooth density distribution and gravitational potential. A quantitative estimate comes from the relaxation time, which is the time taken for the sum of the velocity kicks from the encounters with the field stars (δv) becomes comparable to the initial velocity. If a star with initial velocity \mathbf{v} crosses the galaxy then the velocity is changed by Δv at each crossing. The number of crossings n_{relax} , needed for Δv to be of the order of the initial velocity \mathbf{v} is derived in Section A, which shows that it is

$$\frac{v^2}{\Delta v^2} = n_{\text{relax}} \simeq \frac{0.1N}{\ln N}, \quad (2.2)$$

so the relaxation time is simply defined by $t_{\text{relax}} = n_{\text{relax}} \times t_{\text{cross}}$, where $t_{\text{cross}} = R/v$ is the crossing time, the time taken for a star to cross the galaxy once, where R is the radius of the galaxy and v is a typical velocity, usually approximated by the circular velocity. The crossing time can be used interchangeably with other timescales like dynamical time, which is the time taken for a particle to fall from a radius R to the centre, and orbital

time as they are all very similar to each other.

For a galaxy which has $\sim 10^{11}$ stars, $t_{\text{relax}} \sim 2 \times 10^{16}$ yrs, which is greater than the age of universe ($\sim 14 \times 10^9$ yrs) and so it is definitely suitable to use the approximation of a smoothed density distribution as stellar encounters are unimportant.

2.1.2 The Collisionless Boltzmann Equation

The mass distribution of a collisionless system moving in a smooth potential $\Phi(\mathbf{x}, t)$ can be written as $f(\mathbf{x}, \mathbf{v}, t)$. $f(\mathbf{x}, \mathbf{v}, t)$ can alternatively be used to represent the number density. The mass of stars or dark matter in a small volume $d^3\mathbf{x}d^3\mathbf{v}$ around the position \mathbf{x} and velocity \mathbf{v} is $f(\mathbf{x}, \mathbf{v}, t)d^3\mathbf{x}d^3\mathbf{v}$. Since the system is collisionless, and it is approximated that mass is neither created or destroyed, we can say

$$\frac{df}{dt} = 0 \quad (2.3)$$

where this is a full convective derivative in phase-space such that

$$\frac{df}{dt} = \frac{\partial f}{\partial t} + \mathbf{v} \frac{\partial f}{\partial \mathbf{x}} - \frac{\partial \Phi}{\partial \mathbf{x}} \frac{\partial f}{\partial \mathbf{v}} = 0 \quad (2.4)$$

Equation 2.3 is known as the collisionless Boltzmann (or Vlasov) equation (CBE). The CBE along with the Poisson equation

$$\nabla^2 \Phi = 4\pi G \int f(\mathbf{x}, \mathbf{v}) d^3v, \quad (2.5)$$

can be used to describe the dynamics of a collisionless system. The Poisson equation is solved by a force solver.

2.2 N -body Simulations

In an N -body simulation the motion of N bodies is followed under their mutual gravitational attraction as well as under the influence of any external potential. It is a Monte-Carlo approach to solving the differential equations that describe the dynamics of any gravitating system. N -body simulations have become one of the most powerful tools for understanding many astrophysical problems, as with faster and more powerful computers, as well as efficient numerical algorithms, very complex systems can be modelled.

The first N -body simulations were performed by Holmberg (1941), using 37 light bulbs to represent two galaxies, and using the intensity of the light at each point to represent the gravitational force. This approach works as both the light intensity and gravitational force decrease as r^{-2} with distance r from the source. The first computational N -body simulations were performed by von Hoerner (1960), and were of a star cluster with $N =$

8 – 16. The rapid development of computer technology allowed for simulations of larger N , with $N = 100$ computational simulations being run by Aarseth (1963). The largest N -body simulation that has been undertaken so far is the “Millennium Simulation” Springel et al. (2005) which used $2160^3 = 1.01 \times 10^{10}$ bodies. Large scale galactic systems, like the Milky Way, contain $\sim 10^{11}$ stars, which is an order of magnitude greater than the largest N -body simulation performed. Therefore, each body cannot be thought of as an individual star, but rather as sampling the distribution function. The initial conditions of an N -body simulation are a representation of the mass distribution function $f(\mathbf{x}, \mathbf{v})$ (Section 2.1.2), which in the first approximation are a set of delta functions.

$$f(\mathbf{x}, \mathbf{v}) \rightarrow \sum_{i=1}^N \delta^3(\mathbf{x} - \mathbf{x}_i) \delta^3(\mathbf{v} - \mathbf{v}_i). \quad (2.6)$$

The approximation improves as N increases. This is why some accuracy in the force computation, by taking approximations in solving the force, is traded for increased N in N -body simulations.

2.2.1 Force Calculation

The most compute-intensive part of the N -body simulation is the determination of the gravitational force on each particle due to all others at every time step. There are a variety of methods that can calculate the force. Some methods sacrifice some accuracy for speed but the ideal method is always dependent on the type of problem.

The simplest and most accurate approach is to compute the forces directly for all the bodies (Aarseth, 1963). In this direct summation method the acceleration of each point particle is given by

$$\ddot{\mathbf{x}}_i = -G \sum_{j \neq i}^N \frac{m_j (\mathbf{x}_i - \mathbf{x}_j)}{|\mathbf{x}_i - \mathbf{x}_j|^3}. \quad (2.7)$$

The direct summation does not introduce approximations in the solutions of the equations of motion so deliver the highest accuracy but at the cost of longest computation time, as it requires $N - 1$ calculations for each of the N bodies which is of $\mathcal{O}(N^2)$. Special purpose hardware exists, the GRAvity PipE (GRAPE, Makino (1991)) which has been optimised to compute the gravitational interactions with greater performance than an ordinary CPU. This approach is normally used in cases with $N \lesssim 10000$ and where the forces at close range are particularly important e.g. in collision dominated systems, such as star clusters.

2.3 Force Softening

When the number of particles in the system being modelled is much larger than the number of bodies, N , in the simulation, the N -bodies are a Monte-Carlo representation of the distribution function. If the system being modelled is collisionless but is being simulated using a collisional N -body code, this can produce binaries and close encounters which require a large amount of computational time and care to accurately compute the forces, but are non-physical artifacts in a N -body simulation of a collisionless system. Therefore, softening of the force between bodies with small separations is needed to suppress these artificial two-body encounters and maintain that the simulation is as close to collisionless as possible.

The cost of softening is a loss in the spatial resolution and a bias in the force calculations. With softening, Equation 2.7 is replaced by

$$\ddot{\mathbf{x}}_i = -G \sum_{j \neq i}^N \frac{m_j}{\epsilon^2} \phi' \left[\frac{|\mathbf{x}_i - \mathbf{x}_j|}{\epsilon} \right] \frac{\mathbf{x}_i - \mathbf{x}_j}{|\mathbf{x}_i - \mathbf{x}_j|}. \quad (2.8)$$

where $\phi'(r)$ is the softening kernel, which is a function that tends to r^2 when $r > \epsilon$ and ϵ is the softening length. For the standard Plummer kernel $\phi = (1 + r)^{-1/2}$ which corresponds to a kernel density, the mass distribution by which each body is replaced with, $\eta(r) \propto (1 + r/\epsilon)^{-5/2}$, this however introduces a bias at small separations where the force tends to zero rather than infinity for $|\mathbf{x}_i - \mathbf{x}_j| \ll \epsilon$ and at large separations as the potential only slowly converges to the Newtonian limit. Dehnen (2001) performed a thorough analysis of the optimum softening in a N -body code. Following the conclusions of Dehnen (2001), the kernel used for all simulations in this thesis will be the stronger power-law Plummer kernel density

$$\eta(r) \propto (1 + r/\epsilon)^{-7/2} \quad (2.9)$$

which reduces the bias at large separations.

2.3.1 Particle Based codes

With force softening, the calculated force is an approximation to the true force. Therefore, less computationally intensive methods for calculating the force can be used, thereby allowing the simulations to run faster and allowing the use of a much larger N .

Barnes & Hut (1986) proposed a tree-code algorithm which is able to calculate local interactions accurately and was free from geometric assumptions and restrictions. The major idea of the tree-code is that the potential of a distant group of particles can be approximated by a low-order multipole expansion. The code starts with a single cubic cell

which contains all of the N -bodies. A tree-structured hierarchical subdivision of space is generated by dividing the cell into 8 sub-cells, each of which is recursively divided in the again whenever one or more bodies occupy the same cell. For each cell the mass, centre of mass and low-order multipole moments are computed and then the force on a particle is found by a “tree walk”. Starting from the top cell in the tree, each cell is checked to see whether it is far away enough from a specific particle, according to a pre-defined criteria. If the cell is distant enough from the particle, then it is put on the “interaction list”, if not, each of the sub-cells of that cell is checked in the same way, and so on until a complete interaction list of cells and individual bodies is found. The force on the body is found by summing up all the contributions of every cell or particle on the list. The generation of the interaction list reduces the number of interactions that need to be computed, thereby speeding up the process of calculating the gravitational force. The computational cost of building the tree and determining the accelerations of the bodies is of $\mathcal{O}(N \log N)$. The tree build only takes a few percent of the CPU time, so it is viable to rebuild it at every time-step. The process is sped up further by exploiting the fact that nearby particles will have very similar interaction lists. There is a small error in the force calculation when using a tree code. The nature of the error violates Newton’s third law and so this leads to momentum not being conserved.

2.4 Grid Based Codes

A common alternative to the particle-based schemes is to have the gravitational field of a system approximated on a mesh. Commonly referred to as Particle-Mesh (PM) codes, the position and masses of the particles are used to assign a density to every point on the mesh. The usage of a mesh allows the Poisson equation to be solved using a Fast Fourier Transform (FFT) routine under the assumption of appropriate boundary conditions, which are often periodic. This gives the potential on the mesh, from which the force on each particle can be calculated by interpolation. The simplest grid structure of a PM code is a fixed Cartesian grid. In this case, the computational cost scales as $\mathcal{O}(N + N_g(\log N_g))$ where N_g is the number of grid points. Using a Cartesian grid makes it difficult to handle non-uniform particle distributions as computational effort can be wasted on regions without any particles. If the regions of high density are known in advance then alternate grid geometries can be used to reduce the problem, for example using a cylindrical polar grid in disc simulations (Pfenniger & Friedli, 1993) or a spherical grid in halo or collapse simulations (van Albada & van Gorkom, 1977).

A number of refinements have been developed to improve the PM method. In particular, an adaptive grid rather than a static grid may be used. This known as Adaptive Mesh Refinement (AMR). After the initial grid potentials have been calculated, sub-grids

are automatically generated for regions with high number density thus allowing greater resolution and hence accuracy in the calculation of the forces (Gelato et al., 1997). Instead of FFT, the Poisson Equation is solved using multigrid methods. AMR codes are used for hydrodynamics simulations and are also well suited to cosmological simulations. Another evolution of the PM code is the Particle-Particle/Particle Mesh (P³M) method (Hockney & Eastwood, 1981). In the P³M method the long range forces are calculated using the PM method and the short range forces are computed via the direct summation of particle-particle interactions. However, if there is strong clustering involving a large number of particles, the computation is slowed as the computations are $\mathcal{O}(N^2)$. Adaptive P³M codes can reduce the computational cost to $\mathcal{O}(N\log(N))$. The short range forces can also be evaluated by using a tree code leading to a hybrid Tree-PM code Springel (2005), which is also $\mathcal{O}(N\log(N))$.

2.5 Self-Consistent Field

Another alternative method of calculating forces is the Self-Consistent Field (SCF) method (Hernquist & Ostriker, 1992). In this method the density and potential are expanded as a series of bi-orthonormal basis functions, such that

$$A_{nlm} = \sum_i m_i \phi_{nlm}, \quad (2.10)$$

$$\rho(\mathbf{x}) = \sum_{nlm} A_{nlm} \rho_{nlm}(\mathbf{x}), \quad (2.11)$$

$$\Phi(\mathbf{x}) = \sum_{nlm} A_{nlm} \Phi_{nlm}(\mathbf{x}), \quad (2.12)$$

where n is the radial “quantum” number, and the l and m are corresponding quantities for the angular variables. The individual harmonics ρ_{nlm} and Φ_{nlm} satisfy Poisson’s equation

$$\nabla^2 \Phi_{nlm}(\mathbf{x}) = 4\pi \rho_{nlm}(\mathbf{x}). \quad (2.13)$$

The force on each particle is found from the analytical differential of the potential. The computational cost scales as $\mathcal{O}(Nn_{\max}l_{\max}^2)$ as the SCF method iteratively solves N one-body problems. In problems with a high degree of symmetry is it possible to have little loss in accuracy with a relatively small number of terms in the expansions (Equation 2.11 and 2.12)

2.6 falcON

All the simulations performed in this thesis use, the fast and momentum-conserving tree code falcON [force algorithm with complexity $\mathcal{O}(N)$, Dehnen; Dehnen 2000; 2002] as the gravity solver, which combines the tree-code and fast-multipole method (FMM, Greengard & Rokhlin 1987). In FMM, which is mostly used in molecular dynamics, the bodies are sorted into hierarchically nested grid cells and the multipole moments of each cell are pre-computed. Then the forces between the grid cells are calculated by a multipole expansion, usually in spherical harmonics. The cells are both sources and sinks and so the exploitation that sink cells that are near to each other will feel a similar force from a distance source cell reduces the computational cost to $\mathcal{O}(N)$. In falcON, the bodies are split into a hierarchical tree structure of cubic cells where the cells' masses, centres of mass \mathbf{Z} and quadrupole moments are computed. The force is calculated from mutual cell-cell interactions as the cells are both sources and sinks, so for a pair of cells, A and B, the bodies in cell A must receive forces from cell B and vice versa. If the cells are well separated, the gravitational interaction can take place otherwise the cells must be split. The determination of whether the cells are well separated is done by a multipole-acceptance criterion which is an extension to the criteria to split a cell in the tree-code. Nodes A and B are deemed to be well-separated if

$$|\mathbf{Z}_A - \mathbf{Z}_B| > (r_{\max A} + r_{\max B})/\theta, \quad (2.14)$$

where the opening angle θ controls the accuracy of the code and r_{\max} is the radius of a sphere about the centre of mass \mathbf{Z} , which encloses all the bodies in the cell.

2.6.1 Approximating Gravity

The gravitational potential for N bodies at positions \mathbf{x}_i is given by

$$\Phi(\mathbf{x}_i) = -G \sum_{j \neq i} m_j g(\mathbf{x}_i - \mathbf{x}_j) \quad (2.15)$$

where m_j is the weight of the j th body and $g(\mathbf{x})$ is the Greens function describing the potential of the particle. For a unsoftened point particle $g(\mathbf{x}_i, \mathbf{x}_j) = 1/|\mathbf{x}_i - \mathbf{x}_j|$. For a softened particle, softened with the kernel density from Equation 2.9 becomes

$$g(\mathbf{x}_i, \mathbf{x}_j) = \frac{(|\mathbf{x}_i - \mathbf{x}_j|^2 + \frac{3}{2}\epsilon^2)}{(|\mathbf{x}_i - \mathbf{x}_j|^2 + \epsilon^2)^{3/2}}. \quad (2.16)$$

For a body at position \mathbf{x} in cell A and a body at position \mathbf{y} in cell B, where the two cells have their centres of mass at \mathbf{Z}_A and \mathbf{Z}_B , the mutual interaction can be described by the Greens function which is Taylor expanded about the separation $\mathbf{R} \equiv \mathbf{Z}_A - \mathbf{Z}_B$:

$$g(\mathbf{x} - \mathbf{y}) = \sum_{n=0}^p \frac{1}{n!} (\mathbf{x} - \mathbf{y} - \mathbf{R})^{(n)} \odot \nabla^{(n)} g(\mathbf{R}) + \mathcal{R}_p(g), \quad (2.17)$$

with the notation conventions from Dehnen (2002) in which $\mathbf{x}^{(n)}$ indicates the n -fold outer product of the vector \mathbf{x} with itself, and \odot is a tensor inner product. p is the order of the expansion and \mathcal{R}_p is the Taylor series remainder. Putting Equation 2.17 into 2.15 gives the potential due to cell B on cell A

$$\Phi_{B \rightarrow A}(\mathbf{x}) = - \sum_{m=0}^p \frac{1}{m!} (\mathbf{x} - \mathbf{Z}_A)^{(m)} \odot \mathbf{C}_{B \rightarrow A}^{m,p} + \mathcal{R}_p \quad (2.18)$$

where the field tensors $\mathbf{C}_{B \rightarrow A}^{m,p}$ are given by

$$\mathbf{C}_{B \rightarrow A}^{m,p} = \sum_{n=0}^{p-m} \frac{(-1)^n}{n!} \nabla^{n+m} g(\mathbf{R}) \odot \mathbf{M}_B^n \quad (2.19)$$

and the multipole moments of the cell (B in this example) \mathbf{M}_B^n are given by

$$\mathbf{M}_B^n = \sum_{\mathbf{y}_i \in B} m_i (\mathbf{y}_i - \mathbf{Z}_B)^{(n)}. \quad (2.20)$$

In falcON, instead of using a spherical multipole expansion, a Cartesian expansion of third order ($p = 3$) is used because the higher order multipole moments only contribute to $\mathbf{C}^{0,p}$ and so only affect potential (Φ) and not the force ($\nabla\Phi$). Since the accelerations of the bodies are to be computed, the octopole moments \mathbf{M}_B^3 can be ignored. As the Taylor expansion is performed about the centre of mass of the cell the dipole moment \mathbf{M}_B^1 is zero. This approximation is taken to be acceptable when the two cells are well separated. Since the softened particles are spherically symmetric, the Greens function depends on radius only, so the terms $\nabla^{(n+m)} g(\mathbf{R})$ can be calculated with

$$D^m \equiv \left(\frac{1}{r} \frac{\partial}{\partial r} \right) g(r) \Big|_{r=|\mathbf{R}|} \quad (2.21)$$

and the coefficients of the Taylor series are

$$\begin{aligned} \mathbf{C}_{B \rightarrow A}^0 &= m_B [D^0 + \frac{1}{2} \tilde{\mathbf{M}}_{Bii}^2 D^1 + \frac{1}{2} R_i R_j \tilde{\mathbf{M}}_{Bij}^2 D^2], \\ \mathbf{C}_{B \rightarrow A, i}^1 &= m_B [R_i (D^1 + \frac{1}{2} \tilde{\mathbf{M}}_{Bjj}^2 D^2 + \frac{1}{2} R_j R_k \tilde{\mathbf{M}}_{Bjk}^2 D^3) + R_j \tilde{\mathbf{M}}_{Bij}^2 D^2], \\ \mathbf{C}_{B \rightarrow A, ij}^2 &= m_B [\delta_{ij} D^1 + R_i R_j D^2], \\ \mathbf{C}_{B \rightarrow A, ijk}^3 &= m_B [(\delta_{ij} R_k + \delta_{jk} R_i + \delta_{ki} R_j) D^2 + R_i R_j R_k D^3], \end{aligned} \quad (2.22)$$

where Einstein's sum convention has been used, R_i is the i th Cartesian coordinate of the

separation between the two centres of mass, $m_B = \mathbf{M}_B^0$ as the monopole term is the mass of cell B and $\tilde{\mathbf{M}}_{Bij}^2$ is the i, j th Cartesian component of the specific quadrupole moment tensor ($\tilde{\mathbf{M}}_B^2 \equiv \mathbf{M}_B^2 / \mathbf{M}_B^0$).

When all the necessary interaction coefficients have been determined, the coefficients in each cell are summed over all interactions. The force on an individual body is calculated by summing up the interactions coefficients of all the cells that the body is in, all the way to the root cell. Before this can happen the Taylor expansion of those cells need to be translated to a common centre.

Let $\mathbf{C}_A^{m,p}$ be the coefficients about the centre of mass (\mathbf{Z}_A) of cell A, the coefficients after a translation to a new centre \mathbf{Z}_C are

$$\mathbf{C}_C^{m,p} = \sum_{n=0}^{p-m} \frac{1}{n!} (\mathbf{Z}_A - \mathbf{Z}_C)^{(n)} \odot \mathbf{C}_A^{m+n,p} \quad (2.23)$$

2.7 gyrfalcON

Once all the accelerations of the bodies are known the positions and velocities are evolved for that time-step using an integrator which numerically solves the equations of motions. The program gyrfalcON (GalaxY simulators using falcON), written by Walter Dehnen, combines a leapfrog integrator with the falcON force calculator and is part of the NEMO stellar dynamics toolbox (Teuben, 1995). The particle positions and accelerations of the bodies are calculated at each time step and the velocities are calculated at each half time step to improve the accuracy of the integration. This method is known as the ‘‘Kick-Drift-Kick’’ scheme of the leapfrog and it is this scheme that is employed in gyrfalcON and is represented mathematically as a loop over the operations

$$\begin{aligned} \mathbf{v} &= \mathbf{v} + \mathbf{a} \frac{\Delta t}{2}, & (\text{Kick}) \\ \mathbf{x} &= \mathbf{x} + \mathbf{v} \Delta t & (\text{Drift}) \\ \mathbf{a} &= -\nabla \Phi & (\text{NewAccelerations}) \\ \mathbf{v} &= \mathbf{v} + \mathbf{a} \frac{\Delta t}{2} & (\text{Kick}). \end{aligned} \quad (2.24)$$

The leapfrog integration algorithm is accurate to the second order in Δt , and is also time symmetric, so the original positions and velocities are recovered if the integration is reversed. If the Hamiltonian of the system is separable then the integrator will conserve the phase space volume and so it is ‘‘symplectic’’. This will also ensure that the energy of the system is well conserved over a long time period.

The leapfrog algorithm is ideal for situations in which solving for the acceleration of every particle at every time-step is appropriate, but in a system, like a dark matter halo, where there is a large range of dynamical times for the bodies, this is not the case. For the

bodies in the centre smaller time steps are required than for bodies in the outer regions. With a single global time-step for all bodies, either the innermost bodies are not followed closely enough, resulting in large integration errors, or the outermost bodies are integrated unnecessarily accurately, thereby wasting CPU time. As a solution to this problem for system with large dynamic range, **gyrfalcON** uses an individual time-step scheme. The full time-step (block-step, $\tau_{\max} = 2^{-k_{\max}}$) is broken up on n levels, each level with time-steps of half the time-step in the level before, upto the smallest time-step τ_{\min} which is 2^n times smaller than τ_{\max} . All of the bodies drift with time-steps τ_{\min} but the force computation is carried out on the individual time-step of that body. The criterion for choosing the time-steps of the body are based on the acceleration \mathbf{a}_i and the potential Φ_i of that body. These are parameterised through the **fac** and **fph** parameters, and the time-step of the body τ_i is defined by

$$\tau_i = \min \left\{ \frac{\mathbf{fac}}{|\mathbf{a}_i|}, \frac{\mathbf{fph}}{|\Phi_i|} \right\} \quad (2.25)$$

During the simulation, each body can move down a level (smaller block step) at any block step, but can only move up a level at the synchronisation point between the levels (ie. when the next block step starts at the time in the simulation). Using individual time-steps the symplectic nature of the leapfrog is broken, yet the energy conservation in simulations undertaken in this thesis with individual time-steps are very good and more than acceptable indicating that it is valid to use the individual time-steps.

2.8 Made to Measure N -body method

Cosmological N -body Simulations using the current paradigm of Lambda Cold Dark Matter (Λ CDM) have shown that the dark matter (DM) haloes of galaxies and clusters are generally flattened, triaxial systems (Frenk et al., 1988; Dubinski & Carlberg, 1991; Warren et al., 1992; Thomas et al., 1998; Jing & Suto, 2002; Springel et al., 2004; Allgood et al., 2006; Bailin & Steinmetz, 2005). There are several techniques available for creating triaxial equilibria so that they can be studied in isolation. Holley-Bockelmann et al. (2001) used a technique of starting with a spherical Hernquist (1990) profile and then adiabatically applying a drag to the particle velocities along the principle axes in order to create cuspy triaxial systems. More recently, Moore et al. (2004) used a method which is based on the way the DM haloes are formed in hierarchical cosmological simulations, where prolate/oblate DM haloes are formed by mergers of low/high orbital angular momentum. These techniques, in particular the latter, have the disadvantage that one has little control over the shape and density profile of the triaxial equilibrium system generated.

Schwarzschild (1979) was able to create triaxial equilibria using his orbit-based method. A dynamical model was created by integrating many orbits over many orbital times in

an assumed gravitational potential and putting their properties into an orbit library. The orbit are superposed with positive definite weights to reproduce a triaxial mass distribution. Syer & Tremaine (1996) developed a method for constructing N -body realisations of equilibrium stellar systems. In this so called “made to measure” (M2M) technique equilibria are constructed by integrating an N -body system, while slowly adjusting the masses of the particles until the time-averaged density field (and other observables) converge to a prescribed profile. This M2M technique was further improved upon by de Lorenzi et al. (2007) to make the technique more suited to mixed observables like densities and kinematics where the target observables can be zero-valued. Dehnen (2009) further improved the M2M technique to rectify some of the problems in the M2M formulation. M2M is able to transform a spherical model into a triaxial equilibrium whilst having full control over both the density profile and shape. The M2M method is closely related to the Schwarzschild (1979) method, in that orbits are integrated and then superposed, but in M2M this is done at the same time: while the trajectories are being calculated the weights are being adjusted.

The goal of M2M is to create a particle model which matches some target observable in a system. The algorithm individually adapts the weights of the particles moving in an assumed global potential until the deviations between the particle model and the observables is minimised. The observables of the particle is given by

$$y_j = \sum_i w_i K_j(\mathbf{x}_i, \mathbf{v}_i) \quad (2.26)$$

where K is a known kernel and the particle weights $w_i \equiv m_i/M_{tot}$. The deviations of the particle observables are calculated using a χ^2 -like measure given by

$$C = \sum_{j=1}^n \left(\frac{Y_j - y_j}{\sigma_j} \right)^2 \quad (2.27)$$

where Y_j are the target observables and the uncertainties of the observables are σ_j . Since the number of particles will be much greater than the number of independent constraints, the observables of the particles can remain constant while the weights are still changing with time. So a merit function is introduced

$$Q = \mu S - \frac{1}{2}C. \quad (2.28)$$

The merit function is maximised to fit the N -body model to the observables. S is a penalty function and is multiplied by a Lagrange multiplier μ , which regularises the merit function. The penalty function is taken to be the pseudo-entropy

$$S = - \sum_i w_i \log \frac{w_i}{\hat{w}_i}, \quad (2.29)$$

with $w_i^* \equiv w_i / \sum_j w_j$ the normalised weights and the $\{\hat{w}_i\}$ are a predetermined set of weights, the so-called priors. As

$$\mu \frac{\partial S}{\partial w_i} = -\mu(\log(w_i/\hat{w}_i) + 1), \quad (2.30)$$

if a particle weight $w_i < \hat{w}_i/\epsilon$ (where ϵ is the rate of change) then Equation 2.30 becomes positive and is negative when $w_i > \hat{w}_i/\epsilon$. So the pseudo-entropy term forces the weights to remain close to their priors.

The weights of the particles are adjusted slowly so that Q is maximised. The weights are evolved as

$$\dot{w}_i = \epsilon w_i U_i \quad (2.31)$$

where U_i is the velocity of change,

$$U_i = \frac{\partial Q}{\partial w_i}, \quad (2.32)$$

(although it is incorrectly referred to as force of change in ST96 and DL07 - it is only a first order derivative). For the choice of the constraint function given in Equation 2.27, U_i is now

$$U_i = \mu \frac{\partial S}{\partial w_i} - \sum_{j=1}^n \frac{Y_j - y_j}{\sigma_j^2} K_j(\mathbf{x}_i, \mathbf{v}_i). \quad (2.33)$$

For small enough values of ϵ , integrating Equation 2.32 will eventually result in a maximal Q , with the w_i no longer changing. The method is similar to the Richardson (1972)-Lucy (1974) iteration.

To reduce any temporal fluctuations, the observables are smoothed over a timescale, which is obtained from the integration of the differential equation

$$\frac{d(\bar{y})}{dt} = \alpha(y_j - \bar{y}_j), \quad (2.34)$$

where α is a constant, with the initial value of $\bar{y}_j = y_j$ at $t = 0$. Directly replacing y_j with \bar{y}_j into Equation 2.33 means that the weight adaption is not actually along the gradient of the merit function.

2.8.1 Dehnen's Novel M2M Method

The velocity of change (Equation 2.32) will vary for each particle over the orbit as different parts of the orbit will contribute differently to the merit function. The rate of change should be $\epsilon < \Omega_i$, where Ω_i is the orbital frequency of the particle. However in a N -body system the orbits of the particles can vary by orders of magnitude, so using a low adaption rate, as used in traditional M2M means that the weights for the outermost particles are not adjusted adiabatically. Therefore, integrating each particle on its own dynamical time will achieve that $w_i \propto \epsilon$. This is done by introducing a dimensionless time

$$\tau = t/T_i \quad (2.35)$$

with $T_i = 2\pi/\Omega_i$ the orbital period and is estimated using the epicycle approximation. The equations of motion for the N -body system expressed in terms of τ are

$$\mathbf{x}_i'' = -T_i^2 \nabla \Phi(\mathbf{x}_i) \quad (2.36)$$

where a prime denotes the derivative with respect to τ . The M2M weights are now integrated as

$$w_i' = \epsilon w_i U_i \quad (2.37)$$

with ϵ a dimensionless rate of change per orbit for each particle.

Traditional M2M has no guarantee of the conservation of the weights $\sum_i w_i = 1$. It is assumed that the weights are renormalised after each step. Analogous to Dehnen (1998), the unconstrained maximum of the modified merit function

$$Q^*(\mathbf{w}) \equiv Q(\mathbf{w}^*) + \ln \sum_k w_k - \sum_k w_k \quad (2.38)$$

maximises $Q(\mathbf{w})$ subject to the constraint $1 = \sum_k w_k$. So the weight constraint can be enforced by replacing Q with Q^* in Equation 2.32.

As mentioned above, in the traditional M2M, the time-averaging of the observable leads to the mass adaption not being along the gradient of the merit function. It is advantageous to instead average Q^* , which also suppresses the fluctuations of the merit function. Analogous to Equation 2.34, this gives

$$U_i' = \eta \left(\frac{\partial Q^*}{\partial w_i} - U_i \right) \quad (2.39)$$

where η is a dimensionless averaging rate. Combining this with Equation 2.37 results in a true force of change for $\phi \equiv \ln w_i$

$$\phi_i'' = \epsilon \eta \frac{\partial Q^*}{\partial w_i} - \eta \phi_i' \quad (2.40)$$

So, $\frac{\partial Q^*}{\partial w_i}$ acts like a force for the ϕ_i and replacing it with the gradient of Q^* with respect to the dependant variable ϕ gives

$$\phi_i'' = \lambda \frac{\partial Q^*}{\partial \phi_i} - \eta \phi_i' \quad (2.41)$$

where $\lambda = \epsilon\eta$, this corresponds to

$$U_i' = \eta \left(w_i \frac{\partial Q^*}{\partial w_i} - U_i \right). \quad (2.42)$$

2.8.2 Creating Triaxial Initial Conditions

To create triaxial equilibrium models, observables which describe the system are needed. Using the method from SCF (Section 2.5), the expansion coefficients are used as the observables of the system as they describe the density. The expansion coefficients $A_{\mathbf{n}}$ for the potential expansion are

$$A_{\mathbf{n}} = \sum_i^N w_i \psi_{\mathbf{n}}(\mathbf{x}_i) \quad (2.43)$$

With N number of bodies with weights w_i and positions \mathbf{x}_i . The constraint function is of the form

$$C_\rho = \sum_n \left(\frac{A_{\mathbf{n}} - B_{\mathbf{n}}}{\sigma_{\mathbf{n}}} \right)^2. \quad (2.44)$$

For the interested reader, stability analysis and more details are provided in Dehnen (2009).

These tools meant that we could use Dehnen's 2009 made to measure method to generate multiple stable triaxial models and `gyrfalcON` to evolve satellites in these haloes. The resulting simulations are a significant step forward relative to previous works as it allows the detailed probing of minor mergers within triaxial haloes.

2.9 Analysis Methods

2.9.1 Orbital Analysis

As mentioned in Section 1.4.2, in a triaxial potential there are four different orbital families that an orbit can be classified into, these are short-axis tube, long-axis tube, box and chaotic. If a massless particle was allowed to evolve in a smooth triaxial potential, it would orbit on one of these orbital family types depending on the phase-space coordinate it was released from. Short-axis tubes orbit (Figure 2.1a) about the shortest principle axis in the potential. In this type of orbit the sign of the z -component of angular momentum is conserved. The possible orbital path will be contained in a volume of a roughly cylindrical tube around the short-axis. Long-axis tubes (Figure 2.1b) orbit about the long axis and

approximately conserve the x -component of the angular momentum. The long-axis tubes can be further split into two families, inner and outer long-axis tube orbits which are characterised by the annulus formed in the plane of the short and intermediate axes. In box orbits (Figure 2.1c) there are independent oscillations along the three different axes as it evolves through the system so there is no sense of circulation and the time averaged angular momentum is zero. The orbital path of the massless particle will eventually fill up a volume that is topologically a box, and unlike tube orbits, the orbit is able to get arbitrarily close to the centre of the system. Chaotic orbits (Figure 2.1d) are irregular and follow no particular patterns, they eventually pass through all of phase-space that is energetically available to them.

To ascertain what type of orbits the satellites were on, a massless particle was placed at the initial position of the satellite and the orbit of the satellite was integrated for many dynamical times in a static representation of the triaxial halo model. Simulations of this kind are called semi-analytic simulations as the force is computed from an analytical external potential rather than point particles. A leapfrog integrator (Section 2.7) was used to integrate the orbit with the system being integrated using fixed time steps. By looking at the conservation of the components of the angular momentum (\mathbf{L}), the orbits can be classified into the orbital families. The static potential was calculated from the N -body model akin to the self consistent field method (Section 2.5), and due to this method which attempts to create a smooth potential from expansion coefficients, there were irregularities in the potential from it being perfectly smooth. Due to this, some of the orbits transformed from one orbital family to another. This effect was mostly seen in the particles initially on box orbits as the irregularities were in the region $m < 0.1$, and as box orbits are able to get arbitrarily close to the centre, they were mostly likely to be affected as from the non-smooth potential so it switches to another orbit of the same energy. We refer this phenomena as weak chaos. Figure 2.1e shows a weak chaotic orbit. The caustics of the box orbit can clearly be seen. However the complete volume is also being filled and so it had turned into a chaotic orbit. The long and short axis tubes were classified automatically using the conservation of the respective angular momentum components. The box, chaotic and weakly chaotic orbits were classified by eye as the automatic algorithm could not distinct between these types. As the weak chaos orbits were only a factor in the orbital analysis of classifying the initial orbit and only occurred when integrating the orbit in the static potential there is no effect of this kind in the full N -body simulations for where the results of orbital decay are obtained in Chapter 3. Therefore it was reasonable to proceed without needing a smoother potential.

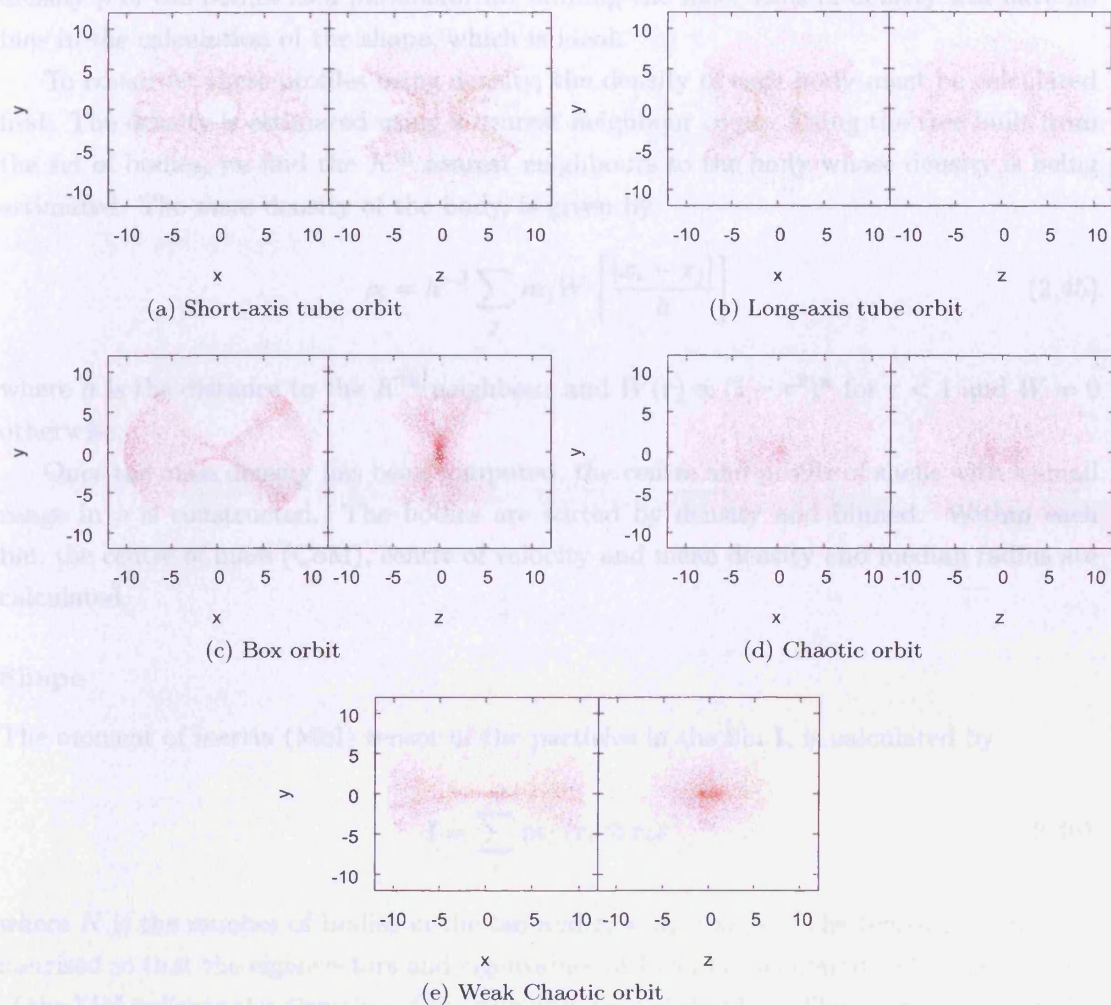


Figure 2.1: Typical examples of each individual orbit types and the weak chaotic orbit which are due to the anisotropic potential used. Each point is taken from the orbit equally spaced in time at a timestep of $1/2^5$.

2.9.2 Halo Profiles using Density

To construct a radial profile of various properties of a spherical halo, the usual method is to split the model into radial spherical bins and construct the profile from these spherical shells. When the shape is non-spherical, elliptical bins are used and the profile is constructed in the same way. This leads to a problem. If the shape of the halo is different from the method of binning, then a bias is introduced in the analysis. In this thesis, the haloes are triaxial and in evolved models (ie. after mergers) the axis ratios evolve within the halo so binning the halo to a certain shape is not ideal. It is more ideal to use the

density ρ of the bodies as a parameter for binning the halo. Bins of density will have no bias in the calculation of the shape, which is ideal.

To construct these profiles using density, the density of each body must be calculated first. The density is estimated using a nearest neighbour count. Using the tree built from the set of bodies, we find the K^{th} nearest neighbours to the body whose density is being estimated. The mass density of the body, is given by

$$\rho_i = h^{-3} \sum_j m_j W \left[\frac{|x_i - x_j|}{h} \right] \quad (2.45)$$

where h is the distance to the K^{th} neighbour and $W(r) \propto (1 - r^2)^n$ for $r < 1$ and $W = 0$ otherwise.

Once the mass density has been computed, the centre and profile of shells with a small range in ρ is constructed. The bodies are sorted by density and binned. Within each bin, the centre of mass (CoM), centre of velocity and mean density and median radius are calculated.

Shape

The moment of inertia (MoI) tensor of the particles in the bin \mathbf{I} , is calculated by

$$\mathbf{I} = \sum_i^N m_i (\mathbf{r}_i \otimes \mathbf{r}_i) \quad (2.46)$$

where N is the number of bodies in the bin and $\mathbf{r}_i = \mathbf{x}_i - \mathbf{x}_{CoM}$. The tensor is then symmetrised so that the eigenvectors and eigenvalues of \mathbf{I} can be calculated. The eigenvectors of the MoI indicate the direction of the principle axes of that bin. The eigenvalues give the magnitude of principle axes of the density bin. The eigenvectors and eigenvalues are found by using the iterative Jacobi eigenvalue algorithm (Jacobi, 1846). The Jacobi algorithm diagonalises a symmetrised matrix from iterative rotations of the matrix. The diagonal of the final matrix are the eigenvalues and the c/a and b/a axis ratios are calculated.

Rotation and Dispersions

We may also find the direction of the rotation vector (if one exists) along with the mean velocities and dispersions in the radial, azimuthal and meridional direction.

First we define the unit vectors in these directions. The rotation vector is simply the direction of the angular momentum vector. Hence, the unit vector is

$$\mathbf{e}_{rot} = \frac{\sum_i^N m_i (\mathbf{e}_{r,i} \times \mathbf{v}_i)}{|\sum_i^N m_i (\mathbf{e}_{r,i} \times \mathbf{v}_i)|} \quad (2.47)$$

where $\mathbf{e}_{r,i} = \mathbf{r}_i/|\mathbf{r}_i|$ is the unit vector in the radial direction of the i th particle. The azimuthal \mathbf{e}_ϕ , and meridional \mathbf{e}_θ unit vectors are given as

$$\mathbf{e}_\phi = \frac{\mathbf{e}_r \times \mathbf{e}_{rot}}{|\mathbf{e}_r \times \mathbf{e}_{rot}|}, \quad \mathbf{e}_\theta = \frac{\mathbf{e}_r \times \mathbf{e}_\phi}{|\mathbf{e}_r \times \mathbf{e}_\phi|}. \quad (2.48)$$

With these unit vectors we may now calculate the velocity dispersions in these directions. They are given by

$$\sigma_r = M^{-1} \left(M \sum_i^N m_i (\mathbf{e}_{r,i} \cdot \mathbf{v}_i)^2 - \left[\sum_i^N m_i (\mathbf{e}_{r,i} \cdot \mathbf{v}_i) \right]^2 \right)^{1/2} \quad (2.49)$$

$$\sigma_\phi = M^{-1} \left(M \sum_i^N m_i (\mathbf{e}_{\phi,i} \cdot \mathbf{v}_i)^2 - \left[\sum_i^N m_i (\mathbf{e}_{\phi,i} \cdot \mathbf{v}_i) \right]^2 \right)^{1/2} \quad (2.50)$$

$$\sigma_\theta = \left(M^{-1} \sum_i^N m_i (\mathbf{e}_{\theta,i} \cdot \mathbf{v}_i)^2 \right)^{1/2} \quad (2.51)$$

where $M = \sum_i^N m_i$.

The orbital decay of satellites may be used as a probe of the shape of the underlying dark matter halos in galaxies. As the shape of these halos may be triaxial, we investigate how triaxiality affects the orbital decay of satellites. We compare the results with a spherical halo, as spherical halos are usually used in investigations of this kind. Triaxial potentials have a much richer orbital structure, the way in which the different orbits affect the infall time is also investigated.

3.1 Introduction

The Milky Way galaxy has numerous satellite galaxies orbiting around it; the closest of these is the Large Magellanic Cloud (LMC), which is a satellite galaxy of the Milky Way. The LMC has been disrupted along the orbital path, and has formed a ring around the Milky Way. Numerical modelling of the orbit around of Sagittarius has been used to constrain the shape of the Milky Way DM halo.

Duffy et al. (2011) and Johnston et al. (2015) reported that the narrow width of the

3

Orbital Decay of a Satellite Galaxy in a Triaxial

Halo

Whirlpool Galaxy • M51



Hubble
Heritage

NASA, ESA, S. Beckwith (STScI), and The Hubble Heritage Team (STScI/AURA) • Hubble Space Telescope ACS • STScI-PRC05-12a

The orbital decay of satellites may be used as a probe of the shape of the underlying dark matter haloes in galaxies. As the shape of these haloes may be triaxial, we investigate how triaxiality affects the orbital decay of satellites. We compare the results with a spherical halo, as spherical models are mostly used in investigations of this kind. Triaxial potentials have a much richer orbital structure, the way in which the different orbits affect the infall time is also investigated.

3.1 Introduction

The Milky Way galaxy has numerous satellite galaxies orbiting around it, the closest of which is the Sagittarius (Sgr) dwarf galaxy. The present-day proximity of Sgr to the Milky Way means that it is currently experiencing significant tidal disturbance. Tidal debris from Sgr has been dispersed along its orbital path, and has formed a tidal stream around the Milky Way. Numerical modelling of the tidal stream of Sgr has been used to constrain the shape of the Milky Way DM halo.

Ibata et al. (2001) and Johnston et al. (2005) proposed that the narrow width of the Sgr stream suggests that the DM halo is close to spherical because the apparent precession of the stream is small. Helmi (2004a,b) argued that the trailing stream is dynamically young and so has not had time to undergo differential precession and thus cannot provide a stringent constraint on the halo shape. However the leading arm, which is dynamically older, can be best fit using a prolate halo with a $c/a \approx 0.6$ (Helmi, 2004a,b). Law et al. (2005) found that the velocities of stars in the leading stream can only be fit with a prolate halo but the precession of the leading stream with respect to the trailing stream can only be fit with an oblate halo. Fellhauer et al. (2006) tried to model the Sgr stream from data in the Sloan Digital Sky Survey (SDSS) (Belokurov et al., 2006). The best fitting model was found to be an almost spherical halo. However, they could not model the both the precession rate and the velocities in the leading arm with a single model. Recently, Law et al. (2009) claimed that they could fit the observed trailing arm velocities, the angular coordinates and radial velocities of the leading arm by using a (fixed) triaxial potential with $c/a = 0.67$ and $b/a = 0.83$.

There is thus no consensus on the shape of the Milky Way halo from the observed studies, with the different analyses and data sets yielding different flattenings.

As the shape of the Milky Way DM halo is possibly triaxial, we will study the effect of triaxiality on the decaying orbit of an infalling satellite. Since the infalling satellite will also have an effect on the halo which will in turn have some feedback on the satellite and its orbit, it is important to have a live halo in our simulations, which can react to the infalling satellite. In this chapter will investigate the infall times of a satellite galaxy into a triaxial shaped DM halo. We will describe a suite of N -body simulations of the orbit of

a satellite modelled as a rigid, softened point-mass. The satellite trajectory decays to the centre of the host halo due to dynamical friction. The satellite starts on a certain orbit and as its trajectory into the centre of the halo is a consequence of it moving from one orbit to another we refer to this process in the chapter as orbital decay.

In previous studies of this problem, the halo shape has usually been assumed to be spherical and so the initial placement of the satellite is inconsequential due to the spherical symmetry. In the triaxial case, the initial position of the satellite becomes more important. The initial orbit the satellite is on depends on this initial position and velocity because of the asymmetry of the underlying potential. Whereas in a spherical halo there is only one type of orbit, in a triaxial halo there are four main families of orbit: box, long-axis tube, short-axis tube and chaotic orbits (see Section 1.4.2). We investigate how these different orbital families can affect the infall time of a satellite and which of the orbital properties determine the infall time of the satellite. The affect of the flattening of the halo on the infall time of a satellite will also be investigated.

Orbital decay is important because it affects predictions of when the Milky Way's satellite galaxies will be accreted or whether they are even bound to the Milky Way. Halo triaxiality can also affect how the satellite will be accreted to the galaxy, which can have consequences for galactic disks and cores and also the feeding of Active galactic nuclei (AGN).

3.2 Initial Conditions

3.2.1 Dark Matter Halo

The N -body realisations of the parent galaxy haloes used in these simulations were constructed using Dehnen's (2009) made to measure method as described in Section 2.8. The models use the truncated dark matter profile as described in Dehnen & McLaughlin (2005), which were shown to have excellent agreement with simulated dark matter profiles. The halo models thus follow the density profile

$$\rho(r) \propto \left(\frac{m}{r_s}\right)^{-7/9} \left[\left(\frac{m}{r_s}\right)^{4/9} + 1 \right] \operatorname{sech} \frac{m}{r_t}, \quad (3.1)$$

where r_s is the scale radius of the halo and m is the triaxial radius, given by

$$m^2 \equiv \frac{x^2}{a^2} + \frac{y^2}{b^2} + \frac{z^2}{c^2}, abc = 1. \quad (3.2)$$

In all the models the total mass of the halo $M = 1$, and the scale radius $r_s = 1$. The models were truncated at the approximate virial radius $r_t = 10r_s$. The N -body model contains a total number of 10^6 bodies. Table 3.1 shows the different models that are used

Model	c/a	b/a
DM00	1	1
DM53	0.5	0.7
DM32	0.7	0.8

Table 3.1: Initial model axis ratios.

in the simulations. Our two triaxial models were chosen to have very similar triaxialities (Section 1.4.1) but with one model being flatter than the other so that the axis ratios of the models are different. The triaxiality parameter (Equation 1.2) value was chosen from Bailin & Steinmetz (2005), who looked at the triaxiality of ~ 4000 haloes formed from a cosmological simulation. They defined the haloes to be near oblate when $0 < T < \frac{1}{3}$, triaxial when $\frac{1}{3} < T < \frac{2}{3}$ and near prolate when $\frac{2}{3} < T < 1$. The majority of haloes were either triaxial or prolate (Figure 1.7) so we decided to have a triaxiality that was close to $T = \frac{2}{3}$. The halo models are denoted in a similar way to how elliptical galaxies are classified. The model classification is related to the axis ratios by the simple equation

$$DMxy, \quad \text{where } x = 10 \left[1 - \frac{c}{a}\right] \text{ and } y = 10 \left[1 - \frac{b}{a}\right]. \quad (3.3)$$

DM53 is a flat triaxial model with $c/a = 0.5$ and $b/a = 0.7$, and so $T = 0.68$. While DM32 is a rounder model with $c/a = 0.7$ and $b/a = 0.8$, therefore $T \approx 0.7$. The model DM00 is spherical halo. Figure 3.1 shows the density profile (ρ), velocity anisotropy (β), and the axis ratios (c/a and b/a) of all the initial models after they had been constructed. The values were calculated as outlined in Section 2.9.2. With Dehnen's (2009) made to measure method, it is also possible to constrain the β profile of the halo. Binney's anisotropy parameter β , quantifies the anisotropy of the velocity distribution and is given by

$$\beta = 1 - \frac{\sigma_\theta^2 + \sigma_\phi^2}{2\sigma_r^2} \quad (3.4)$$

where σ_θ , σ_ϕ and σ_r are the velocity dispersions in the meridional, azimuthal and radial directions respectively. However, here the β profile is left unconstrained during the made to measure process. The flatter triaxial model DM53 becomes increasingly radially anisotropic at large radii while the rounder triaxial model DM32 has a constant radial anisotropy and the spherical model is isotropic.

3.2.2 Satellite and Orbital Setup

The satellite was modelled as a heavy particle with a mass of 0.01 and an increased softening length, $\epsilon = 0.15$ (compared to $\epsilon = 0.01$ for the halo particles). As described in

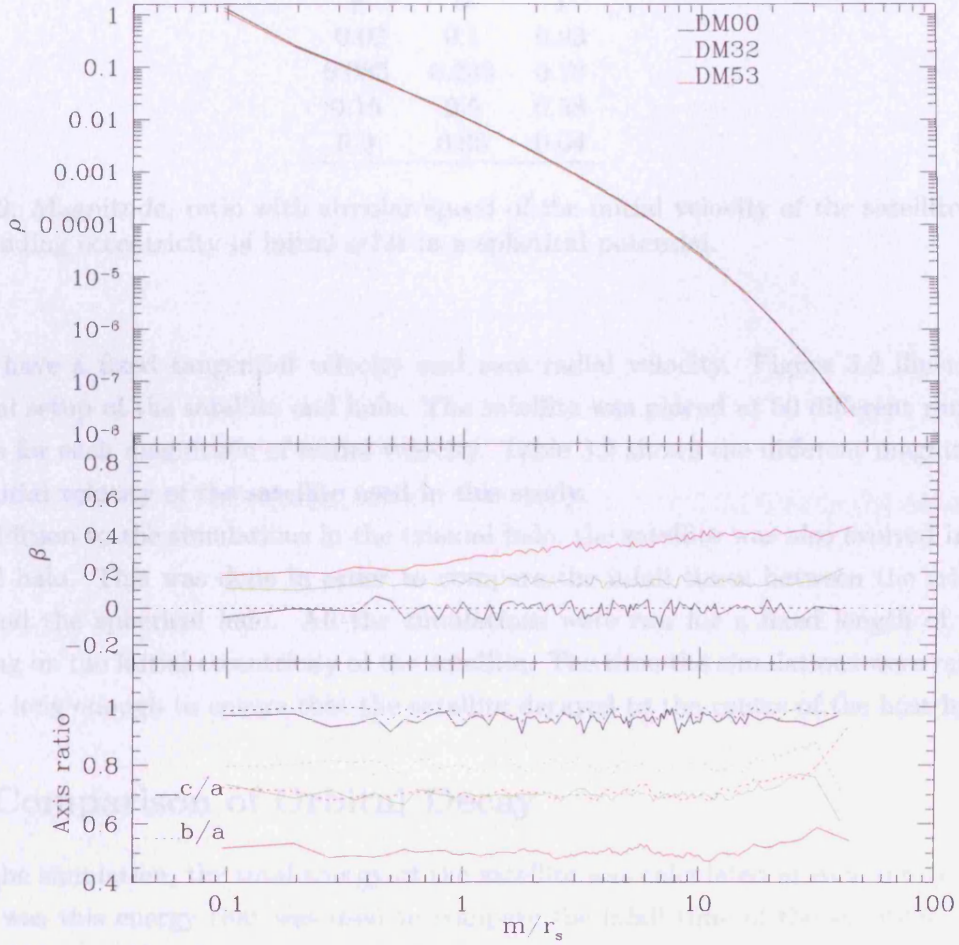


Figure 3.1: Density (ρ), velocity anisotropy (β) and axis ratio profiles of the all the initial models constructed with the M2M method. Due to the method of density estimation the density of the innermost and outermost data points is slightly overestimated.

Section 2.3, the softening kernel is one which follows the profile

$$\rho_{\text{soft}} \propto (1 + r^2/\epsilon^2)^{-7/2}. \quad (3.5)$$

So the satellite can be thought of as having the above density profile.

For the simulations the satellite was initially placed at the truncation radius of the halo, with a random azimuthal angle from the x -axis (ϕ) and polar angle from the z -axis θ , which is random in $\cos\theta$, and so it will start at a random point on a quadrant of the halo. The satellite was given a initial tangential velocity in the direction defined by the random angle α where $\alpha = 0$ is toward the z axis of the halo and so the satellite will

v	v/v_{circ}	e_{sph}
0	0	1
0.03	0.1	0.93
0.085	0.283	0.78
0.15	0.5	0.58
0.3	0.95	0.04

Table 3.2: Magnitude, ratio with circular speed of the initial velocity of the satellite and corresponding eccentricity of initial orbit in a spherical potential.

initially have a fixed tangential velocity and zero radial velocity. Figure 3.2 illustrates the initial setup of the satellite and halo. The satellite was placed at 50 different random positions for each magnitude of initial velocity. Table 3.2 shows the different magnitudes of the initial velocity of the satellite used in this study.

In addition to the simulations in the triaxial halo, the satellite was also evolved in the spherical halo. This was done in order to compare the infall times between the triaxial haloes and the spherical halo. All the simulations were run for a fixed length of time depending on the initial eccentricity of the satellite. The time the simulations were ran for was kept long enough to ensure that the satellite decayed to the centre of the host halo.

3.3 Comparison of Orbital Decay

During the simulation, the total energy of the satellite was calculated at each integration step. It was this energy that was used to compare the infall time of the satellites. The energy of the satellite falls as the satellites orbit is decaying because energy is being transferred from the satellite to the halo via dynamical friction. The dynamical friction is proportional to many properties. As the satellite is at pericentre the velocity of the satellite is higher than when it is at apocentre, this would mean that there is a greater frictional force felt by the satellite at pericentre. The left panel of Figure 3.3 shows the energy decay of a satellite which initially is on a highly radial orbit ($e_{\text{sph}} = 1$). As the figure shows, there is a sharp energy loss of the satellite orbit, which occurs when the satellite is at pericentre; the energy remains roughly constant for the rest of the orbit. The energy continues to drop at each pericentric passage as the satellite falls in until it plateaus at a constant value once the satellite has reached the centre. The infall time is the time measured at which the satellite reaches a certain energy value. The energy value at which the infall time is defined, is the same for all halo models but changes for each initial velocity. The example shown in the left hand panel of Figure 3.3 for $e_{\text{sat}} = 1$ the energy value chosen was -0.45. The right panel of Figure 3.3 shows the energy decay of a satellite for the case which initially is on a near circular orbit ($e_{\text{sph}} = 0.04$). The evolution

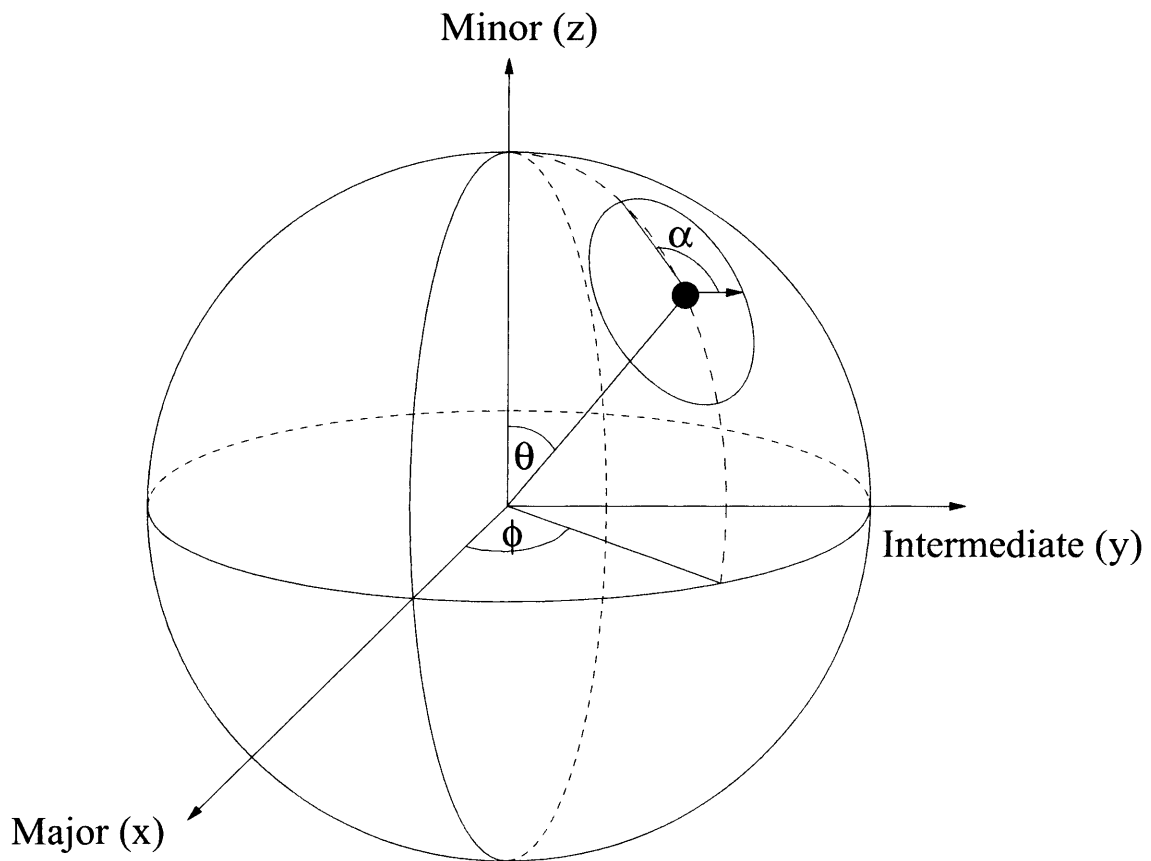


Figure 3.2: Initial setup of the position of the satellite with respect to the halo.

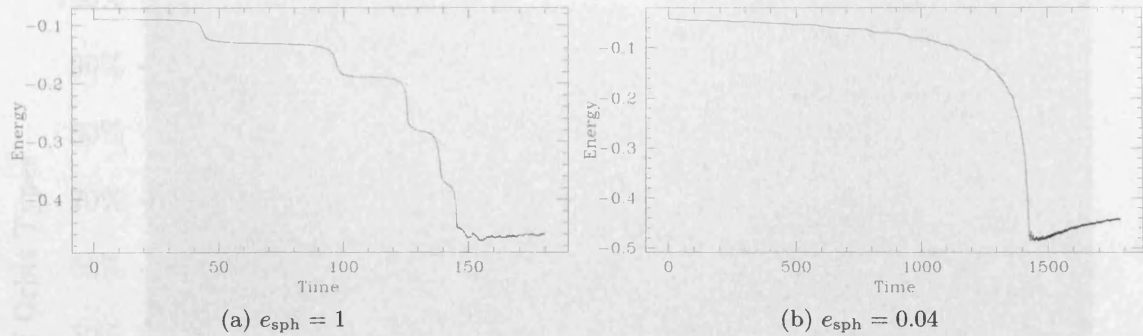


Figure 3.3: Time evolution of the total energy of a satellite as it decays to the centre of the triaxial halo DM53. The left panel shows the evolution when the initial eccentricity $e_{\text{sph}} = 1$ and the right panel when $e_{\text{sph}} = 0.04$.

of the orbital energy is somewhat different. There is no sharp energy loss at pericentre but rather a smooth decline in energy over the entire orbit as in a single orbit there is not a large variation in background halo density so the dynamical friction force does not vary greatly.

3.3.1 Dependence on Orbit Type in the Initial Conditions

As mentioned before, the initial angular position of a satellite of a given radius is not important in simulations with a spherical halo. This is because the satellite orbit will always be the same and only depends on the initial radius and velocity. This is not the case in the triaxial halo. The initial position has a bearing on the initial satellite orbit, along with the eccentricity, r and direction of the velocity. The initial orbital type could therefore have an effect on the infall time. Triaxial potentials support box orbits which are centrophilic (Section 1.4.2) and can get arbitrarily close to the centre which may reduce the infall time as they do not circulate around the centre like loop orbits. The type of orbit that the satellite initially will start on is highly dependent on the initial corresponding spherical eccentricity of the orbit. When the satellite is initially on a highly eccentric orbit, it is mostly likely to be on a box or chaotic orbit. As the eccentricity decreases, the angular momentum of the initial orbit increases and so the satellite is most likely to start on a loop orbit. Figure 3.4 shows the proportional of initial orbit type of a sample of 10000 test satellites placed randomly on a spherical surface (ie. same r) for different initial eccentricities. The method of orbit classification is described in Section 2.9.1.

There is also a slight dependence on the initial placement of the satellite. When the satellite is initially near the x - y plane (ie. when $\theta = 90$) and with low eccentricity, it will most likely start on a short-axis tube orbit. There are no short-axis tube orbits when $\theta < 30^\circ$. Long-axis tube orbits appear to be randomly spread and there is no definite

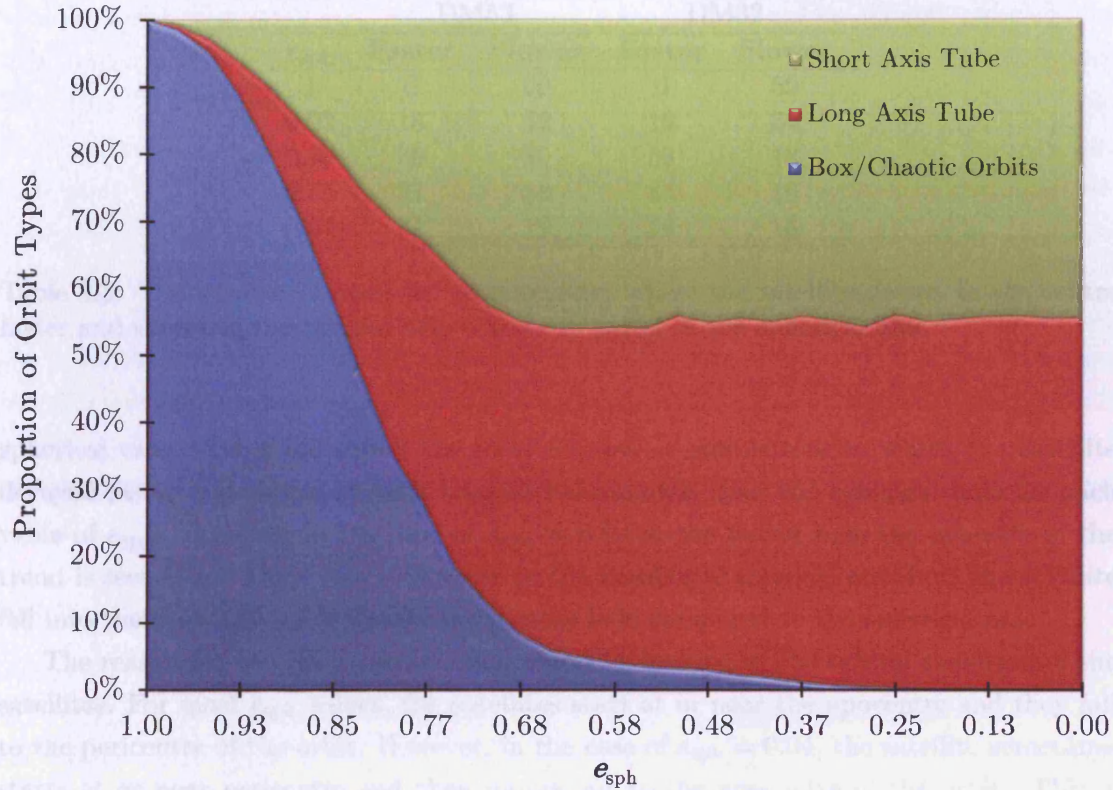


Figure 3.4: Proportion of orbit types as a function of e_{sph} in triaxial halo model DM53. Box and chaotic orbits are represented in blue, short-axis tube orbits are represented in green and long-axis tube orbits are represented in red.

dependence on initial position. This could explain why in Figure 3.4 at low eccentricities there is a slight preference of the satellite to start on a long axis tube orbit over short-axis tube orbits. At higher eccentricities, the satellite will tend to start on a box orbit when $\phi < 70^\circ$ and $\theta > 40$ and on boxlets when $\phi < 50^\circ$ and $\theta < 50^\circ$. At high eccentricities the initial orbits are dominated by chaotic and weakly chaotic orbits and they appear to be randomly orientated. There appears to be no correlation with the initial direction of the velocity and the type of orbit that the satellite is initially on.

3.4 Determination of Infall Time

When comparing the decay of the satellite in a triaxial halo with that in a spherical halo, e_{sph} has a large effect on the decay time. In the case where $e_{\text{sph}} = 1$ the satellite always decayed to the centre at a later time in the triaxial halo than in the spherical halo. As e_{sph} is reduced, the satellite decayed to the centre faster in the triaxial case than in the

e_{sph}	DM53		DM32	
	Faster	Slower	Faster	Slower
1	0	50	0	50
0.93	18	32	16	34
0.78	30	20	32	18
0.58	37	13	34	16
0.04	31	19	34	16

Table 3.3: The number of cases for each velocity where the satellite decays to the centre faster and slower in the triaxial halo when compared to the spherical halo

spherical case. Table 3.3 shows the total number of simulations in which the satellite decayed faster and slower in both triaxial halo models than the spherical halo for each value of e_{sph} . However, in the case of $e_{\text{sph}} = 0.04$ in the flatter halo the opposite of the trend is seen here. There was a decrease in the number of simulations where the satellite fell into the centre faster in the flatter triaxial halo compared to the spherical halo.

The reason for the effect can be understood by looking at the orbital evolution of the satellites. For most e_{sph} values, the satellites start at or near the apocentre and they fall to the pericentre of the orbit. However, in the case of $e_{\text{sph}} = 0.04$, the satellite sometimes starts at or near pericentre and then moves out to the apocentre of the orbit. This is because the initial eccentricities are calculated with respect to a spherical halo. In the triaxial halo, these eccentricity values are meaningless as the eccentricity can only be relevant to loop orbits while the orbits are actually evolving. Box orbits do not have an eccentricity because they do not circulate about the halo. The triaxial halo models are created using the criteria that $abc = 1$ which conserves the volume of the halo. At the initial radius of the satellite, the enclosed mass is lower in the triaxial haloes and this enclosed mass varies with ϕ and θ . Therefore, the initial velocity is greater than the circular speed for that interior mass, and that is why the orbits of the satellites are near pericentre initially. In the case of the flatter halo (DM53) the satellite's apocentre is further out and so it takes longer to fall into the centre from this point when compared with the rounder halo (DM32) and the spherical halo.

3.4.1 Dynamical Time

In trying to determine what affects the infall time of a satellite, we look at general properties of the initial orbit.

The difference in infall time for satellites at different initial positions and with different eccentricities could simply be because they have different orbit dynamical times. Figure 3.5 shows the ratio of infall time between the triaxial halo and spherical halo for both triaxial models against the ratio of dynamical time of the satellite in the triaxial halo and the

spherical halo. The infall and dynamical times in the triaxial haloes are normalised by the infall and dynamical times in the spherical halo, respectively. This is because they vary by a large amount for different values of e_{sph} . Using the normalisation, the relations can be analysed together. The dynamical time is calculated as the mean time between two sign changes of the radial velocity. This figure shows that the differences in infall time are not purely because of the different dynamical times. If this were the case then the points should lie on the 1:1 line. There is, however, a strong trend with the dynamical time, whose gradient reduces as e_{sph} is decreased. As there is a large spread in the points, there could be other properties, we now look for other properties of the initial orbit which are more closely related to the infall time. For the satellites on near circular orbits in halo model DM53 and initially on short-axis tube orbits, there are some points in Figure 3.5 that have a very low dynamical time. These satellites all start very close to the major axis of the halo as they have all values of $\phi < 13^\circ$.

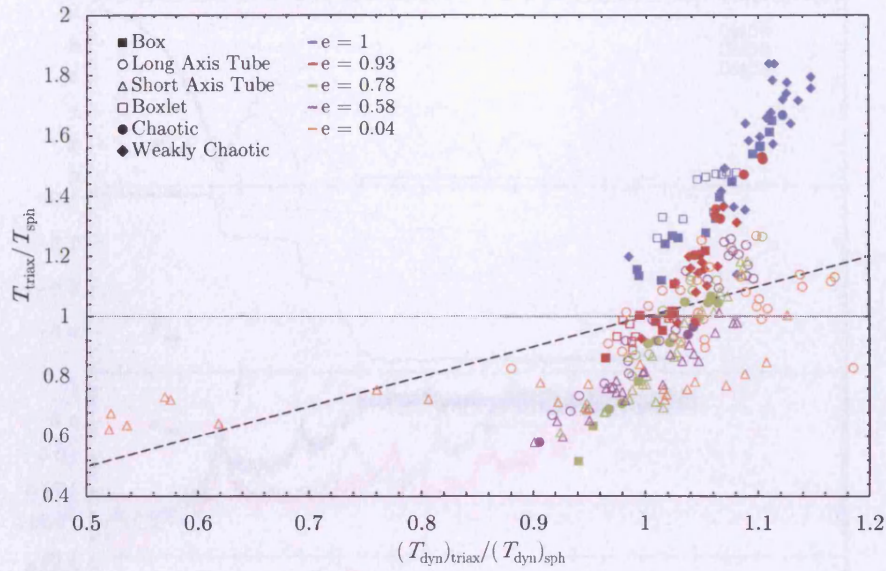
3.4.2 Density at Pericentre

We now explore whether the type of orbit that the satellite is on is a determining factor in the rate of decay. In a spherical halo, when $e_{\text{sph}} = 1$, the orbit is forced to go through the centre of the halo, and so will go through the densest region of the halo. The orbit will therefore decay faster as the frictional force is proportional to background density. This, however, is not the case for the satellite in a triaxial halo. As a satellite with e_{sph} is on a box orbit, it will miss the centre and so will take longer to decay to the centre. Figure 3.6 shows the evolution of the satellite's orbit in all three haloes for $e_{\text{sph}} = 1$ as it decays to the centre. The figure shows the time evolution of the radius of the satellite, the energy of the satellite, the local density of the halo at the location of the satellite and the angular momentum of the satellite. By looking at the calculated surrounding density of the satellite, it can be clearly seen that at the first pericentric passage the local density of the halo at the location of the satellite in the spherical halo is over an order of magnitude greater than in the triaxial halo. This suggests that the density has an important bearing on the decay time as the dynamical friction force on the satellite is strongest when it is at pericentre as the background density over the orbit is highest there.

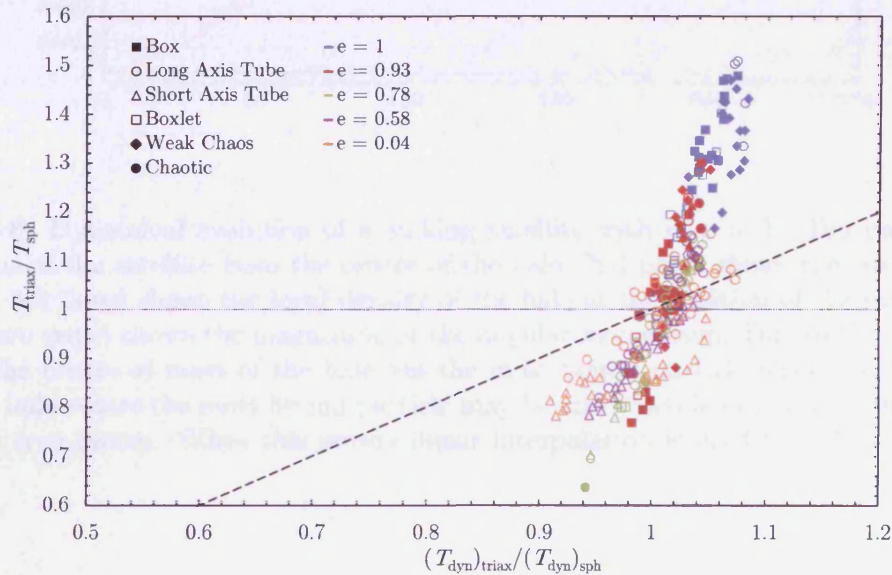
We now investigate the relationship between the infall time and the mean density of the halo at the pericentre over the evolution of the initial orbit of the satellite. First, we normalise the infall time of the satellite with the dynamical time to reduce the effect of the dynamical time. The normalised infall time is denoted by

$$\kappa = \frac{t_{\text{infall}}}{t_{\text{dyn}}}. \quad (3.6)$$

Figure 3.7 shows κ for all the satellites in the triaxial halo and spherical halo. In the



(a) DM53



(b) DM32

Figure 3.5: Ratio of time taken for the satellite to reach the centre in the triaxial halo over the spherical halo plotted against the ratio of dynamical time of the satellite in the triaxial halo over the spherical halo. The flatter triaxial halo model values are shown on top while the rounder triaxial halo model is shown on the bottom. The open point types denote orbits which are centrophobic and the filled point types denote orbits which are centrophilic.

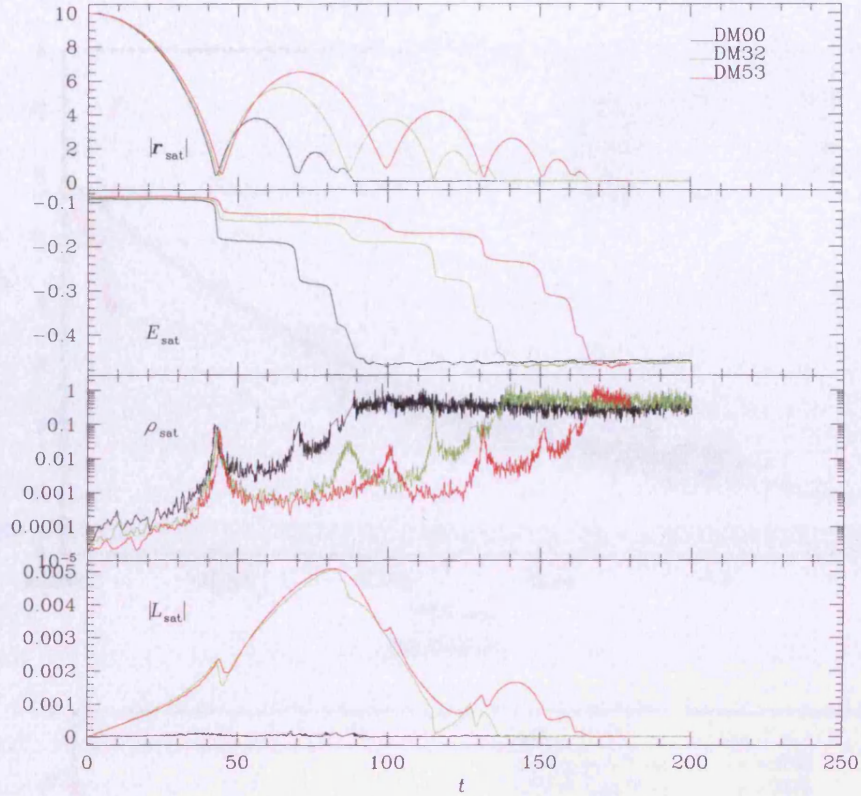


Figure 3.6: Dynamical evolution of a sinking satellite with $e_{\text{sph}} = 1$. Top panel shows the radius of the satellite from the centre of the halo, 2nd panel shows the energy of the satellite, 3rd panel shows the local density of the halo at the position of the satellite and the bottom panel shows the magnitude of the angular momentum. Due to the method of finding the centre of mass of the halo via the most bound particle when the satellite is near the halo centre the most bound particle may be one which is near the satellite rather than the true centre. When this occurs linear interpolation is used to reduce the errors created.

spherical halo, $\langle \rho_{\text{DMperi}} \rangle$ is the same for all orbits at a given eccentricity. However in the triaxial halo the different orbits will have different $\langle \rho_{\text{DMperi}} \rangle$ due to the initial conditions of the satellite. We extrapolate the relation of κ and $\langle \rho_{\text{DMperi}} \rangle$ for the spherical halo by fitting a power-law profile to the points. Comparing the normalised infall time, κ for the spherical and triaxial haloes shows that the orbital decay for tube orbits is mostly more efficient in the triaxial haloes as for initial orbits with the same $\langle \rho_{\text{DMperi}} \rangle$, κ is slightly smaller in the triaxial haloes. However for all other types of orbit, the orbital decay tends to be more efficient in the spherical halo. For the satellites initially on loops orbits, it

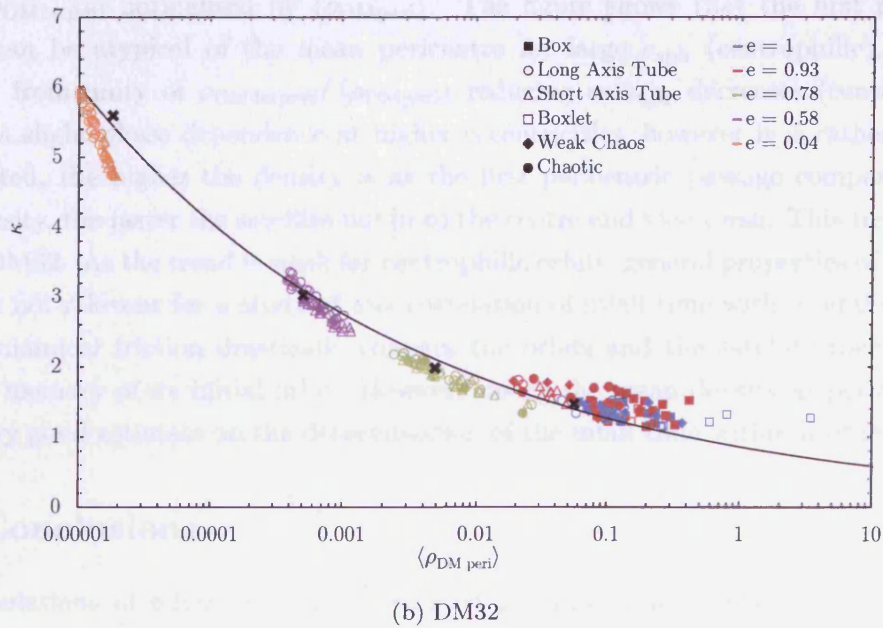
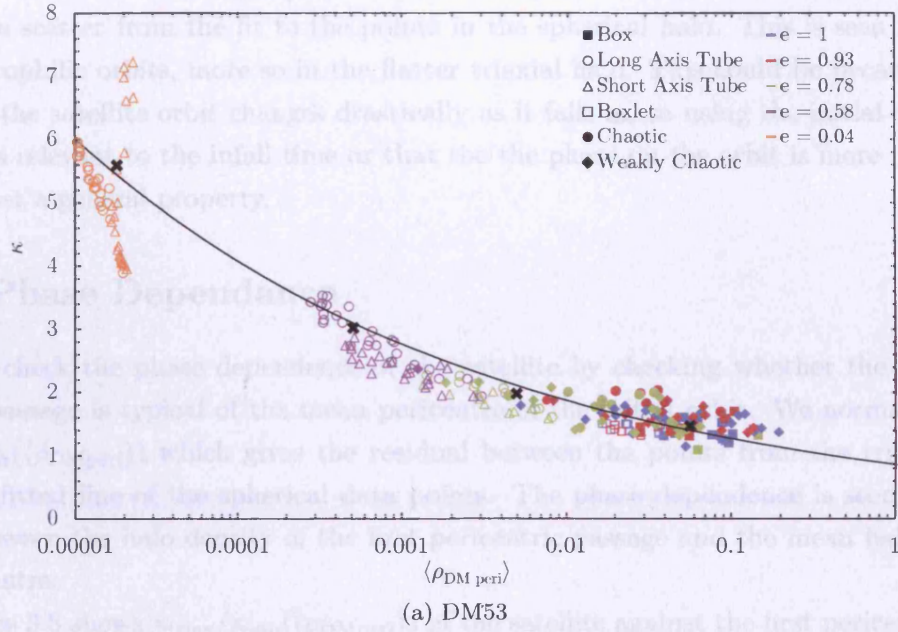


Figure 3.7: Figure of infall time normalised with dynamical time for all the satellites in the triaxial halo (coloured points) and spherical halo (black crosses) against the mean halo density at pericentre. The black curve shows a power-law best fit the spherical halo data points.

can be seen that the short-axis tube orbits decayed to the centre faster than the long axis tube. This is because the $\langle\rho_{\text{DMperi}}\rangle$ tends to be higher for the short-axis tubes. There is still some scatter from the fit to the points in the spherical halo. This is seen mostly in the centrophilic orbits, more so in the flatter triaxial halo. This could be because of two reasons; the satellite orbit changes drastically as it falls in, so using the initial orbit may not be as relevant to the infall time or that the phase on the orbit is more important rather just a general property.

3.5 Phase Dependence

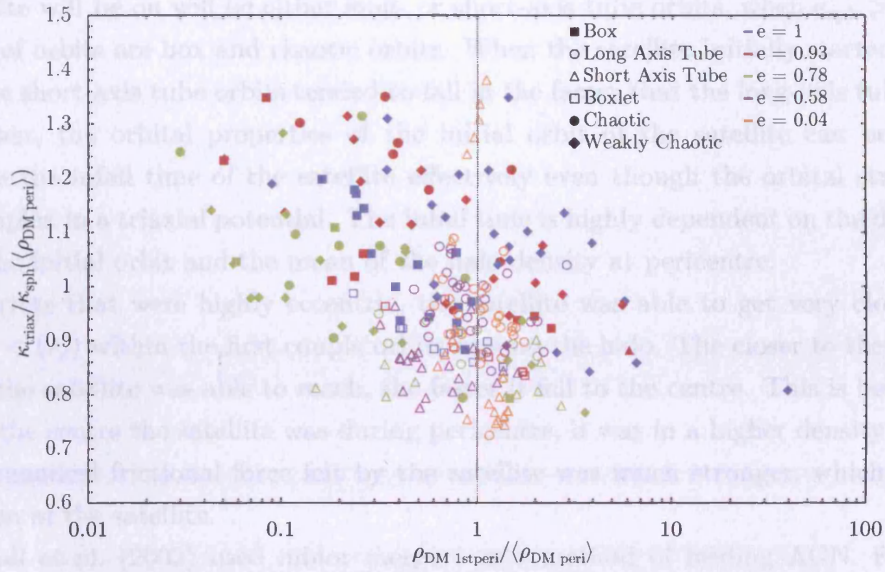
Now we check the phase dependence of the satellite by checking whether the first pericentric passage is typical of the mean pericentre of the initial orbit. We normalise κ_{triax} with $\kappa_{\text{sph}}(\langle\rho_{\text{DMperi}}\rangle)$ which gives the residual between the points from the triaxial halo and the fitted line of the spherical data points. The phase dependence is seen from the ratio between the halo density of the first pericentric passage and the mean halo density at pericentre.

Figure 3.8 shows $\kappa_{\text{triax}}/\kappa_{\text{sph}}(\langle\rho_{\text{DMperi}}\rangle)$ of the satellite against the first pericentric halo density $\rho_{\text{DM1stperi}}$ normalised by $\langle\rho_{\text{DMperi}}\rangle$. The figure shows that the first pericentric passage can be atypical of the mean pericentre for large e_{sph} (centrophilic), with the deviation from unity of $\rho_{\text{DM1stperi}}/\langle\rho_{\text{DMperi}}\rangle$ reducing as e_{sph} decreases (centrophobic). There is a slight phase dependence at higher eccentricities, however it is rather tenuous. As expected, the higher the density is at the first pericentric passage compared to the mean density, the faster the satellite fall in to the centre and vice versa. This trend is seen more in DM32. As the trend is weak for centrophilic orbits, general properties of the initial orbits are not relevant for a study of any correlation of infall time with orbital properties as the dynamical friction drastically changes the orbits and the satellite then does not have any memory of its initial orbit. However, using the mean density at pericentre can give a very good estimate on the determination of the infall time within a triaxial halo.

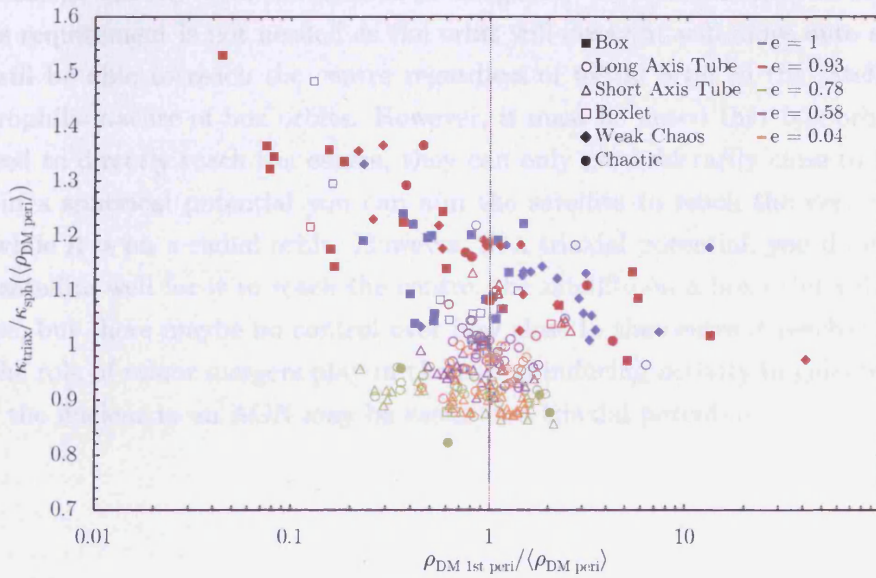
3.6 Conclusions

With simulations of minor mergers in isolated galaxies using a spherical DM halo the initial position of the satellite around the halo is not important, as the infall time is only dependent on r and the eccentricity of the orbit. When introducing a triaxial DM halo, the initial position becomes very important as this leads to the satellite having a different initial orbit which affects the infall time.

In a spherical halo, the satellite is simply on a loop orbit and will just decay in the orbital plane of its initial orbit. This is not the case in the triaxial halo. The potential created by the halo means that the satellite will be on different types of orbits, depending



(a) DM53



(b) DM32

Figure 3.8: Ratio of time taken for the satellite to reach the centre in the triaxial halo over the spherical halo plotted against the triaxial radius of the first pericentric pass of the satellite in the simulation.

on where it is started from and what the initial velocity of the satellite is. When the initial corresponding spherical eccentricity of the satellite $e_{\text{sph}} = 0.04$ the majority of orbits that the satellite will be on will be either long- or short-axis tube orbits, when $e_{\text{sph}} > 0.78$ the majority of orbits are box and chaotic orbits. When the satellite initially started on tube orbits, the short-axis tube orbits tended to fall in the faster than the long-axis tube orbits.

However, the orbital properties of the initial orbit of the satellite can be used to determine the infall time of the satellite effectively even though the orbital structure is more complex in a triaxial potential. The infall time is highly dependent on the dynamical time of the initial orbit and the mean of the halo density at pericentre.

For orbits that were highly eccentric, the satellite was able to get very close to the centre ($r < 1r_s$) within the first couple orbits around the halo. The closer to the centre of the halo the satellite was able to reach, the faster it fell to the centre. This is because the closer to the centre the satellite was during pericentre, it was in a higher density area and so the dynamical frictional force felt by the satellite was much stronger, which retarded the motion of the satellite.

Kendall et al. (2003) used minor mergers as a method of feeding AGN. For minor mergers to be a viable method of feeding AGN, they needed the initial orbit to be well aimed to merge directly with the nucleus of the galaxy. However in the case for a triaxial halo, this requirement is not needed as the orbit will decay, it will move onto a box orbit and so will be able to reach the centre regardless of initial orbit of the satellite due to the centrophilic nature of box orbits. However, it must be noted that box orbits are not guaranteed to directly reach the centre, they can only get arbitrarily close to the centre. So, within a spherical potential you can aim the satellite to reach the very centre of a galaxy, while it is on a radial orbit. However, in a triaxial potential, you do not need to aim the satellite well for it to reach the centre, the satellite on a box orbit will take it to the centre, but there maybe no control over how close to the centre it reaches. This may change the role of minor mergers play in the role of inducing activity in galactic nuclei as reaching the nucleus in an AGN may be easier in a triaxial potential.

In this chapter, some of observational consequences of the presence of triaxial dark matter haloes will be investigated.

Polar ring galaxies are systems which consist of a central galaxy encircled by a highly inclined whose apparent major or minor axis coincides with the apparent minor axis of the central galaxy. These polar ring galaxies can be used as probes of the triaxial nature of dark matter haloes (Klein & Smecker-Mehner, 1993).

These have been being recent observations of the central regions of elliptical galaxies which often have a concentration of elongated structure and also have a concentration of stars. It has been shown that these features can be the result of a merger (Klein & Smecker-Mehner, 1993; Kormendik, 1988). In this chapter, simulations of the orbital dynamics of a satellite galaxy in a (possibly triaxial) elliptical galaxy embedded in a triaxial dark matter halo.

4

Dynamical Friction in Flattened Haloes

4.1. Intro

Binary AGN
The two AGN
(Seyfert 2)
The separation
(400 pc)
Seyfert 2
Klein & Smecker-Mehner

4.1.2. Kin

The velocity
with respect
to the galaxy
is 100 km/s
(1988). The
velocity of the
satellite galaxy
is 100 km/s
relative to the
galaxy. The
velocity of the
satellite galaxy
is 100 km/s
relative to the
galaxy.



Polar-Ring Galaxy NGC 4650A

PRC99-12
Space Telescope Science Institute
Hubble Heritage Team (AURA/STScI/NASA)

Hubble Heritage

In this chapter, some of observational consequences of the presence of triaxial dark matter haloes will be investigated.

Polar ring galaxies are systems which consist of a central galaxy encircled by a bright annulus whose apparent major axis nearly coincides with the apparent minor axis of the central galaxy. These polar ring galaxies can be used as probes of the triaxial nature of dark matter haloes (Cox & Sparke, 1996).

There have been many recent observations of the central regions of elliptical galaxies which often have a kinematically decoupled component and also have a coplanar gas disc and it has been shown that these features can be the result of a merger (Hernquist & Barnes, 1991; Kormendy, 1984). In this chapter, simulations of the orbital decay of a satellite galaxy in a triaxial dark matter halo will be analysed and the properties of the orbit will be investigated to see if it is possible for the aforementioned phenomena to be created via the accretion and/or tidal disruption of a satellite galaxy in a (possibly triaxial) elliptical galaxy embedded in a triaxial dark matter halo.

4.1 Introduction

Binney (1976, 1978) showed that elliptical galaxies may be intrinsically triaxial in shape. This was based on the observations of the slow bulk rotation of the stellar distribution (Bertola & Capaccioli, 1975; Illingworth, 1977), the presence of velocity gradients along the apparent minor axis (Schechter & Gunn, 1978) and evidence from N -body simulations (Aarseth & Binney, 1978). Dynamical modelling from observational data of isophotal twists and velocity fields of elliptical galaxies have been best fit by triaxial models (Buote et al., 2002; Statler et al., 2004).

4.1.1 Kinematically Decoupled Cores

The discovery by Efstathiou et al. (1982) of an elliptical galaxy (NGC 5813) with a kinematically decoupled core (hereafter KDC, Figure 4.1) along with other observations of more ellipticals with KDCs (Bender, 1988; Franx & Illingworth, 1988; Emsellem et al., 2004) showed that KDCs are found in a large fraction of early-type galaxies. Some of the ellipticals with KDCs have been found to have counter-rotating cores (Franx & Illingworth, 1988). The most widely accepted explanation for the formation of KDCs in elliptical galaxies is the merger of a compact secondary with a giant elliptical (Kormendy, 1984; Balcells & Quinn, 1990; Balcells, 1992). In this scenario, the secondary sinks to the nucleus by dynamical friction and if the orbital angular momentum is not aligned with the initial angular momentum of the elliptical galaxy then a KDC is formed. Merger simulations give a good description of the observed peculiar core kinematics. There are observations of KDCs which cannot be explained with a single merger event. IC1459 is one such example,

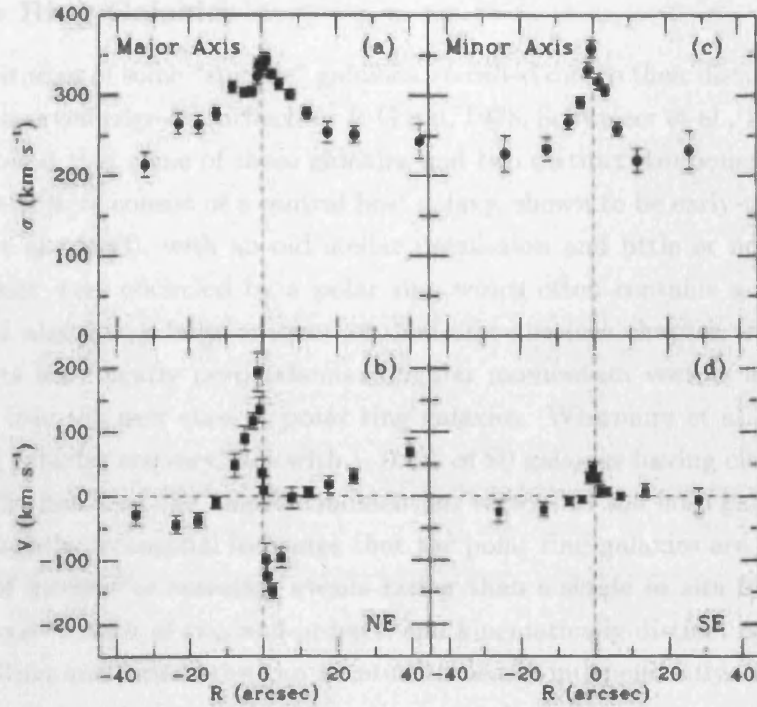


Figure 4.1: Figure from Franx & Illingworth (1988) showing the stellar velocity dispersion and radial velocity profiles of IC 1459 along the major axis (*a*, *b*) and along the minor axis (*c*, *d*).

which has a slowly rotating stellar halo with a counter-rotating core and a gaseous component which rotates in the same sense as the stellar halo (Franx & Illingworth, 1988). The observable kinematics of a triaxial system is very rich (Statler, 1991), the phenomenon of counter-rotating KDCs could be explained if the elliptical galaxies are embedded in triaxial dark matter haloes.

Many observed elliptical galaxies contain gas disks in their inner parts (Emsellem et al., 2004). These discs are always aligned with the equatorial plane of the elliptical halo. Some of the ellipticals have strongly misaligned photometric and kinematic axes, which indicates a non-axisymmetric structure (Emsellem et al., 2004). Numerical simulations have shown that from gas-rich 1:1 to 2:1 disc mergers a new stellar disc component can be created from star formation in the gas which settled into the equatorial plane of the merger remnant (Barnes & Hernquist, 1992; Naab & Burkert, 2001). Gas can also be transported to the centre of an elliptical galaxy via accretion of a satellite containing cold gas (Khochfar & Burkert, 2005). Although there is no gas in the simulations we have undertaken, the orbit of the satellite could give an indication of the behaviour of the debris from a disrupted satellite, which may enable us to infer the possible gas distribution after the merger.

4.1.2 Polar Ring Galaxies

Observational studies of some “spindle” galaxies, so called due to their distinctive shape on the sky when observed edge-on (Schechter & Gunn, 1978; Schweizer et al., 1983; Whitmore et al., 1987), found that some of these galaxies had two distinct components at the same redshift. These objects consist of a central host galaxy, shown to be early-type S0 galaxies (Hagen-Torn et al., 1983), with an old stellar population and little or no gas and dust. The host galaxies were encircled by a polar ring which often contains a younger stellar population and also has a large amount of dust and gas (see chapter title page). The two components have nearly perpendicular angular momentum vectors and the objects were classified into the new class of polar ring galaxies. Whitmore et al. (1990) showed that polar ring galaxies are very rare with $\sim 0.5\%$ of S0 galaxies having clearly detectable polar rings. The fact that the angular momentum vectors of the host galaxy and of the polar ring are nearly orthogonal indicates that the polar ring galaxies are most likely the end products of mergers or accretion events rather than a single *in situ* formation event. Polar ring galaxies consist of two well-ordered and kinematically distinct components and so the composition and kinematics can be studied nearly independently. This provides a unique opportunity to study galaxy interactions as other merger remnants are generally very disordered systems.

Since the polar rings of these galaxies extend well beyond the visible part of the host galaxy, they provide excellent probes of the surrounding dark matter halo of the galaxy. In a static axisymmetric potential, non-precessing loop orbits stay in the equatorial plane. Orbits which are not in this plane will precess about this plane except if the orbit passes through the potential’s symmetry axis (polar orbit). The plane in which the orbit is non-precessing we will refer to as the preferred plane. In a static triaxial potential, the preferred planes are perpendicular to the long- and short-axis (Athanasoula & Bosma, 1985). Most polar rings are very nearly kinematically orthogonal to their host galaxies, although intrinsic inclinations between 10 and 35 degrees from polar are also fairly common (Whitmore, 1984). In an axisymmetric potential, the orbits of an inclined polar ring will suffer from differential precession as the orbital times are longer at larger radii. However, most polar rings appear to be planar and there is no clear evidence of differential precession (Whitmore, 1984). A triaxial potential could reduce this differential potential and so could explain why there appears to be no warping observed in polar ring galaxies.

Studies of satellite orbital decay in spherical dark matter haloes have shown that the Chandrasekhar (1943) dynamical friction formula (Section 1.6) is a good approximation (Velazquez & White, 1999). However, in triaxial systems, the standard Chandrasekhar formula does not accurately reproduce the decay of a satellite (Statler, 1991; Peñarrubia et al., 2002). This is primarily due to the fact that the Chandrasekhar formula assumes an isotropic velocity distribution while triaxial equilibrium models inevitably have anisotropic

velocity distributions (Merritt, 1980; Moore et al., 2004; Dehnen, 2009). Statler (1991) showed in an analytical study that, in the case of Stäckel potentials (Section 1.4.2), the velocity anisotropy produces strong effects on the satellite orbit. Binney (1977) extended the Chandrasekhar formula to take into account the velocity anisotropy of an axisymmetric model. His formulation reduces to the Chandrasekhar formula for an isotropic velocity distribution. Using full N -body simulations, Peñarrubia et al. (2004) varied the value of $\ln \Lambda$ to minimise the χ^2 difference of the decaying orbit from numerical simulations to the orbit predicted by the dynamical friction formula of Binney and Chandrasekhar. They found that the prediction from Binney’s formulation of orbital decay in an oblate spheroid produces a much lower χ^2 error than the standard Chandrasekhar formula. Binney (1977) also showed that in an oblate axisymmetric potential, a body will suffer a decrease in orbital inclination as it decays. This is due to the body experiencing a larger drag force in the direction of the axis perpendicular to the preferred plane than the drag force in the axisymmetry plane. This result was also reproduced by Peñarrubia et al. (2004).

In this chapter, the evolution of the decaying orbit of a satellite in a flattened triaxial halo will be investigated. The difference in the decay of orbit inclination in a triaxial halo and axisymmetric halo is potentially significant as the velocity dispersion profiles will differ between the two models and so the effect of dynamical friction on the satellite’s orbit will be different and will also change the nature of the orbit. This could be important for the transport of gas into the centre of elliptical galaxies where gas discs are always found to be in the equatorial plane. Finally, the effect of changing the mass of the satellite will be investigated both in terms of dynamical friction timescales and the nature of the decaying orbit.

It is also important to see that these observational phenomena mentioned can be created using a triaxial halo as cosmological simulations have showed that the intrinsic shapes of dark matter haloes are triaxial (Section 1.3). If the richer orbital structure within a triaxial potential prevents these phenomena from existing, then this would be a huge hurdle of our understanding of dark matter haloes.

4.2 Decay to the Equatorial Plane

From the simulations in Chapter 3, it was seen that when the satellite orbit was initially near circular orbit, it almost always decays to the most preferred plane perpendicular to the short-axis. We assume the orbital plane to have decayed to the equatorial plane when the orbital plane is within 15° of the equatorial plane as measured by the direction of the angular momentum vector. For other initial orbits, the infall timescale is much shorter than the timescale of the decay to the equatorial plane and so the orbit of the satellite does not decay all the way to the equatorial plane but there is still a decay away from

the original orbital plane. In a spherical dark matter halo, the plane of the satellite's orbit stays constant in simulations of the decaying orbit, due to conservation of angular momentum.

The evolution of the satellite orbit is very different in triaxial haloes than in spherical haloes. In both triaxial halo models considered here (DM53 and DM32, see Section 3.2), the final orbital plane in most simulations tends to be in the equatorial plane when the satellite orbit has decayed to the centre and is initially on a near circular orbit. Figure 4.2 shows an (equal-area) Aitoff projection of the direction of the angular momentum vector of the satellite for three sets of simulations. In each set of simulations, the initial conditions of the satellite are the same but the orbit of the satellite is shown for both the triaxial models. The direction of the angular momentum gives the direction of the orbital plane as the angular momentum vector is always perpendicular to that plane. As expected, by the end of the simulations the angular momentum vectors are pointing towards either the positive or negative minor axes of the halo, which means that the plane of the orbit is in the equatorial plane of the halo. The rate at which the momentum vector moves to the minor axis is faster in the flatter halo than in the rounder triaxial halo. This is because of the velocity anisotropy of the halo particles; the flatter halo has a larger anisotropy which exerts a larger “torque” on the satellite due to the anisotropy of dynamical frictional drag forces (Binney, 1977), moving the orbit to the equatorial plane. Statler (1991) found, using Säckel potentials, that along the direction in which the halo is cold, the frictional force increases. In a triaxial halo, globally $\sigma_x^2 > \sigma_y^2 > \sigma_z^2$ and so the frictional force will be strongest in the z direction which leads to the decay to the equatorial plane. This effect of anisotropy can be easily tested. By comparing the evolution of the momentum vector in the simulation with the evolution of a decay of a satellite in a static potential and a frictional force as prescribed by Chandrasekhar (1943). As Chandrasekhar's formulation assumes isotropy any effects due to anisotropy will not occur. Figure 4.3 shows the evolution of the angular momentum of a satellite in our full N -body simulation and using Chandrasekhar's friction formula in a semi-analytic manner. The momentum vector moves from precession about the long-axis to precessing about the short-axis in the N -body simulation while the momentum vector only precesses about the long-axis.

If the satellite is initially on a long-axis tube orbit, the angular momentum vector will initially precess about the long axis on a long axis tube orbit. The closer the vector is to the long axis the longer it will precess about this axis before it begins to precess about the minor axis of the halo and move onto a short axis tube orbit. In the flatter halo this change happens sooner than in the rounder triaxial halo. Thus, for some cases, the angular momentum is still precessing about the long axis at the end of the simulation. In these cases, when the satellite reaches the centre, the orbital plane has not decayed to the equatorial plane and remains nearer to the polar plane of the halo.

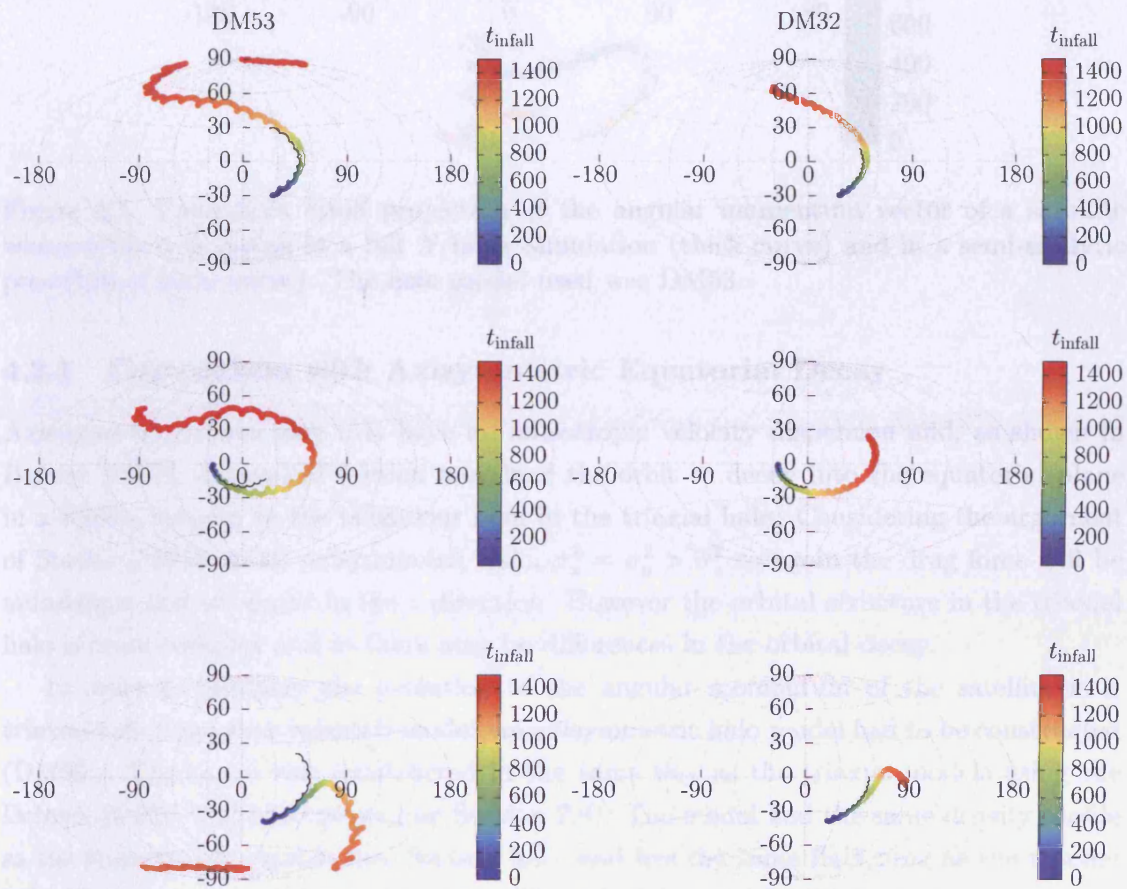


Figure 4.2: Equal-Area Aitoff projection of the angular momentum vector for three simulations (coloured curves). Left-hand figures show the evolution in the flatter triaxial halo (DM53) and the right-hand figures show the evolution in the rounder triaxial halo (DM32). The black curve shows the evolution of a non-decaying orbit. In these figures the longitude values of 0 and 180/-180 are in the direction of the positive and negative long-axis respectively. The longitude values of 90 and -90 are in the direction of positive and negative intermediate-axis, respectively and the latitude values of 90 and -90 are in the direction of the positive and negative short-axis.

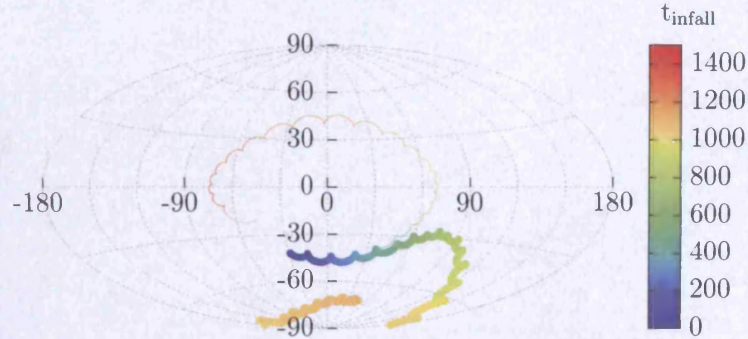


Figure 4.3: Equal-area aitoff projection of the angular momentum vector of a satellite whose orbit is decaying in a full N -body simulation (thick curve) and in a semi-analytic prescription (thin curve). The halo model used was DM53.

4.2.1 Comparison with Axisymmetric Equatorial Decay

Axisymmetric haloes may also have an anisotropic velocity dispersion and, as shown in Binney (1977), dynamical friction may lead the orbit to decay into the equatorial plane in a similar manner to the behaviour seen in the triaxial halo. Considering the argument of Statler (1991), in an axisymmetric halo, $\sigma_x^2 = \sigma_y^2 > \sigma_z^2$ so again the drag force will be anisotropic and strongest in the z direction. However the orbital structure in the triaxial halo is more complex and so there may be differences in the orbital decay.

In order to compare the evolution of the angular momentum of the satellite in a triaxial halo to an axisymmetric model, an axisymmetric halo model had to be constructed (DM50). The model was constructed in the same way as the triaxial models using the Dehnen (2009) M2M technique (see Section 2.8). The model had the same density profile as the triaxial halo models (see Section 3.2), and has the same flattening as the triaxial halo DM53 of $c/a = 0.5$ and $b/a = 1$. The triaxial model DM53 becomes increasingly radially anisotropic at large radii with $\beta = 0.2$ in the inner parts to $\beta = 0.4$ in the outer parts of the halo model. The triaxial model DM32 and the axisymmetric model both have constant radial anisotropy with $\beta \approx 0.1$. The 50 simulations from the previous chapter in which the initial velocity of the satellite was $e_{\text{sph}} = 0.04$ (where e_{sph} is the eccentricity of the orbit in a spherical potential with the same initial velocity, as before) were run with the satellites placed around the axisymmetric model and allowed to evolve until the orbits decayed to the centre of the halo.

As the preferred plane in an axisymmetric potential is the equatorial plane, all the satellite orbits decayed to this plane except those in which the satellite orbit was very close (within 10°) to a polar orbit, in which case it precessed about the minor axis and decayed only slightly away from a polar orbit within the timescale of the infall time. This is because the L_z component of the angular momentum vector is initially zero, or very small,

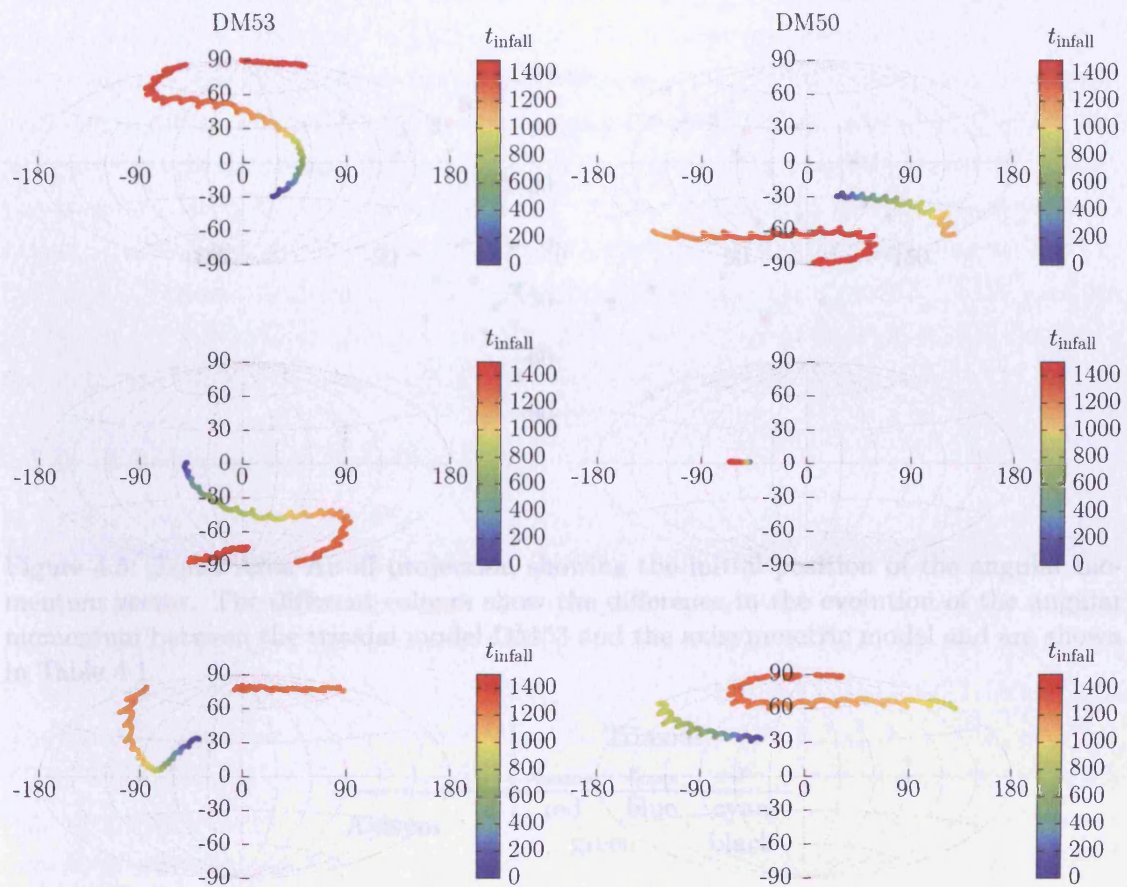


Figure 4.4: Equal-Area Aitoff projection of the angular momentum vector for three simulations. Left-hand figures show the evolution in the flatter triaxial halo (DM53) and the right-hand figures show the evolution in the axisymmetric halo (DM50).

and as this component is conserved in the axisymmetric potential, it remains zero or close to zero and stays in the same plane. This is in contrast to the case of a triaxial halo, where the L_z component can grow, and so the orbital plane can decay to the equatorial plane as both L_x and L_y decay. For all the other cases where the orbit of the satellite decays to the equatorial plane, the angular momentum vector of the satellite precesses around the z (minor)-axis. Figure 4.4 shows the evolution of the angular momentum vector in an equal-area Aitoff projection in the triaxial halo model DM53 and the axisymmetric model for three simulations where the satellite initial conditions are the same for both haloes.

In the triaxial haloes, unless the initial orbit of the satellite is a short-axis tube, the angular momentum of the satellite begins to precess about the long axis and then changes to precess about the minor axis as there are two preferred planes in a triaxial potential,

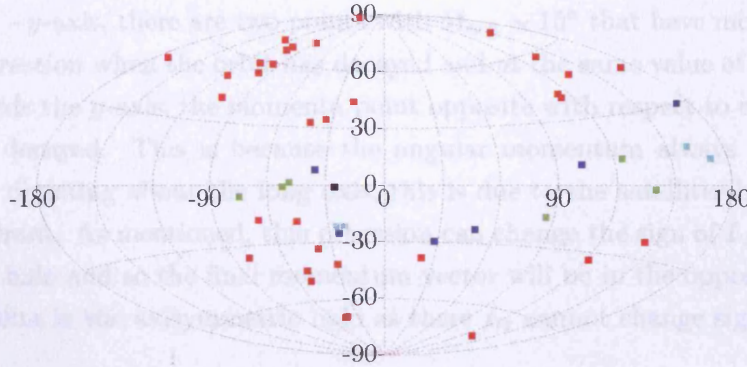


Figure 4.5: Equal-Area Aitoff projection showing the initial position of the angular momentum vector. The different colours show the difference in the evolution of the angular momentum between the triaxial model DM53 and the axisymmetric model and are shown in Table 4.1.

		Triaxial		
		z_{same}	z_{opp}	x
Axisym.	z	red	blue	cyan
	x	green		black

Table 4.1: Colour Key of Figure 4.5 denoting the final orbital plane as determined by the angular momentum vector (L) of the satellite in the axisymmetric and triaxial model. In the axisymmetric model the momentum vector of the satellite will point along the z -axis (equatorial orbit) or x -axis (polar orbit). In the triaxial model the momentum vector can point along the z -axis, either in the same or opposite direction as the final vector in the axisymmetric model, or towards the x -axis.

perpendicular to the long- and minor-axis. Due to this initial precession about the long-axis, if L_z is initially negative, it can end up precessing about the positive minor axis and vice versa. In the axisymmetric potential, the angular momentum of the satellite will only precess about the positive or negative minor axis depending on the sign of the initial L_z component. Hence, a satellite with the same initial conditions can end up precessing about opposite minor axis with respect to each other in the triaxial and axisymmetric potentials (top panels in Figure 4.4). Figure 4.5 shows the initial angular momentum vectors of the satellites from all 50 simulations on an Aitoff projection, and the different symbol colours show how the evolution of the orbital plane differs between the triaxial halo model DM53 and the axisymmetric model. It can be seen that the angular momentum vectors point in the same direction in both models (red points) when \mathbf{L} deviates from the

xy -plane ($\delta\mathbf{L}_{xy}$) initially by $\lesssim 30^\circ$. When $-30^\circ \lesssim \delta\mathbf{L}_{xy} \lesssim 30^\circ$, then the final precession can be different to each other in both models. There is an asymmetry seen, e.g. where \mathbf{L} is towards the $-y$ -axis, there are two points with $\delta\mathbf{L}_{xy} \sim 15^\circ$ that have momenta pointing in the same direction when the orbit has decayed and at the same value of $\delta\mathbf{L}_{xy}$ when L is pointing towards the y -axis, the momenta point opposite with respect to each other when the orbit has decayed. This is because the angular momentum always precesses in an anti-clockwise direction about the long axis, this is due to the satellites being launched in the same quadrant. As mentioned, this precession can change the sign of L_z of the satellite in the triaxial halo and so the final momentum vector will be in the opposite direction to the same satellite in the axisymmetric halo as there L_z cannot change sign.

4.2.2 Changing the Satellite Mass

In the real world, as the satellite is falling in to the centre of the halo, it loses mass due to tidal stripping and truncation of the satellite, which will then change the dynamical friction as Chandrasekhar's formula (and Binney's) states that the dynamical friction acceleration is proportional to satellite mass. So if the mass increases the dynamical friction force is increased, which will reduce the infall time. Binney (1977) shows that the dynamical friction is also proportional to $(1 - e_v^2)^{1/2}$, where $e_v^2 = 1 - (\sigma_\perp/\sigma_\parallel)^2$ is ellipticity of the velocity dispersion ellipsoid. Changing the mass of the satellite will mean that the satellite orbit will change and this leads to the evolution of e_v being different, even if the satellites have the same initial conditions. Figure 4.6 shows the infall time of a satellite for 4 different satellite masses. The satellites are all extended softened particles for which the softening length has either been increased, in order to keep the density of the satellite the same (green line), held fixed (black line). The points can be reproduced by a relation of the form $t_{\text{infall}} \propto M_{\text{sat}}^{-0.777}$ for the satellites with varying softening lengths and $t_{\text{infall}} \propto M_{\text{sat}}^{-0.814}$ for the satellites with the same softening lengths (Figure 4.6). The satellites have an initial tangential velocity of $e_{\text{sph}} = 0.11$ and are all started from the same initial position, in halo model DM53. The direction of the velocity was changed to see whether there was an orbital dependence of this fit, but the relation is still best fit by the one given above. There is a difference in the gradients because with the same softening lengths the heavier particles become more concentrated. This means the wake formed behind the satellite will be larger as the field bodies will be scattered more and the larger wake will increase the dynamical friction. With Chandrasekhar's formula we expect $t_{\text{infall}} \propto M_{\text{sat}}^{-1}$ (Read & Gilmore, 2003). The difference presumably is because the fundamental inaccuracies of Chandrasekhar's formula. The formula neglects any velocity anisotropies as it assumes an isotropic medium. The difference could be a difference in the non-local wake effects, however testing this is beyond the scope of this analysis.

Figure 4.7 is an Aitoff projection of the evolution of the angular momentum vector for

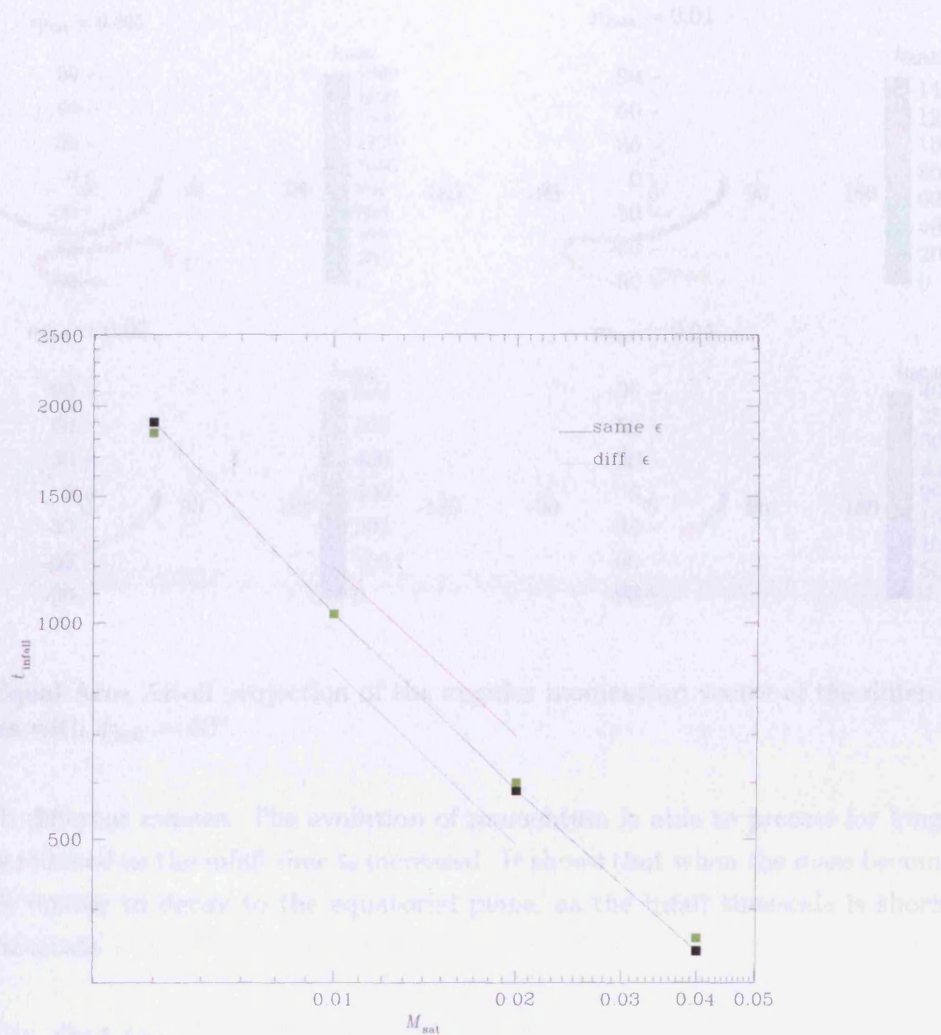


Figure 4.6: Figure showing the infall time of the satellites for different satellite masses as they orbitally decay into the triaxial halo. The green line and points are when the satellites have the varying softening length as the mass is varied to keep the density constant and the black line and points represents the satellites that has the same softening length for all masses. The red line indicates an ideal fit to the data for the varying softening length and the blue line indicated an ideal fit to the data for the constant softening length.

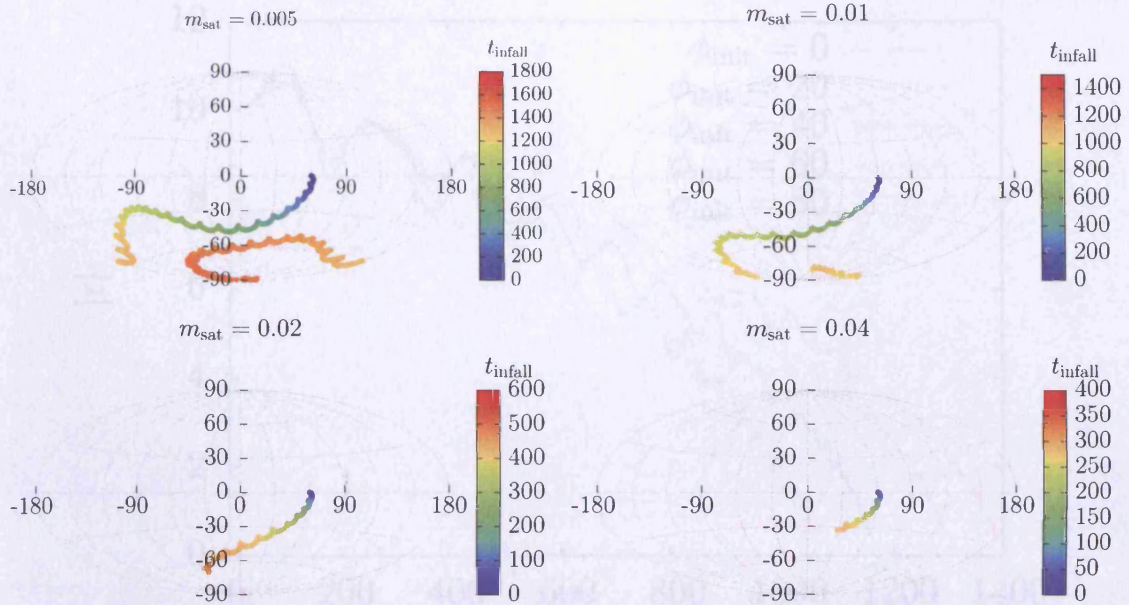


Figure 4.7: Equal-Area Aitoff projection of the angular momentum vector of the different mass satellites with $\phi_{\text{init}} = 60^\circ$.

satellites with different masses. The evolution of momentum is able to precess for longer as the mass is reduced as the infall time is increased. It shows that when the mass becomes too large it is unable to decay to the equatorial plane, as the infall timescale is shorter than that decay timescale.

4.3 Polar Orbits

As predicted by Binney (1977) and shown by Peñarrubia et al. (2004), when the satellite is on a polar orbit in an axisymmetric potential the satellite will always stay on this polar orbit. In a triaxial halo this will only be the case if the satellite orbits in the preferred plane about the long axis. It is interesting to see how the evolution of the satellite orbit behaves when it is not about the long axis in order to explore the likelihood that polar-ring galaxies might occupy triaxial dark matter haloes. As found in the previous section, orbits tend to decay to the preferred plane perpendicular to the short-axis, and so one expects the orbits to decay to this plane, which suggests that even in the most extreme case of a satellite on a polar orbit (except for the case in which it is exactly about the long axis) the orbit can potentially decay to the equatorial plane. In order to investigate this simulations were undertaken. The satellites are placed on the minor-axis of the halo at a distance $r = 10r_s = r_t$. They are given a near circular velocity with $e_{\text{sph}} = 0.11$ in the direction

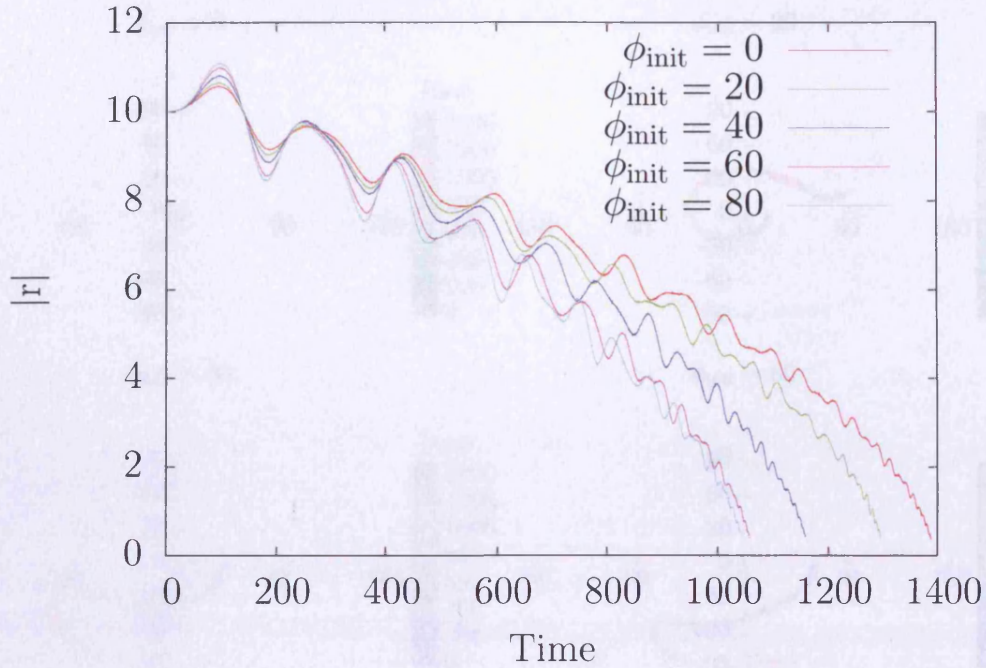


Figure 4.8: Figure showing the evolution of the satellite orbit in triaxial halo DM53 with $M_{\text{sat}} = 0.01$ for different values of ϕ_{init} (different colours).

defined by an azimuthal angle (ϕ_{init}) where $\phi_{\text{init}} = 0^\circ$ is towards the intermediate-axis (giving a stable orbit about the long-axis), and $\phi_{\text{init}} = 90^\circ$ is towards the long-axis (giving an unstable orbit about the intermediate-axis). 12 simulations were run for each halo model starting from $\phi_{\text{init}} = -10^\circ$ to $\phi_{\text{init}} = 100^\circ$ in steps of 10° . Analogous to the result found by Peñarrubia et al. (2004) where the infall time of the satellite increases as the orbit becomes more polar, the infall time of the satellite increases as ϕ_{init} is reduced peaking at $\phi_{\text{init}} = 0$ when the satellite is on an orbit about the long axis which also corresponds to the results in Chapter 3 (Figure 4.8).

In the triaxial haloes, except $\phi_{\text{init}} = 0$ and $\phi_{\text{init}} = 90$, the satellite initially precesses about the long-axis as seen in the previous section. When $\phi_{\text{init}} < 30^\circ$ the timescale to decay to the centre of the halo was faster than the timescale for the angular momentum to flip to pointing towards the minor-axis, even though the time taken to fall in to the centre was longer when ϕ_{init} was smaller. Figure 4.9 shows equal-area Aitoff projections of the angular momentum of the satellite with different values of ϕ_{init} as it evolves in the triaxial halo DM53. This shows that the closer the orbit is to the preferred plane perpendicular to the long-axis, the longer it takes to eventually change the angular momentum vector to precess about the minor-axis. The only difference between the two halo models was that in the flatter halo model, the angular momentum vector precesses about the long-axis

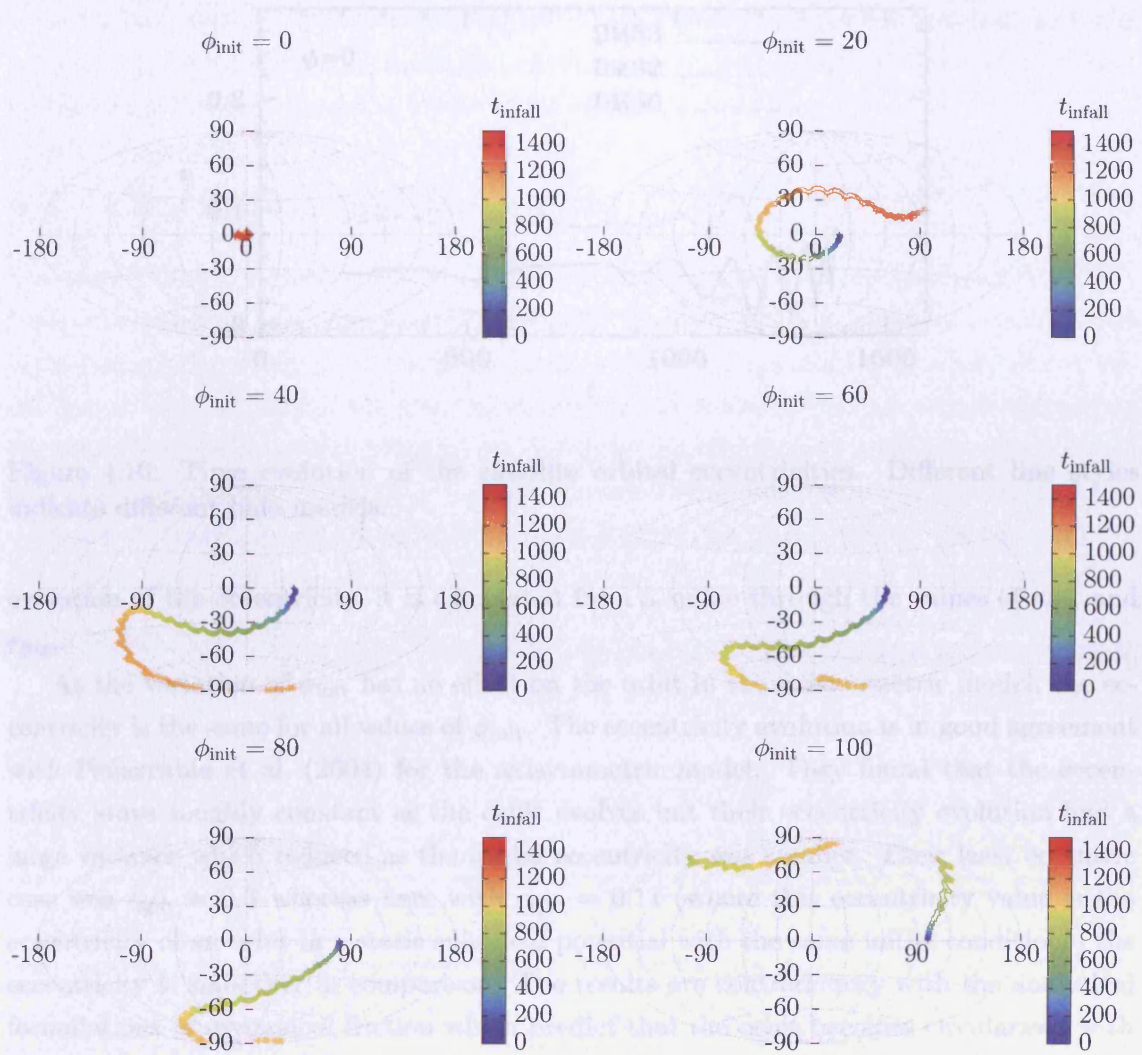


Figure 4.9: Equal-Area Aitoff projection of the angular momentum vector of the satellite for different ϕ_{init} .

faster than in the rounder halo model.

As the polar rings extend out to well beyond the visible host of the galaxy, their eccentricity is a possible probe of the shape of the dark halo. The flatter the halo potential is, the more the ring will be elongated parallel to the minor axis of the halo (Schweizer et al., 1983; Katz & Richstone, 1984). Figure 4.10 shows the evolution of the eccentricity of the orbit of the satellite in the two triaxial models and the axisymmetric models for $\phi_{\text{init}} = 0$. The eccentricity is defined as $e = (r_{\text{apo}} - r_{\text{peri}})/(r_{\text{apo}} + r_{\text{peri}})$, where r_{apo} , r_{peri} are the apocentre and pericentre, respectively. The apocentre and pericentre values are obtained by noting where the satellite's radial velocity changes sign. To obtain a smoother

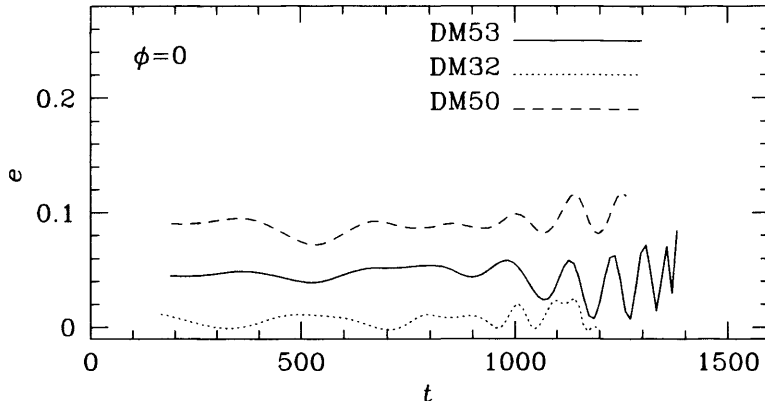


Figure 4.10: Time evolution of the satellite orbital eccentricities. Different line styles indicate different halo models.

evolution of the eccentricity, it is calculated from a spline through the values of r_{apo} and r_{peri} .

As the variation of ϕ_{init} has no effect on the orbit in the axisymmetric model, the eccentricity is the same for all values of ϕ_{init} . The eccentricity evolution is in good agreement with Peñarrubia et al. (2004) for the axisymmetric model. They found that the eccentricity stays roughly constant as the orbit evolves but their eccentricity evolution had a large variance which reduced as the initial eccentricity was smaller. Their least eccentric case was $e_{\text{sph}} = 0.3$ whereas here with $e_{\text{sph}} = 0.11$ (where this eccentricity value is the eccentricity of an orbit in a static spherical potential with the same initial conditions) the eccentricity is smoother in comparison. The results are contradictory with the analytical formulations of dynamical friction which predict that the orbit becomes circularised with the circularisation becoming stronger as the satellite moves in higher density areas. The analytical result predicts a circularisation because when the satellite is at pericenter, it feels most of the dynamical friction force at this point in the orbit. At pericentre the radial velocity is zero and in an isotropic halo the direction of the drag force is exactly in the opposite direction of motion and so the tangential velocity is reduced which leads to a circularisation of the orbit. However, as we have an anisotropic halo, the direction of dynamical friction is not exactly opposite the direction of motion which will mean that the orbit may not be circularised.

The satellite orbit in the triaxial halo shows the same characteristics in that the eccentricity of the orbit stays constant as the orbit decays. The increase in noise of the eccentricity at late times of the orbits is due to orbit becoming a box orbit and the dynamical friction force is changing the nature of the orbit more drastically as the force is much higher in the inner parts. The initial eccentricity is also dependant on ϕ_{init} as the eccentricity is greater as ϕ_{init} increases, with the eccentricity increasing roughly the

same for both triaxial halo models. The value of c/b seems to have a correlation with the eccentricity. DM50 which has the highest average eccentricity also has the smaller c/b and DM32 has c/b of 0.875 and the lowest eccentricity.

4.4 Conclusions and Discussion

The results shown in Section 4.2 could give a possible explanation on the origins of KDCs. If satellite galaxies that were orbitally decaying into the centre of elliptical galaxies were dense enough then they could reach the centre without being completely tidally disrupted. As there is no mass loss in the simulations shown here these results are a limiting case on the evolution of the orbital plane of the satellite. So simulations with the satellite as a distribution of bodies rather than a single extended body are needed. We note, however, that full N -body simulations undertaken by Peñarrubia et al. (2004) showed that for low eccentricity orbits, most of the mass is retained when the satellite reaches the centre. This is however dependent on the adopted satellite model. Both axisymmetric and triaxial haloes also provide a mechanism for the satellite to be orbiting obliquely to the halo which are also seen in observations of KDCs (NGC 3656, Balcells & Stanford (1990)). These ortho-rotating cores are much rarer.

As the orbit of the satellite decays to the equatorial plane, this provides a mechanism for feeding gas discs in elliptical galaxies. If the elliptical was devoid of gas or gas-poor, then ram-pressure stripping is not effective so a gas rich satellite may not lose all its gas before it reaches the centre and the loss of gas occurs only by tidal disruption. Kendall et al. (2003), who studied (via semi-analytic simulations) the location of gas stripped from a gas rich satellite, found that the more circular the satellite orbit is, the closer to the centre the gas is deposited. It should be noted that they used a very simplistic model of the gas stripping in which it is removed in the same way as normal stellar mass. Following from that, it is then possible that the satellite can hold enough gas to feed the central disc. As we have shown, in a triaxial or axisymmetric halo, the satellite will be on the equatorial plane when it reaches the centre and the gas deposited by this satellite will also lie on this plane due to momentum conservation. Although, ideally this needs to be tested with a full hydrodynamical treatment.

Polar ring galaxies have two components that have nearly orthogonal kinematics with the major axis of the polar ring aligned with the apparent minor axis of the host galaxy. As the origin of the polar ring is hypothesised to be a satellite galaxy and the ring is formed due to the mass loss of the satellite via tidal stripping, we performed simulations of a satellite orbit evolving in a triaxial and axisymmetric dark matter halo model. The satellite orbit gives an indication of where any polar ring will be found as the mass that is lost will trace out the orbit. If the satellite had a shallow density profile then it is

possible to completely disrupt it within a couple orbital timescales, leaving a ring of debris. Polar rings are seen to have inclinations in the polar angle from 10° to 30° which in an axisymmetric case, differential precession can lead to a warping of the ring. In an axisymmetric potential the orbital plane always precesses about the short-axis and in a triaxial potential orbits that are close to polar orbits precess about the long-axis. This difference means that the precession and consequently the warping of the ring can be more pronounced in the axisymmetric case and as this warping is not seen in the observations of polar rings. Due to the stable orbits within a triaxial halo it is possible for polar rings to exist if they are embedded in triaxial dark matter haloes.

Using polar rings as a probe to the flattening (c/a) of dark matter haloes is possible due to the eccentricities of the orbits differing in each halo models for the same initial conditions of the satellite. The flatter the halo is, the larger the eccentricity of the satellite orbit will be increased. However, it will be difficult to distinguish between a triaxial halo and a axisymmetric halo and find the three-dimensional shape of the halo (ie. b/a), as the azimuthal angle between the polar orbit and the long-axis of the halo needs to be known, as the eccentricity of the orbit is a function of this angle in the triaxial orbit and this azimuthal angle cannot be observed.

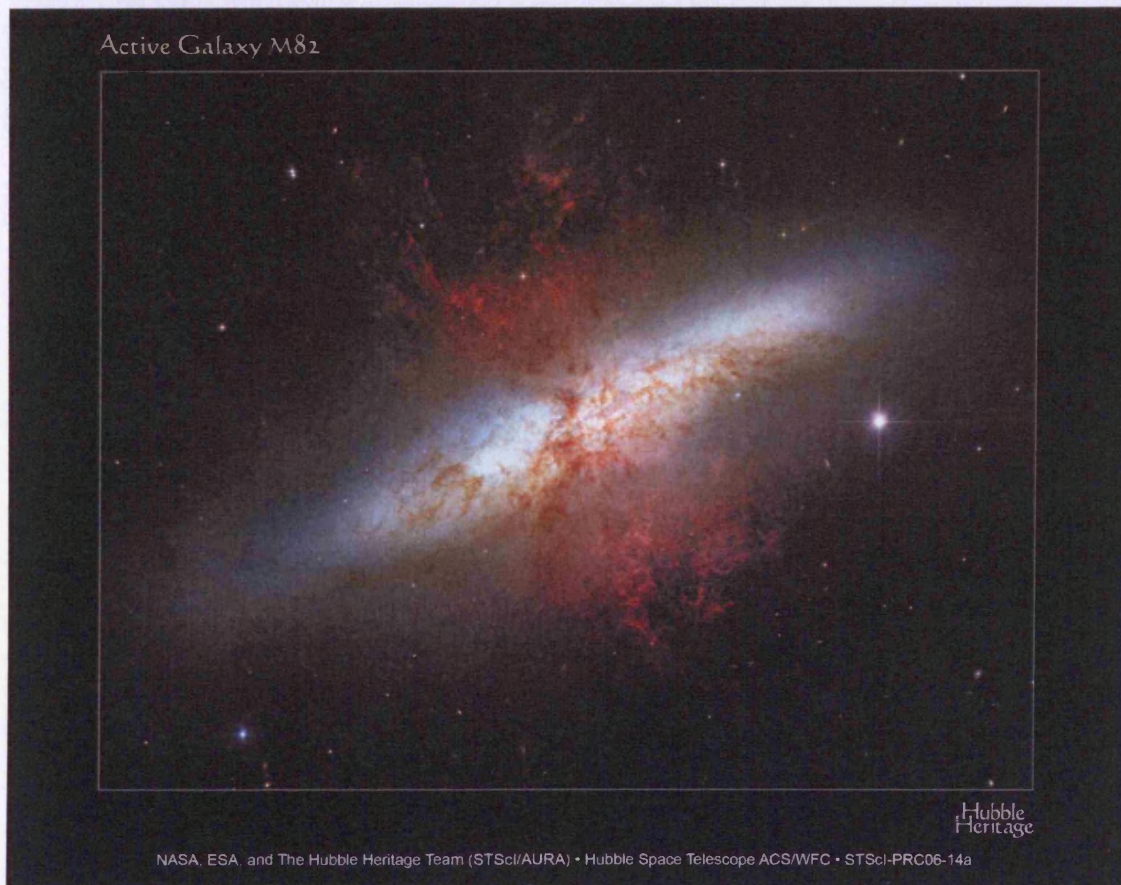
Cosmological simulations have shown the density profile of dark matter haloes is divergent at small radii, forming cusp. However, inferred observations of the dark matter profile, alongside numerous independent data show that a cored profile is needed to fit the observations. Baryonic matter is used in various simulations as a means of reducing the density profile at small radii. Other suggested means include means of transporting baryonic matter to the inner parts of a halo. The subsequent merger of the satellite galaxy has an effect on the halo shape as the satellite's orbital energy and is transferred to the host halo.

5

5.1 Introduction

Effects of Minor Mergers on Triaxial Haloes

Quinn et al. (1996) were the first to use numerical simulations to study the shape of dark matter haloes. In order to do this they used spherical coordinates and assumed the host structure. They found that there was a significant difference in the density profiles of collapsed objects and the initial distribution of matter in the universe. However, West et al.



Cosmological simulations have shown the density profile of dark matter haloes is divergent at small radii, forming a cusp. However, inferred observations of the dark matter profile, along with numerical simulations have shown that a cored profile is needed to fit the observations. Baryonic matter is used in various simulations as a means of reducing the density profile at small radii. Minor mergers are an ideal means of transporting baryonic matter to the inner parts of a halo. The consequent merger of the satellite galaxy has an effect on the halo shape as the satellite loses orbital energy and is transferred to the host halo.

5.1 Introduction

Quinn et al. (1986) were the first to use N -body simulations to study the shape of dark matter haloes in order to find how the initial conditions affected the final structure. They found that there was a connection between the density profiles of collapsed objects and the initial fluctuation spectrum for Einstein-de Sitter universes. However, West et al. (1987) found that the density profiles of simulated galaxy clusters were similar, irrespective of the initial conditions as dynamical effects like violent relaxation are efficient at erasing information of the initial conditions. Navarro et al. (1997) (hereafter, NFW) found that the spherically averaged density profiles of the N -body dark matter haloes are similar, regardless of the cosmological model. They proposed a parametric density profile that was universal for all dark matter haloes and independent of halo mass

$$\rho(r) = \frac{\rho_c}{(r/r_s)^\alpha (1 + r/r_s)^{3-\alpha}} \quad (5.1)$$

where r_s is the scale radius and ρ_c is the characteristic density.

NFW proposed that the value of the inner density slope $\alpha = 1$. The value of α has been the subject of much debate in later work. Moore et al. (1998) and Fukushige & Makino (1997) argued for $\alpha = 1.5$, while Jing & Suto (2000) and Klypin et al. (2001) found that the value of α depends on halo mass, merger history and substructure. Power et al. (2003) showed that the logarithmic slope becomes increasingly shallow at small radii with little indication of the slope reaching an asymptotic value. Although there have been many large-scale cosmological simulations, there is still no final consensus about the exact shape of the dark matter density profile. However, all simulations to date consistently predict that the density profile is divergent in the inner parts, which is referred to as a central cusp.

There have been many observational attempts to infer the density profile of dark matter haloes via gas rotation curves. The distribution of gas can be spectroscopically observed to well beyond the luminous radius allowing to probe the dark matter dominated outer regions of galaxies. Moore (1994) analysed H_I observations of a dwarf galaxy and found that the model profiles are too steep to accurately predict the rotation velocities on radial

scales $\lesssim 10\text{kpc}$. de Blok & Bosma (2002) and de Blok et al. (2003) used hybrid $\text{H}\alpha$ and HI observations of low surface brightness galaxies and tried to fit the observations using numerical simulations. They also found that cuspy haloes (with $\alpha = 1$) do not produce the correct rotation curves. They found that an inner density slope of $\alpha = 0.2$ produces the best fit to the data. Salucci (2001) and Borriello & Salucci (2001) reached the same conclusions with optical observations of spiral galaxies at the visible edge of discs where the dark matter halo is the main component of the galaxy. Gentile et al. (2004) decomposed the HI rotation curves of five spiral galaxies into their luminous and dark components and again found that the rotation curves of the dark component could only be better fitted with cored halo density profiles.

Numerical simulations have also been used to show that galaxies need a cored density profile. Kleyna et al. (2003) used N -body simulations to model the second peak of the stellar distribution which is associated with a kinematically cold subpopulation in the dwarf spheroidal Ursa Minor. They found that the harmonic potential of a cored dark matter halo prevented the clump from dissolving too quickly. In a dark matter halo with a cusped density profile the clump dissolves within less than a Gyr whereas in the cored model the clump could last for a Hubble time. N -body simulations of bars have also shown the need for low densities of dark matter in the inner haloes of spiral galaxies. Debattista & Sellwood (2000) and Athanassoula (2003) found that strong, fast bars in galaxies experience fierce braking and slow unacceptably in dense haloes, and that the existence of fast bars in strongly barred galaxies require the halo density to be low.

This discrepancy between cosmological simulations and the observational data has become known as the cusp-core problem. This is a big issue for ΛCDM cosmology as the systems which have been studied, the LSBs and dwarf galaxies, inferred from the rotation curves are the most dark matter dominated. There is either a fundamental flaw in ΛCDM cosmogony or that there are some astrophysical processes that make the cusp shallower in dark matter haloes.

There have been many attempts at using baryonic matter to reduce the log slope of density profile in the centre of dark matter haloes. Navarro et al. (1996) and Binney et al. (2001) proposed that feedback from star formation could flatten the halo profile. The idea is that gas first collects slowly in a disk at the centre of the halo which adiabatically compresses it. Once the disk grows dense enough to trigger a burst of star formation, the energy released blasts out the gas into the halo at high speed and this results in a non-adiabatic decompression of the halo, which may lead to the reduction of the dark matter density. Gnedin & Zhao (2002) simulated this idea in the most extreme case, where they grew the disc inside a halo to adiabatically compress it, and they then instantaneously removed the disc completely. They found that the density was reduced but only by a factor of two.

Zhao et al. (2002) suggest that the dark matter cusp can be reduced by the accretion of dark matter onto a supermassive black hole. This result relied on tidal stirring from infalling satellites and the loss cone refilling to more efficient than previously thought. Read & Gilmore (2003) showed that this process would not significantly alter the cusp. The black holes from the merges can eject much of the central matter via scattering and so the accretion rate is reduced.

It has also been shown that stellar bars can transfer angular momentum to dark matter particles through orbital resonances and dynamical friction (Weinberg & Katz, 2007; Sellwood, 2008). This process slows the bar but also reduces the density of the halo. Merritt et al. (2002) showed that super-massive black hole growth via mergers can also reduce the central halo profile. As the two black holes of the progenitors move towards the centre of the halo remnant due to dynamical friction, dark matter particles can be ejected from the centre via three body encounters when the two black holes have formed a bound pair.

El-Zant et al. (2001) used semi-analytic Monte Carlo simulations to see if it is possible to reduce the inner density profile through the infall of baryonic clumps. The baryonic clumps, modelled as a single particle were evolved in a static NFW halo and given a drag force using the Chandrasekhar (1943) dynamical friction formula. The baryons collect into clumps through the Jeans instability as galaxies are assembled. The baryonic clumps fall into the centre of the halo through dynamical friction and transfer energy to the halo particles and hence lower the density. It is assumed that the clumps are small enough that they do not collide with each other, that they are sufficiently tightly bound that they do not disrupt due to tidal forces, that they maintain their cohesion independent of internal physical processes like star formation and that mass clumps contain little dark matter.

Jardel & Sellwood (2009) tested the proposal of El-Zant et al. (2001) using full N -body simulations to find out the clump mass needed to significantly change the inner density profile of a dark matter halo. They modelled the heavy clump using a single particle with an extended smoothing length. The clumps were initially on circular orbits, which are not very realistic as it is highly unlikely that infalling clumps would be on circular orbits. From this they found that the heavier the particle, the more it is able to decrease the log slope of their initial dark matter halo. A clump of 5% of the halo mass was able to flatten the halo mass within a radius $r \lesssim r_s$, where r_s is the scale radius. Although, the density reduction was milder than predicted by El-Zant et al. (2001). They then split the baryonic mass into a number of heavy particles and found that for a baryonic mass of 10% of the total mass within $15r_s$ must be made up of $\lesssim 150$ equal clumps to again flatten the density profile to $r \lesssim r_s$. They found a milder density reduction than El-Zant et al. (2001) due to the difference of dynamical friction, as El-Zant et al. (2001) used the semi-analytic approach of invoking dynamical friction and used $\ln \Lambda \simeq 8.5$ (see Equation 1.3) whereas Jardel & Sellwood (2009) found that their simulation of a single clump corresponds to

$\ln \Lambda \simeq 2.5$.

Goerdt et al. (2008) consider the energy exchange between the satellite and background halo in relation to the change in halo shape. Assuming the satellite is and remains on a circular orbit, the energy transfer does not depend on the process of dynamical friction. The energy lost by the satellite moving from radius $r + \delta r$ to r is injected into a spherical shell at r . After this energy injection from the satellite, the halo must return to virial equilibrium. Assuming there is no mass loss, the kinetic energy is converted to potential energy and the halo expands resulting in a decrease in density.

The focus of this chapter will be similar to that of Jardel & Sellwood (2009). The simulations from Chapter 3 are used but the analysis is focused on the dark matter halo. The satellites that were used are equivalent to the baryonic clumps used by El-Zant et al. (2001) and Jardel & Sellwood (2009), as they were modelled as a single heavy particle with an extended softening length. The key focus in this chapter will be to explore the reduction of the cusp in the density profile in triaxial haloes as both El-Zant et al. (2001) and Jardel & Sellwood (2009) used spherical dark matter haloes. Jardel & Sellwood (2009) claimed that reason they observed a milder density reduction than El-Zant et al. (2001) was because of the differing values of $\ln \Lambda$. The differing value of $\ln \Lambda$ caused the clump in the simulations of Jardel & Sellwood (2009) to fall in slower than in the simulations of El-Zant et al. (2001) which corresponded to a reduction in the rate of energy transferred to the halo from the satellite. The evolution of the axis ratios will also be investigated because as energy is transferred from the satellite to the halo, it is interesting to see how this energy transfer affects the overall shape of the triaxial dark matter halo.

5.2 Infall Time Revisited

As shown in Chapter 3, the infall time of a satellite is dependant on the initial position. Jardel & Sellwood (2009) used $\ln \Lambda$ in the Chandrasekhar (1943) dynamical friction formula as a free parameter to match the infall time from Chandrasekhar's formula to the simulation. Using this reasoning, a range of values for $\ln \Lambda$ will be found for the satellite orbit decay in a triaxial halo as different initial positions lead to different infall times. To find the value of $\ln \Lambda$ corresponding to the simulations described in Chapter 3, a semi-analytic code is used. The satellite is placed in a static potential that is created from the triaxial halo models used in the full N -body simulation described in Section 3.2. The satellite is then given a drag force as prescribed by Chandrasekhar (1943). The assumption is also made that the halo particles have a Maxwellian velocity distribution that allows us to write the frictional drag as

$$a_{\text{df}} = -\frac{4\pi G^2 M \rho \ln \Lambda}{v^3} \left[\text{erf}(X) - \frac{2X}{\sqrt{\pi}} e^{-X^2} \right] \mathbf{v} \quad (5.2)$$

where, G is the gravitational constant, M is the mass of the satellite, $\rho(r)$ is the local density distribution, v is the velocity of the satellite, $\ln \Lambda$ is the Coulomb logarithm and $X = v/\sqrt{2}\sigma(r)$.

Matching the infall time of the satellite in the semi-analytic simulation to the full N -body simulation, the value of the scaling parameter $\ln \Lambda$ was found to range between 4.5 to 5.2, which is about halfway between the values used by El-Zant et al. (2001) and Jardel & Sellwood (2009). While using the dynamical friction formula in a semi analytic code does match the full N -body simulations reasonably well, changing the values of $\ln \Lambda$ never produces an exact fit because of the fundamental inaccuracies of Chandrasekhar's formula.

Previous work in modelling dynamical friction have yielded conflicting results with some authors finding that the Chandrasekhar (1943) dynamical friction formula reproduces fully self consistent simulations well (Velazquez & White, 1999; Jiang & Binney, 2000; Jardel & Sellwood, 2009) when $\ln \Lambda$ is used as a fitting parameter. While other work, e.g. Hashimoto et al. (2003) and Fellhauer & Lin (2007), found that they could not get a suitable fit to their full self-consistent simulations and that using $\ln \Lambda$ as a fitting parameter. Hashimoto et al. (2003) found using a temporal varying $\ln \Lambda$ the semi-analytic code fit much better to the results of a N -body simulation. They argued that the need for using $\ln \Lambda$ as a fitting parameter was unnecessary since $\ln \Lambda$ is calculated from the size of the satellite and its distance to the centre of the host galaxy.

5.3 Halo Response of Satellite Accretion

As the satellite sinks to the centre of the halo, it experiences dynamical friction and loses orbital energy. As dynamical friction can be thought of as a series of two-body encounters (Chandrasekhar, 1943), the orbital energy is transferred to the halo particles surrounding the satellite, increasing their velocity dispersion and “heating” the halo. The satellite loses most of its energy when it is at pericentre as the dynamical friction is highest here due to the higher local density of the halo. so the innermost part of the halo is heated the most. This can be seen in Figure 5.1 which shows the initial and final radial profile of the velocity dispersion (σ) and the components of velocity dispersion of all the halo models for when the satellite is on a highly eccentric orbit ($e_{\text{sph}} = 1$) and when the satellite starts on a near circular orbit ($e_{\text{sph}} = 0.04$). When the satellite has decayed to the centre the velocity dispersion profile rises in the inner parts where before the velocity dispersion decreases towards the centre. For all three halo models the velocity dispersion is similar to the original profile at $r > r_s$. Inside this radius, it deviates from the original profile for both initial eccentricities shown in Figure 5.1. The radius that the original profiles peaked is an analytical value (see Dehnen & McLaughlin (2005)) $r_{\sigma\text{peak}} = (7/9)^{9/4}r_s \approx 0.568r_s$.

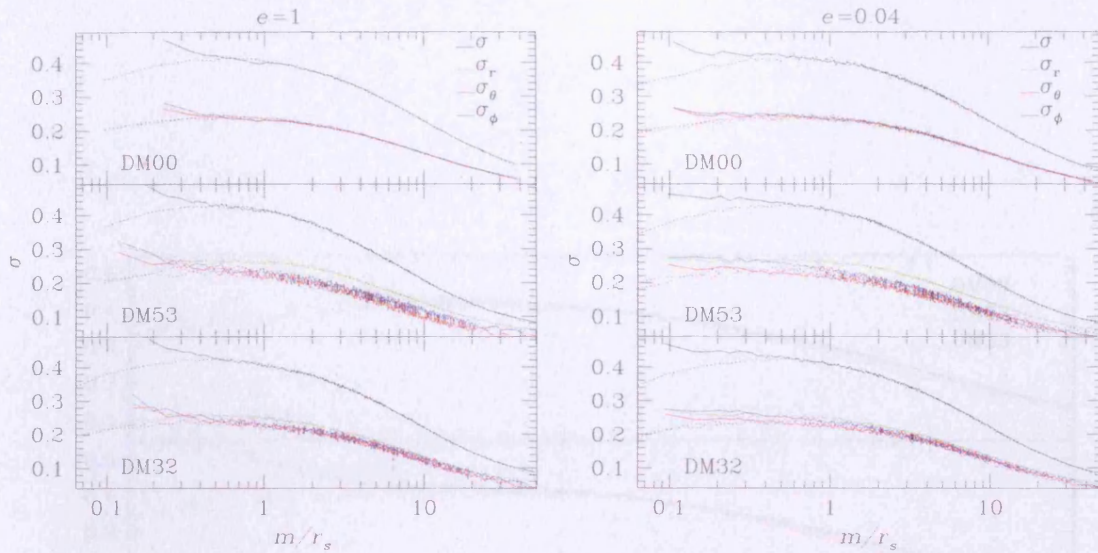


Figure 5.1: Initial (dashed lines) and final (solid lines) radial profiles of the velocity dispersion component for the three halo models. The left figure shows the halo profile when the satellite is on a radial orbit ($e_{\text{sph}} = 1$) and the right figure shows the halo profile when the satellite is on a near circular orbit ($e_{\text{sph}} = 0.04$).

It is this point where the final profile deviates from the original profile.

This anisotropy in the velocity dispersion as reflected in the β (Equation 3.4) profile has been seen in triaxial equilibria when they have been created using different methods from our own (Merritt, 1980; Moore et al., 2004). Looking at the β profile of the halo after the evolution of the satellite, for both e_{sph} shown the halo becomes isotropic in the triaxial haloes, and become increasingly radially anisotropic, which DM53 increasing more than DM32.

Figure 5.2 shows the velocity dispersion of all the halo models before and after the satellite has decayed to the centre of the halo.

The halo from which the profiles are calculated are taken from simulations in which in all three models the satellites infall time was similar. The gradient of the slope of the velocity distribution in the inner part of the halo at $r \lesssim 0.6r_s$ is shallower when the initial orbit of the satellite is less eccentric. This is due to the manner in which the satellite loses energy as it decays to the centre of the halo as described by Goerdt et al. (2008). When the satellite is on a near circular orbit ($e_{\text{sph}} = 0.04$) at large radii the energy loss is spread over a shell at radius r . The energy per unit mass gained by the shell is small at large radii as the volume of the shell is larger, so there is less an effect on the halo at large radii from the energy transfer of the satellite. The satellite does spend more time at large radii so it therefore loses more energy at large radii and does not lose as much energy in the inner

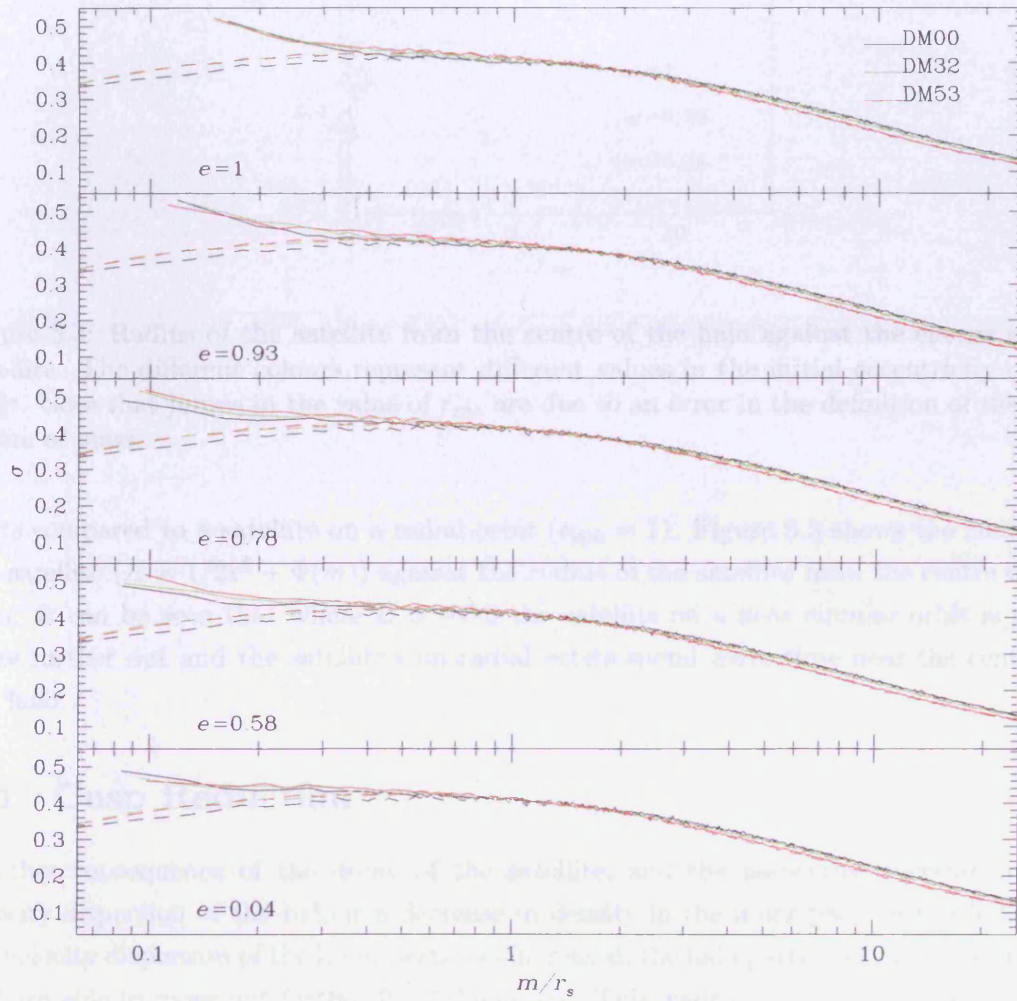


Figure 5.2: Initial (dashed lines) and final (solid lines) radial profiles of the velocity dispersion for the spherical and the two triaxial models for orbits of varying e_{sph} .

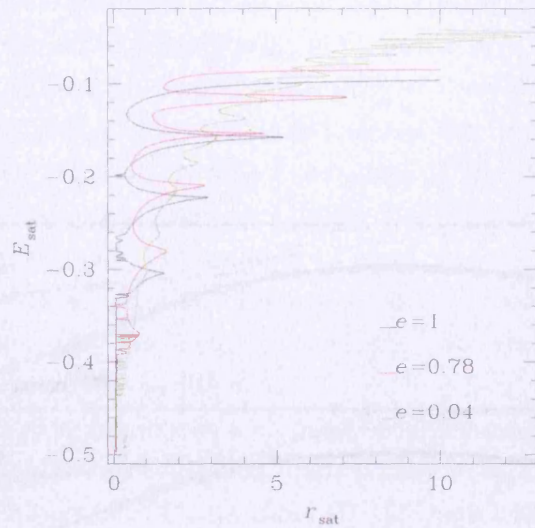


Figure 5.3: Radius of the satellite from the centre of the halo against the energy of the satellite. The different colours represent different values in the initial eccentricity of the orbit. Note that jumps in the value of r_{sat} are due to an error in the definition of the halo centre of mass.

parts compared to a satellite on a radial orbit ($e_{\text{sph}} = 1$). Figure 5.3 shows the energy of the satellite ($E = 1/2v^2 + \Phi(m)$) against the radius of the satellite from the centre of the halo. It can be seen that where $E > -0.3$ the satellite on a near circular orbit is much more further out and the satellite's on radial orbits spend more time near the centre of the halo.

5.4 Cusp Reduction

Another consequence of the decay of the satellite, and the associated increase in the velocity dispersion of the halo is a decrease in density in the inner parts of the halo. As the velocity dispersion of the inner parts has increased, the halo particles have more energy and are able to move out further from the centre. This leads to a reduction in density in the inner parts of the halo. Figure 5.4 shows the density profiles of all the halo models before and after the satellite has fallen into the centre of the halo. The density profiles in the inner parts of the halo have clearly become shallower. The dotted lines show the approximate gradient of the density profile at small radii ($r < 0.2r_s$) and are calculated from an extrapolation of the density values of the two innermost bins. For the initial models, $\rho \propto m^{-1.6}$ at small radii. The approximate gradients, α where $\rho \propto m^{-\alpha}$. The gradient of the density profile is reduced as the initial eccentricity of the satellite orbit is increased. For initial eccentricities of 0.04 and 0.58, $\rho \propto m^{-1.2}$. $\rho \propto m^{-1}$ when the

initial eccentricities are 0.78 and 0.93. The shallowest density gradient at small radii was when the satellite was on a radial orbit ($e_{\text{sat}} = 1$), here $\rho \propto m^{-0.85}$. The peak of all the density profiles shown in Figure 5.4, occur when $\frac{m}{r_s} = 2$ and it is from within this radius ($r_2 = (11/10)^{1/3} r_s \approx 0.6376 r_s$) where the final models differ from the original models.

In our simulations there is an increased reduction of the density profile as a consequence of the satellite being modelled as a single heavy particle. In the real world the satellite would be tidally disrupted and the mass distributed by this process and have but this is not the case here. The density profiles are internally consistent and can be compared to the results of other studies.

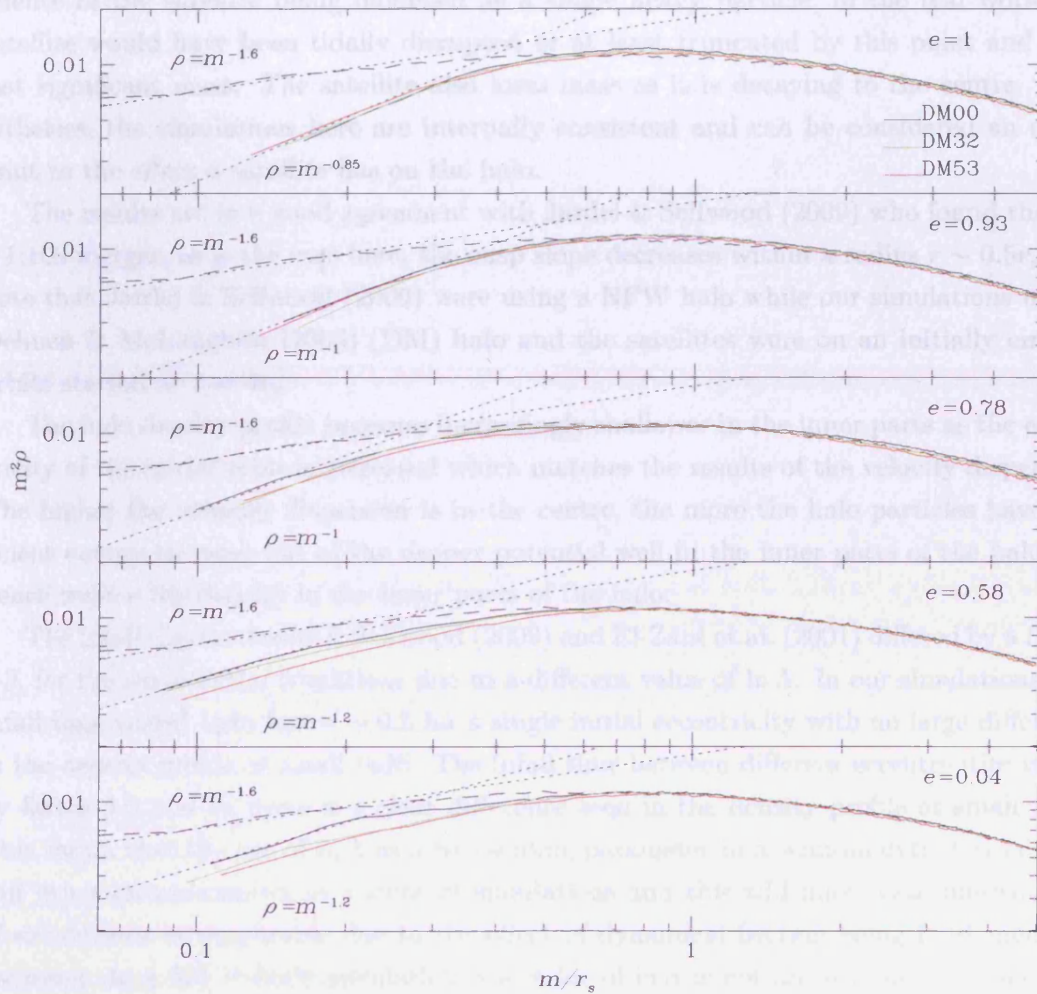


Figure 5.4: Initial (dashed lines) and final (solid lines) density profiles for the spherical and the two triaxial models. Different line colours represent different initial halo models. The dotted lines show the gradient derived from the first two bins of the constructed density profile using density bins.

initial eccentricities are 0.78 and 0.93. The shallowest density gradient at small radii was when the satellite was on a radial orbit ($e_{\text{sph}} = 1$), here $\rho \propto m^{-0.85}$. The peak of all the density profiles shown in Figure 5.4, occur when $\frac{d \ln \rho}{d \ln m} = 2$ and it is from within this radius ($r_2 = (11/13)^{9/4} r_s \approx 0.6876 r_s$) where the final models differ from the original models.

In our simulations there is an increased reduction of the density profile as a consequence of the satellite being modelled as a single heavy particle, in the real world the satellite would have been tidally disrupted or at least truncated by this point and have lost significant mass. The satellite also loses mass as it is decaying to the centre. Nevertheless, the simulations here are internally consistent and can be considered an upper limit to the effect a satellite has on the halo.

The results are in a good agreement with Jardel & Sellwood (2009) who found that for a 1:100 merger, as is the case here, the cusp slope decreases within a radius $r \sim 0.5 r_s$. We note that Jardel & Sellwood (2009) were using a NFW halo while our simulations used a Dehnen & McLaughlin (2005) (DM) halo and the satellites were on an initially circular orbits started at $r = 4 r_s$.

The halo density profile becomes increasingly shallower in the inner parts as the eccentricity of the initial orbit is increased which matches the results of the velocity dispersion. The higher the velocity dispersion is in the centre, the more the halo particles have sufficient energy to move out of the deeper potential well in the inner parts of the halo and hence reduce the density in the inner parts of the halo.

The infall time in Jardel & Sellwood (2009) and El-Zant et al. (2001) differed by a factor 2-3, for the same initial conditions due to a different value of $\ln \Lambda$. In our simulations, the infall time varied upto factor ~ 0.5 for a single initial eccentricity with no large difference in the density profile at small radii. The infall time between different eccentricities varied by factor 2-4 and so there is a clear difference seen in the density profile at small radii. This shows that the use of $\ln \Lambda$ as a free scaling parameter in a semi-analytic formulation will bring inconsistencies in a suite of simulations and this will make two different sets of simulations incomparable due to the effect of dynamical friction being fundamentally incorrect. In a full N -body simulation, the value of $\ln \Lambda$ is not an issue as the dynamical friction is due to the physics of the system rather than an added prescription. In trying to match the simulations of the spherical halo to the Chandrasekhar formula provided a range of values for $\ln \Lambda$ depending on the initial conditions, which begins to show how inaccurate the Chandrasekhar formula can become when it is used in only a semi-analytic manner like in El-Zant et al. (2001).

Figure 5.5 shows the density of the final halo models within different masses of the total mass against the ratio of infall time of the satellite in the triaxial halo over the infall time in the spherical halo for all of the simulations undertaken. It shows that the density upto 2% of the mass of the halo is similar across all three halo models. As the infall time

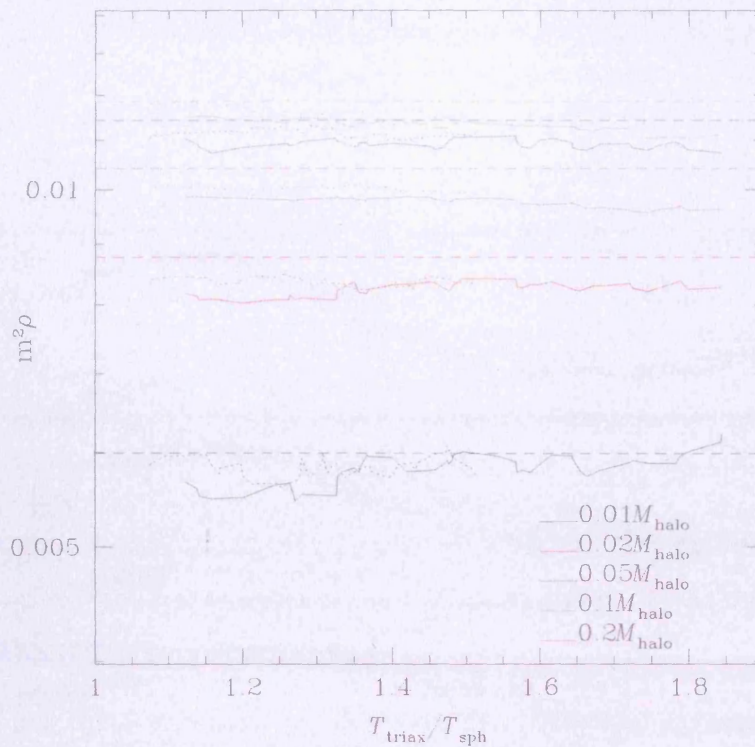


Figure 5.5: Density of halo within 1%, 2%, 5%, 10% and 20% (different colours) of the total mass of the halo after the satellite has orbitally decayed to the centre against the ratio of infall time of the satellite in the triaxial halo over the infall time in the spherical halo. The dashed lines are of halo model DM00, dotted lines are of halo model DM32 and solid lines are of halo model DM53.

of the satellite increases then the density increases in the inner parts and reduces in the outer parts of the halo. This is due to where the mass is being moved to by the satellite as it falls in.

5.4.1 Mass Excavation

Looking at the net difference in the mass profile allows us to see where about the mass has been moved to by the satellite. Figure 5.6 shows the radial profile of the mass reduction within r between the initial and final haloes for all halo models and for all initial eccentricities, where $\Delta M = M_{\text{initial}} - M_{\text{final}}$. In all cases, the satellite excavated mass from the inner parts of the halo as it settles into the centre which corresponds with the density reduction in the inner parts as shown in the previous section. The amount of mass excavated by the satellite is of order of its own mass and the initial velocity determines the radius to which the mass is excavated. When the satellite is on a highly eccentric orbit the mass excavated is greatest as it spends more time in the outer parts of the halo ($r < 1r_s$), so

energy is lost here and these parts of the halo are heated and the mass is moved out as the halo expands. The low eccentricity orbits lead to a reduced mass excavation in the outer parts with a strong peak in the inner parts because the energy is expelled here and the inner parts are heated up the most. This follows the results of the reduction of the cusp from the previous section.

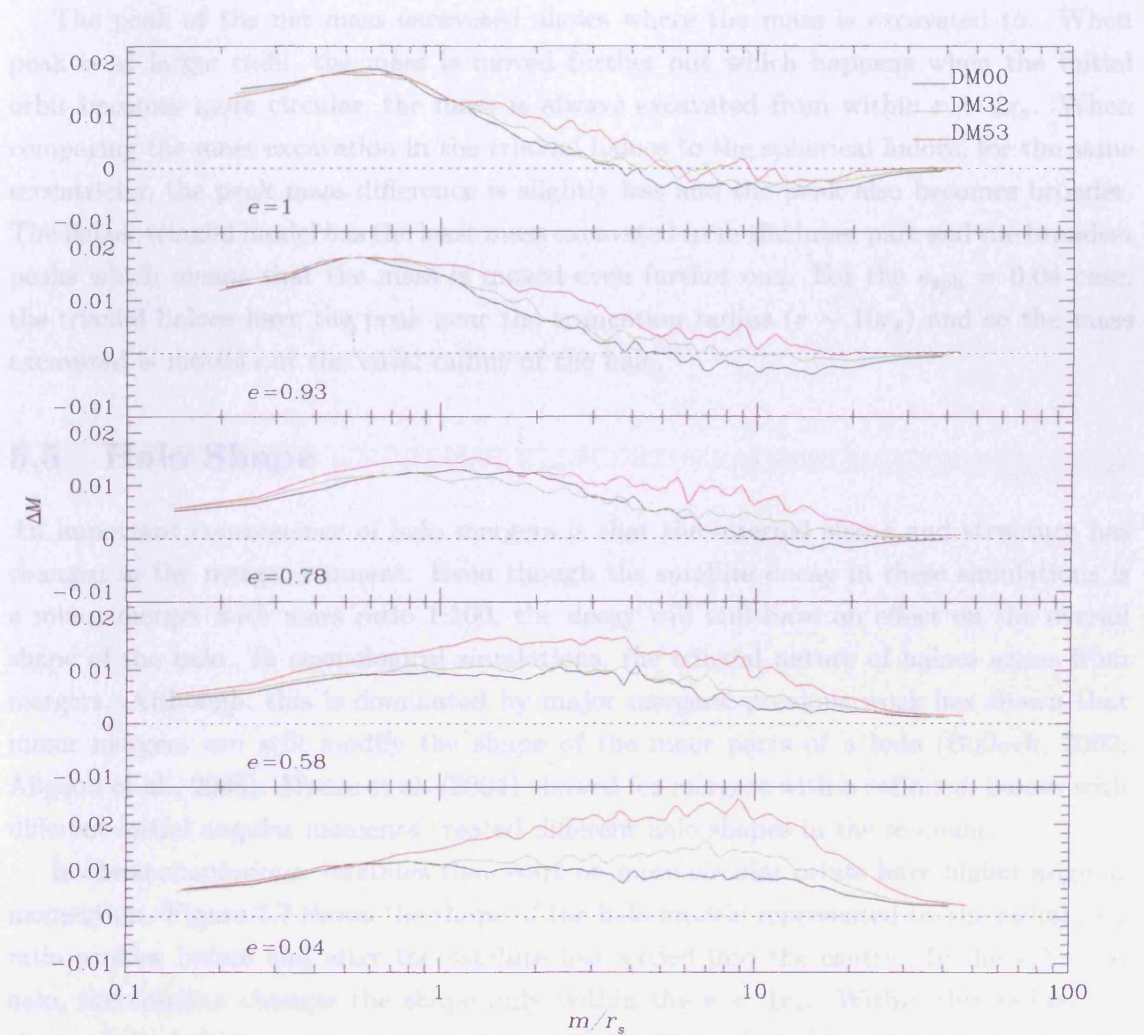


Figure 5.6: Reduction of mass contained within a triaxial radius m between the initial halo and final halo once the satellite has decayed to the centre. Different colours represent different initial halo models.

energy is lost here and these parts of the halo are heated and the mass is moved out as the halo expands. The less eccentric orbits lead to a reduced mass excavation in the outer parts with a strong peak in the inner parts because the energy is expelled here and the inner parts are heated up the most. This follows the results of the reduction of the cusp from the previous section.

The peak of the net mass excavated shows where the mass is excavated to. When peak is at larger radii, the mass is moved further out which happens when the initial orbit becomes more circular, the mass is always excavated from within $r = 1r_s$. When comparing the mass excavation in the triaxial haloes to the spherical haloes, for the same eccentricity, the peak mass difference is slightly less and the peak also becomes broader. The flatter triaxial model has the least mass excavated from the inner part and the broadest peaks which means that the mass is moved even further out. For the $e_{\text{sph}} = 0.04$ case, the triaxial haloes have the peak near the truncation radius ($r \sim 10r_s$) and so the mass excavated is moved out the virial radius of the halo.

5.5 Halo Shape

An important consequence of halo mergers is that the internal shape and structure has changed in the merger remnant. Even though the satellite decay in these simulations is a minor merger with mass ratio 1:100, the decay will still have an effect on the overall shape of the halo. In cosmological simulations, the triaxial nature of haloes arises from mergers. Although, this is dominated by major mergers, previous work has shown that minor mergers can still modify the shape of the inner parts of a halo (Bullock, 2002; Allgood et al., 2006). Moore et al. (2004) showed for mergers with a ratio 1:3, haloes with different initial angular momenta created different halo shapes in the remnant.

In these simulations, satellites that start on more circular orbits have higher angular momentum. Figure 5.7 shows the shape of the halo models represented by the radial axis ratio profiles before and after the satellite has settled into the centre. In the spherical halo, the satellite changes the shape only within the $r < 1r_s$. Within this radius the shape of the halo becomes axisymmetric, with the flattening of the inner parts, seen as the reduction of the c/a axis ratio, becoming increasingly high towards the centre. Here, the initial direction of the satellite is important to the direction of the axisymmetry, the direction of the major axis of the axisymmetric part is in the same direction as the satellite is travelling. So the satellite induces a preferred axis in the spherical halo. For the model DM53, which is the flatter of the two triaxial halo models, the outer part with exception of $e_{\text{sph}} = 0.04$, the profile is the same as the initial profile at $r > 10r_s$, ie. where the satellite starts from. When $e_{\text{sph}} = 0.04$, the satellite starts near pericentre in its orbit. It therefore affects the outer parts of the halo and so the shape of the halo at $r > 10r_s$ is changed here

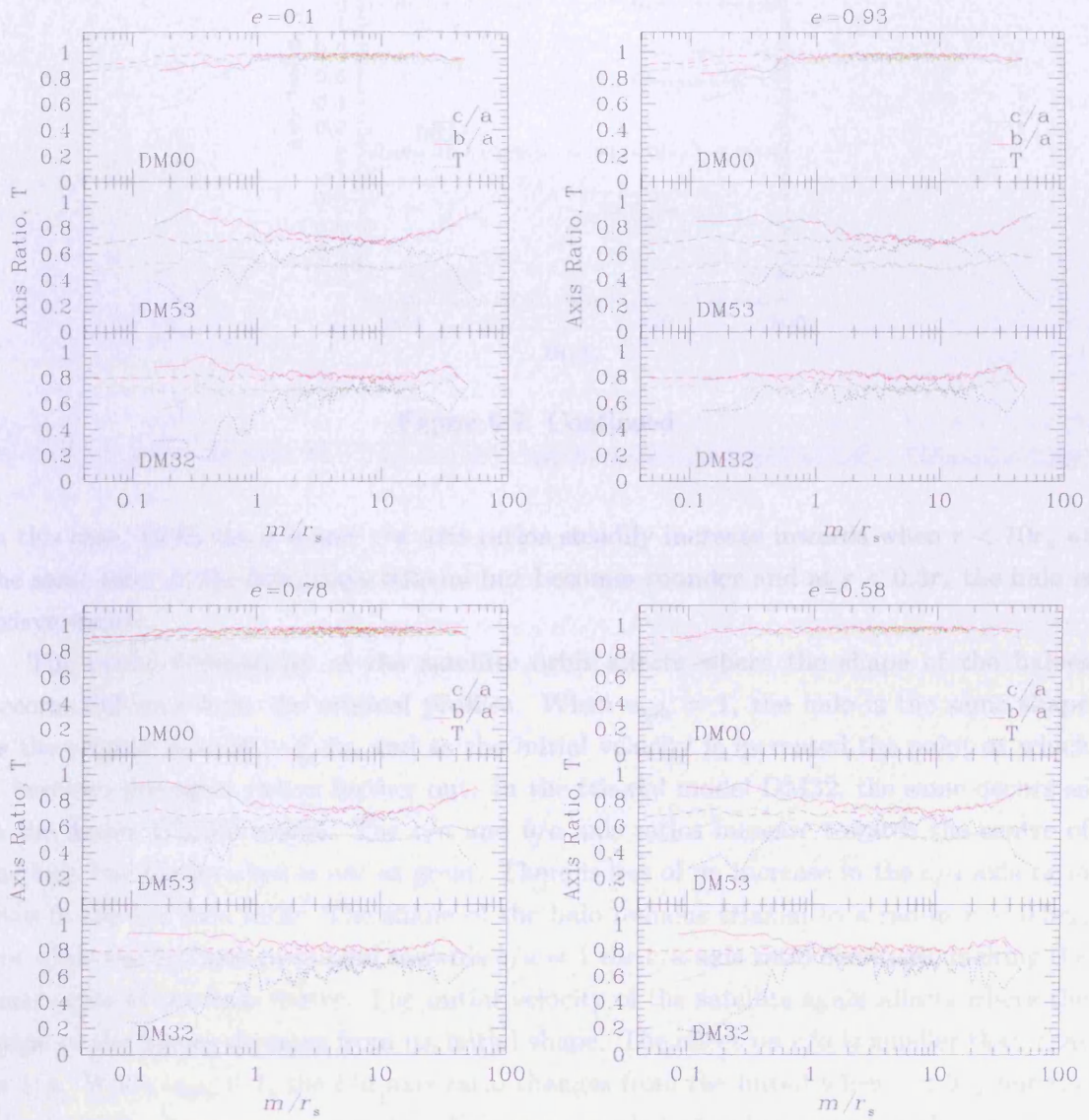


Figure 5.7: Initial (dashed lines) and final (solid lines) minor to major (c/a , green lines) and intermediate to major (b/a , red lines) axis ratios and triaxiality of the final models (dotted lines) for all halo models.

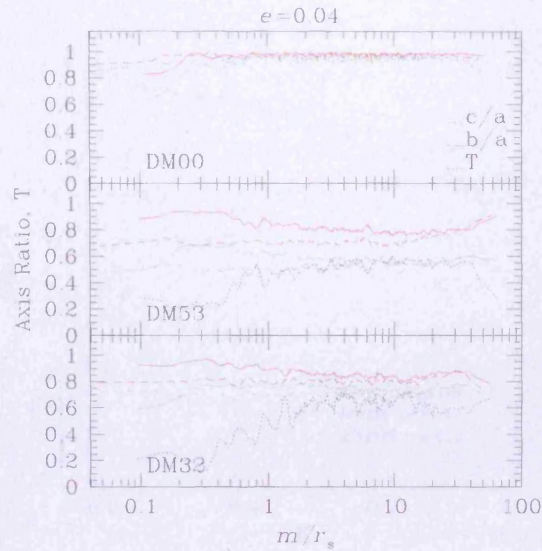


Figure 5.7: Continued

in this case. Both the b/a and c/a axis ratios steadily increase inwards when $r < 10r_s$ at the same rate, so the halo stays triaxial but becomes rounder and at $r < 0.3r_s$ the halo is axisymmetric.

The initial eccentricity of the satellite orbit affects where the shape of the haloes become different from the original profiles. When $e_{\text{sph}} = 1$, the halo is the same shape as the original outside $r \gtrsim 3r_s$ and as the initial velocity is increased the point at which it becomes divergent moves further out. In the triaxial model DM32, the same occurs as in the flatter triaxial model. The c/a and b/a axis ratios increase towards the centre of the halo but the increase is not as great. There is less of an increase in the c/a axis ratio than in the b/a axis ratio. The shape of the halo remains triaxial to a radius $r \sim 0.5r_s$, but while the b/a axis ratio tend towards $b/a = 1$ the c/a axis ratio decreases, making the inner parts of the halo flatter. The initial velocity of the satellite again affects where the shape of the haloes diverges from its initial shape. The effect on c/a is smaller than that on b/a . When $e_{\text{sph}} = 1$, the b/a axis ratio changes from the initial when $r < 3r_s$ but the c/a axis ratio changes when $r < 1r_s$. This suggests that rounder triaxial models are more stable. The action of the decaying satellite changes the shape of the flatter triaxial halo more drastically than the rounder triaxial model. Figure 5.7 shows that the triaxiality (see Section 1.4) of the halo is similar to the original in to $r = 2r_s$ even though the axis ratios are increasing, but in the inner parts ($r < r_s$) the triaxiality parameter tends to 0, again showing that the shape of the halo is an oblate spheroid at small radii.

There are two dominating factors to the change in shape of the halo. The first is the transfer of energy by the satellite as it loses orbital energy, which changes the orbits of

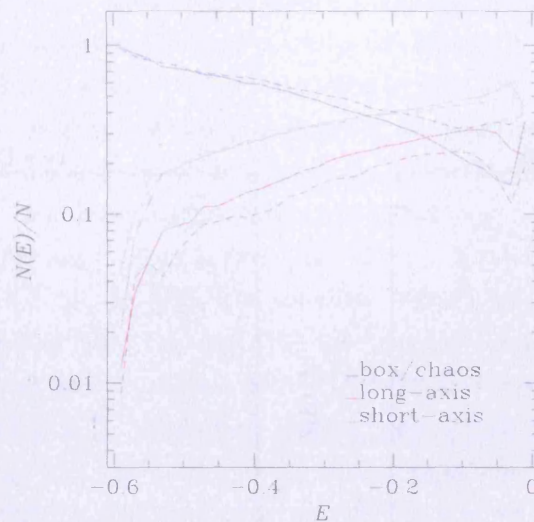


Figure 5.8: Histogram of the energies of all the halo bodies in both the triaxial models DM53 (dashed line) and DM32 (solid line). Different colours represent the different orbital families that a body can be classified to in a triaxial potential.

the halo particles are they can move onto a different orbit with the increase in energy. The second is the change in the underlying potential due to the presence of the satellite. Which again will affect the orbits of the satellite as the phase-space structure is changed.

5.5.1 Resultant Orbital Structure

As the shape of the halo has been changed by the decayed satellite, the orbital structure within the halo will be affected as the triaxial structure is dependant on box orbits (Schwarzschild, 1979; Gerhard & Binney, 1985). Figure 5.8 shows the breakdown of all the halo bodies classified by orbit type and binned by energy and gives an indication of the orbital structure of the modelled haloes. The flatter of the two haloes has more box orbits at nearly all energies, with a lot more at lower energies, where the rounder triaxial halo has many more of the halo particles on both classes of tube orbit. This shows how the box orbits provide the backbone of the triaxial halo structure especially if the halo is fairly flat as elongated box orbits enhance the density along the longest and intermediate axes. These elongated box orbits are vital in this model and the difference in the box orbits at high energies is most likely the highly elongated box orbits. Figure 5.9 shows the energies of the halo bodies of the initial energy distribution and after the satellite has decayed to the centre. When the satellite is on an eccentric orbit the most of the energy is lost in the inner parts of the halo. Figure 5.9 shows there is a large drop of halo bodies on box orbits with $E < -0.4$ as they have gained energy as box orbits are centrophillic and are most halo particles at small radii are on box orbits.. The number of halo bodies on box

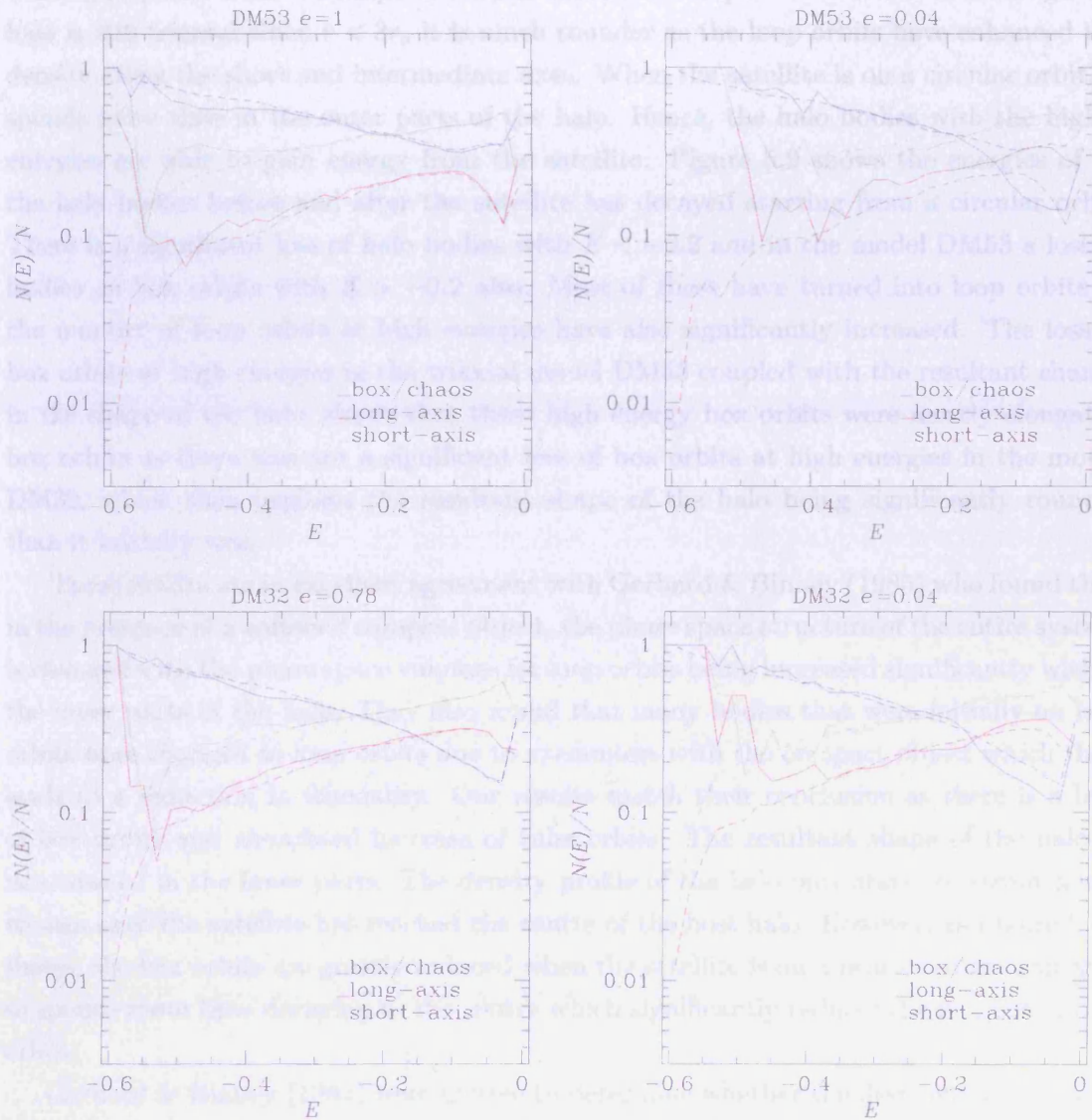


Figure 5.9: Histogram of the energy of the halo bodies initially (dashed lines) and after the satellite has decayed to the centre (solid lines). Different colours represent the different orbital families that a body can be in a triaxial potential. The top panels are of the flatter halo model DM53 and the bottom panels are of the rounder triaxial model DM32.

orbits have been reduced the most and as there is a reduction of box orbits in nearly all energy bins. Figure 5.10 shows the contribution to the density profile due to different orbit families. This shows that the halo bodies that were on box orbits are now on loop orbits. This corresponds with the shape of the halo shown in the previous section as although the halo is still triaxial when $r < 3r_s$ it is much rounder as the loop orbits have enhanced the density along the short and intermediate axes. When the satellite is on a circular orbit, it spends more time in the outer parts of the halo. Hence, the halo bodies with the higher energies are able to gain energy from the satellite. Figure 5.9 shows the energies of all the halo bodies before and after the satellite has decayed starting from a circular orbit. There is a significant loss of halo bodies with $E < -0.2$ and in the model DM53 a loss of bodies on box orbits with $E > -0.2$ also. Most of these have turned into loop orbits as the number of loop orbits at high energies have also significantly increased. The loss of box orbits at high energies in the triaxial model DM53 coupled with the resultant change in the shape of the halo, shows that these high energy box orbits were mostly elongated box orbits as there was not a significant loss of box orbits at high energies in the model DM32, which then explains the resultant shape of the halo being significantly rounder than it initially was.

These results are in excellent agreement with Gerhard & Binney (1985) who found that in the presence of a softened compact object, the phase space structure of the entire system is changed with the phase space volumes for loop orbits being increased significantly within the inner parts of the halo. They also found that many bodies that were initially on box orbits were changed to loop orbits due to encounters with the compact object which then leads to a reduction in triaxiality. Our results match their conclusion as there is a loss of box orbits and associated increase of tube orbits. The resultant shape of the halo is non-triaxial in the inner parts. The density profile of the halo only starts to significantly change once the satellite has reached the centre of the host halo. However, as Figure 5.10 shows, the box orbits are greatly reduced when the satellite is on a near circular orbit and so spends more time decaying to the centre which significantly reduces the number of box orbits.

Gerhard & Binney (1985) were unable to determine whether the destruction of triaxiality occurs abruptly or at a steady rate due to the need for a full N -body simulation to determine this. The disruption of the smaller box orbits will change the potential from triaxial to axisymmetric which in turn does not support box orbits and they immediately convert to tube orbits. However the disruption time is a rapidly increasing function of r and so as the smaller box orbits are disrupted much earlier the larger box orbits, axisymmetry will spread gradually from the centre. Merritt & Quinlan (1998) studied the effect of a massive central singularity on the structure of a triaxial galaxy. They found that when $M_{\text{bh}}/M_{\text{halo}} \lesssim 0.3$, the halo evolves to an axisymmetric shape on a timescale that

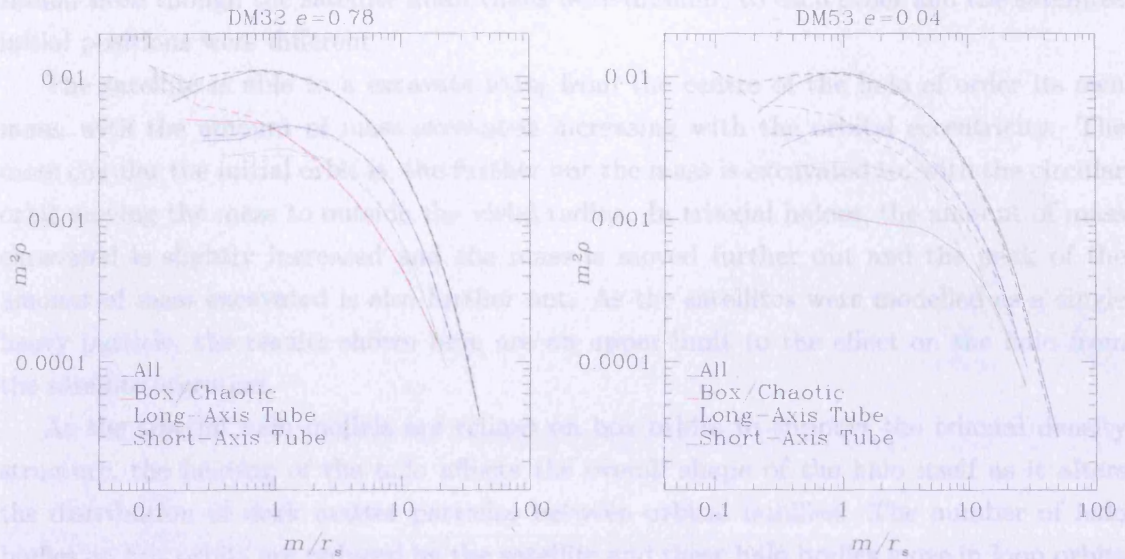


Figure 5.10: Density profile of the halo model for the rounder triaxial halo (left panel) and flatter triaxial halo (right panel) before (dashed lines) and after (solid lines) the orbit decay of the satellite. The initial eccentricity of the orbit of the satellite was $e_{\text{sph}} = 0.78$, $e_{\text{sph}} = 0.04$ for the left, right panel, respectively. The different colours indicate the contribution to the density profile due to different orbit families.

exceeds the galaxy lifetime. From our haloes it is clear that it is the latter mechanism which reduces the triaxiality at a steady rate that occurs. Even though the central region is axisymmetric there are still box orbits within the halo.

5.6 Conclusions and Discussion

Infalling satellite galaxies or massive baryonic clumps greatly affect the haloes of the host galaxies. The orbital energy that is released from the satellite galaxy as its orbits decays and slows due to dynamical friction is transferred to the host halo. This energy heats the inner parts of the halo increasing the central velocity dispersion profile and leads to a density reduction in agreement with previous work (El-Zant et al., 2001; Jardel & Sellwood, 2009).

The manner in which the satellite decays to the centre has a great effect in the amount by which the slope of the profile is reduced. Satellites on eccentric orbits reduce the density profile more than circular orbits, as the satellites are able to the centre faster as they experience more dynamical friction and so hence lose more energy in the inner parts of the halo. The difference between halo models made little difference to the resultant halo profile after the satellite had decayed to the centre, as the density profiles were very

similar even though the satellite infall times were different to each other and the satellites initial positions were different.

The satellite is able to excavate mass from the centre of the halo of order its own mass, with the amount of mass excavated increasing with the orbital eccentricity. The more circular the initial orbit is, the further out the mass is excavated to, with the circular orbit moving the mass to outside the virial radius. In triaxial haloes, the amount of mass excavated is slightly increased and the mass is moved further out and the peak of the amount of mass excavated is also further out. As the satellites were modelled as a single heavy particle, the results shown here are an upper limit to the effect on the halo from the satellite accretion.

As the triaxial halo models are reliant on box orbits to support the triaxial density structure, the heating of the halo affects the overall shape of the halo itself as it alters the distribution of dark matter particles between orbital families. The number of halo bodies on box orbits are reduced by the satellite and these halo bodies move in loop orbits creating a rounder halo. This effect was also seen in previous work by Gerhard & Binney (1985) and Merritt & Quinlan (1998).

This suggests that dark matter haloes may not have a temporally constant structural shape, which might explain the difficulties and inconsistencies in the analysis of the Sagittarius tidal stream in trying to constrain the halo shape seen in the literature. The infall of baryons, from the previous satellite accretion history of the Milky Way (Bullock & Johnston, 2005) will have changed the shape of the halo and so ideally models with time-varying halo shapes would be more realistic when trying to constrain the shape of the halo when using observational data. However, this would not be feasible as the parameter space is large and it could be possible to reproduce observable data with many different halo models, so it would be hard to constrain data.

A

Deriving the Relaxation Time

Considering the interaction between two stars, a subject star and a field star, both of mass m , shown in Figure A.1, allows us to derive the relaxation time of a gravitational system of which the two masses belong to. The system has a typical radius R , a total mass M , and is made up of N number of stars. The subject star passes within a distance b (also known as the impact parameter) to the field star, which imparts an impulse and changes the velocity of the subject star by δv . Assuming the subject star passes the field star on a straight-line trajectory, so $x = vt$, this change in velocity can be approximated by considering the perpendicular force on the subject star F_{\perp} , which is given by

$$F_{\perp} = \frac{Gm^2}{r^2} \cos(\theta) \simeq \frac{Gm^2}{b^2} \left[1 + \left(\frac{vt}{b} \right)^2 \right]^{-3/2}. \quad (\text{A.1})$$

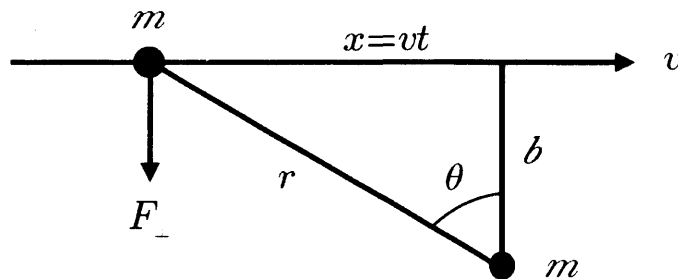


Figure A.1: Schematic of a single interaction between a subject star and a field star

By using Newton's laws $\mathbf{F} = m\dot{\mathbf{v}}$, the change in perpendicular velocity of the subject star is then

$$\delta v_{\perp} \simeq \int_{-\infty}^{\infty} \frac{Gm}{b^2} \left[1 + \left(\frac{vt}{b} \right)^2 \right]^{-3/2} dt = \frac{2Gm}{bv}. \quad (\text{A.2})$$

The above approximation is valid for when $\delta v_{\perp} \ll v$.

As the above was for a single encounter, we now consider the subject star travelling across the system once, then the number of other field stars it will encounter is

$$\delta n = \frac{N}{\pi R^2} 2\pi b db = \frac{2N}{R^2} b db \quad (\text{A.3})$$

with the impact parameter ranging between b and $b+db$. The perturbations in perpendicular velocity direction are randomly orientated so the mean change in velocity will be zero, the mean-square change is non-zero, so after one crossing, the change in perpendicular velocity is given by

$$\Delta v_{\perp}^2 \equiv \int_{b_{\min}}^{b_{\max}} \sum \delta v^2 \simeq \int_{b_{\min}}^{b_{\max}} \delta v^2 \delta n = \int_{b_{\min}}^{b_{\max}} \left(\frac{2Gm}{bv} \right)^2 \frac{2N}{R^2} b db \quad (\text{A.4})$$

where b_{\max} and b_{\min} are the maximum and minimum impact parameters, respectively. Integrating Equation A.4 over all impact parameters gives

$$\Delta v^2 \simeq 8N \left(\frac{Gm}{Rv} \right)^2 \ln \Lambda. \quad (\text{A.5})$$

where the factor

$$\ln \Lambda \equiv \ln \left(\frac{b_{\max}}{b_{\min}} \right) \quad (\text{A.6})$$

is known as the Coulomb logarithm.

We take the typical velocity of a field star to be approximately the circular velocity of a star at the radius of the system, so that

$$v^2 \approx \frac{GNm}{R}. \quad (\text{A.7})$$

We set b_{\max} to the radius of the system R , and set b_{\min} to the impact parameter needed to deflect the field star by 90 degrees $b_{90} \equiv 2Gm/v^2$. So using Equation A.7 we can say that $\Lambda \approx N$

The number of crossing required for the subject star to be deflected in the perpendicular direction by a velocity of the order of its original velocity and so deflecting the field star by 45 degrees, which is the definition of relaxation time, will be when

$$n_{\text{relax}} = \frac{v^2}{\Delta v^2} \simeq \frac{N}{8 \ln \Lambda} \simeq \frac{0.1N}{\ln N} \quad (\text{A.8})$$

Bibliography

- S. J. Aarseth. *Dynamical evolution of clusters of galaxies, I* 1963, MNRAS, 126, 223.
- S. J. Aarseth & J. Binney. *On the relaxation of galaxies and clusters from aspherical initial conditions* 1978, MNRAS, 185, 227.
- M. G. Abadi, J. F. Navarro, M. Steinmetz, & V. R. Eke. *Simulations of Galaxy Formation in a Λ Cold Dark Matter Universe. II. The Fine Structure of Simulated Galactic Disks* 2003, ApJ, 597, 21.
- A.-a.-R. Al Sufi. *Book of Fixed Stars* 964. Isfahan, Persia.
- C. Alcock, R. A. Allsman, D. R. Alves, T. S. Axelrod, A. C. Becker, D. P. Bennett, K. H. Cook, N. Dalal, et al. *MACHO Project Limits on Black Hole Dark Matter in the 1-30 M_{solar} Range* 2001, ApJ, 550, L169.
- B. Allgood, R. A. Flores, J. R. Primack, A. V. Kravtsov, R. H. Wechsler, A. Faltenbacher, & J. S. Bullock. *The shape of dark matter haloes: dependence on mass, redshift, radius and formation* 2006, MNRAS, 367, 1781.
- E. Athanassoula. *What determines the strength and the slowdown rate of bars?* 2003, MNRAS, 341, 1179.
- E. Athanassoula & A. Bosma. *Shells and rings around galaxies* 1985, ARA&A, 23, 147.
- J. Bailin & M. Steinmetz. *Internal and External Alignment of the Shapes and Angular Momenta of Λ CDM Halos* 2005, ApJ, 627, 647.
- M. Balcells. *Peculiar Kinematics* 1992, In G. Longo, M. Capaccioli, & G. Busarello, eds., *Morphological and Physical Classification of Galaxies*, vol. 178 of *Astrophysics and Space Science Library*, 221 (1992).
- M. Balcells & P. J. Quinn. *The formation of counterrotating cores in elliptical galaxies* 1990, ApJ, 361, 381.
- M. Balcells & S. A. Stanford. *A counterrotating core in the merger remnant candidate NGC 3656 (ARP 155)* 1990, ApJ, 362, 443.
- J. Barnes & P. Hut. *A hierarchical $O(N \log N)$ force-calculation algorithm* 1986, Nature, 324, 446.

-
- J. E. Barnes & L. Hernquist. *Dynamics of interacting galaxies* 1992, ARA&A, 30, 705.
- J. E. Barnes & L. Hernquist. *Transformations of Galaxies. II. Gasdynamics in Merging Disk Galaxies* 1996, ApJ, 471, 115.
- K. Bekki & M. Chiba. *Formation of the Galactic Stellar Halo. I. Structure and Kinematics* 2001, ApJ, 558, 666.
- V. Belokurov, D. B. Zucker, N. W. Evans, G. Gilmore, S. Vidrih, D. M. Bramich, H. J. Newberg, R. F. G. Wyse, et al. *The Field of Streams: Sagittarius and Its Siblings* 2006, ApJ, 642, L137.
- R. Bender. *Rotating and counter-rotating cores in elliptical galaxies* 1988, A&A, 202, L5.
- F. Bertola & M. Capaccioli. *Dynamics of early type galaxies. I - The rotation curve of the elliptical galaxy NGC 4697* 1975, ApJ, 200, 439.
- B. Binggeli, A. Sandage, & G. A. Tammann. *Studies of the Virgo Cluster. II - A catalog of 2096 galaxies in the Virgo Cluster area.* 1985, AJ, 90, 1681.
- J. Binney. *Is the flattening of elliptical galaxies necessarily due to rotation* 1976, MNRAS, 177, 19.
- J. Binney. *Dynamical friction in aspherical clusters* 1977, MNRAS, 181, 735.
- J. Binney. *On the rotation of elliptical galaxies* 1978, MNRAS, 183, 501.
- J. Binney, O. Gerhard, & J. Silk. *The dark matter problem in disc galaxies* 2001, MNRAS, 321, 471.
- P. Bode, J. P. Ostriker, & N. Turok. *Halo Formation in Warm Dark Matter Models* 2001, ApJ, 556, 93.
- A. Borriello & P. Salucci. *The dark matter distribution in disc galaxies* 2001, MNRAS, 323, 285.
- A. Bosma. *The distribution and kinematics of neutral hydrogen in spiral galaxies of various morphological types* 1978, Ph.D. thesis, Groningen Univ.).
- J. S. Bullock. *Shapes of dark matter halos* 2002, In P. Natarajan, ed., *The Shapes of Galaxies and their Dark*, 109 (2002).
- J. S. Bullock & K. V. Johnston. *Tracing Galaxy Formation with Stellar Halos. I. Methods* 2005, ApJ, 635, 931.
- J. S. Bullock, A. V. Kravtsov, & D. H. Weinberg. *Reionization and the Abundance of Galactic Satellites* 2000, ApJ, 539, 517.
-

-
- D. A. Buote, T. E. Jeltema, C. R. Canizares, & G. P. Garmire. *Chandra Evidence of a Flattened, Triaxial Dark Matter Halo in the Elliptical Galaxy NGC 720* 2002, ApJ, 577, 183.
- S. Chandrasekhar. *Dynamical Friction. I. General Considerations: the Coefficient of Dynamical Friction.* 1943, ApJ, 97, 255.
- R. J. E. Clausius. *On a Mechanical Theorem Applicable to Heat* 1870, Philosophical Magazine, 40, 122.
- D. Clowe, M. Bradač, A. H. Gonzalez, M. Markevitch, S. W. Randall, C. Jones, & D. Zaritsky. *A Direct Empirical Proof of the Existence of Dark Matter* 2006, ApJ, 648, L109.
- P. Colín, V. Avila-Reese, & O. Valenzuela. *Substructure and Halo Density Profiles in a Warm Dark Matter Cosmology* 2000, ApJ, 542, 622.
- M. Colless, G. Dalton, S. Maddox, W. Sutherland, P. Norberg, S. Cole, J. Bland-Hawthorn, T. Bridges, et al. *The 2dF Galaxy Redshift Survey: spectra and redshifts* 2001, MNRAS, 328, 1039.
- A. L. Cox & L. S. Sparke. *Using HI in Polar-Ring Galaxies to Probe Galactic Potentials* 1996, In E. D. Skillman, ed., *The Minnesota Lectures on Extragalactic Neutral Hydrogen*, vol. 106 of *Astronomical Society of the Pacific Conference Series*, 168–+ (1996).
- M. Davis, G. Efstathiou, C. S. Frenk, & S. D. M. White. *The evolution of large-scale structure in a universe dominated by cold dark matter* 1985, ApJ, 292, 371.
- W. J. G. de Blok & A. Bosma. *High-resolution rotation curves of low surface brightness galaxies* 2002, A&A, 385, 816.
- W. J. G. de Blok, A. Bosma, & S. McGaugh. *Simulating observations of dark matter dominated galaxies: towards the optimal halo profile* 2003, MNRAS, 340, 657.
- F. de Lorenzi, V. P. Debattista, O. Gerhard, & N. Sambhus. *NMAGIC: a fast parallel implementation of a χ^2 -made-to-measure algorithm for modelling observational data* 2007, MNRAS, 376, 71.
- T. de Zeeuw. *Elliptical galaxies with separable potentials* 1985, MNRAS, 216, 273.
- T. de Zeeuw & D. Merritt. *Stellar orbits in a triaxial galaxy. I - Orbits in the plane of rotation* 1983, ApJ, 267, 571.
- V. P. Debattista, B. Moore, T. Quinn, S. Kazantzidis, R. Maas, L. Mayer, J. Read, & J. Stadel. *The Causes of Halo Shape Changes Induced by Cooling Baryons: Disks versus Substructures* 2008, ApJ, 681, 1076.
-

-
- V. P. Debattista & J. A. Sellwood. *Constraints from Dynamical Friction on the Dark Matter Content of Barred Galaxies* 2000, ApJ, 543, 704.
- W. Dehnen. *The Distribution of Nearby Stars in Velocity Space Inferred from HIPPARCOS Data* 1998, AJ, 115, 2384.
- W. Dehnen. *A Very Fast and Momentum-conserving Tree Code* 2000, ApJ, 536, L39.
- W. Dehnen. *Towards optimal softening in three-dimensional N-body codes - I. Minimizing the force error* 2001, MNRAS, 324, 273.
- W. Dehnen. *A Hierarchical $O(N)$ Force Calculation Algorithm* 2002, Journal of Computational Physics, 179, 27.
- W. Dehnen. *Tailoring triaxial N-body models via a novel made-to-measure method* 2009, MNRAS, 395, 1079.
- W. Dehnen & D. E. McLaughlin. *Dynamical insight into dark matter haloes* 2005, MNRAS, 363, 1057.
- A. Dekel & J. Silk. *The origin of dwarf galaxies, cold dark matter, and biased galaxy formation* 1986, ApJ, 303, 39.
- J. Dubinski. *The Origin of the Brightest Cluster Galaxies* 1998, ApJ, 502, 141.
- J. Dubinski & R. G. Carlberg. *The structure of cold dark matter halos* 1991, ApJ, 378, 496.
- J. Dunkley, E. Komatsu, M. R. Nolta, D. N. Spergel, D. Larson, G. Hinshaw, L. Page, C. L. Bennett, et al. *Five-Year Wilkinson Microwave Anisotropy Probe Observations: Likelihoods and Parameters from the WMAP Data* 2009, ApJS, 180, 306.
- G. Efstathiou, R. S. Ellis, & D. Carter. *Further observations of the elliptical galaxy NGC 5813* 1982, MNRAS, 201, 975.
- A. Einstein. *Kosmologische Betrachtungen zur allgemeinen Relativitätstheorie* 1917, Sitzungsberichte der Königlich Preußischen Akademie der Wissenschaften,, 142–152.
- A. El-Zant, I. Shlosman, & Y. Hoffman. *Dark Halos: The Flattening of the Density Cusp by Dynamical Friction* 2001, ApJ, 560, 636.
- E. Emsellem, M. Cappellari, R. F. Peletier, R. M. McDermid, R. Bacon, M. Bureau, Y. Copin, R. L. Davies, et al. *The SAURON project - III. Integral-field absorption-line kinematics of 48 elliptical and lenticular galaxies* 2004, MNRAS, 352, 721.

-
- A. E. Evrard, T. J. MacFarland, H. M. P. Couchman, J. M. Colberg, N. Yoshida, S. D. M. White, A. Jenkins, C. S. Frenk, et al. *Galaxy Clusters in Hubble Volume Simulations: Cosmological Constraints from Sky Survey Populations* 2002, ApJ, 573, 7.
- M. Fellhauer, V. Belokurov, N. W. Evans, M. I. Wilkinson, D. B. Zucker, G. Gilmore, M. J. Irwin, D. M. Bramich, et al. *The Origin of the Bifurcation in the Sagittarius Stream* 2006, ApJ, 651, 167.
- M. Fellhauer & D. N. C. Lin. *The influence of mass-loss from a star cluster on its dynamical friction - I. Clusters without internal evolution* 2007, MNRAS, 375, 604.
- R. A. Flores & J. R. Primack. *Observational and theoretical constraints on singular dark matter halos* 1994, ApJ, 427, L1.
- M. Franx, G. Illingworth, & T. de Zeeuw. *The ordered nature of elliptical galaxies - Implications for their intrinsic angular momenta and shapes* 1991, ApJ, 383, 112.
- M. Franx & G. D. Illingworth. *A counterrotating core in IC 1459* 1988, ApJ, 327, L55.
- C. S. Frenk, S. D. M. White, M. Davis, & G. Efstathiou. *The formation of dark halos in a universe dominated by cold dark matter* 1988, ApJ, 327, 507.
- T. Fukushige & J. Makino. *On the Origin of Cusps in Dark Matter Halos* 1997, ApJ, 477, L9+.
- E. Fulton & J. E. Barnes. *Core Density Profile Survival in Dissipationless Mergers* 2001, Ap&SS, 276, 851.
- G. Galilei. *Sidereus Nuncius, (Starry Messenger)* 1610. in translation: University of Chicago Press (1989).
- S. Gelato, D. F. Chernoff, & I. Wasserman. *An Adaptive Hierarchical Particle-Mesh Code with Isolated Boundary Conditions* 1997, ApJ, 480, 115.
- G. Gentile, P. Salucci, U. Klein, D. Vergani, & P. Kalberla. *The cored distribution of dark matter in spiral galaxies* 2004, MNRAS, 351, 903.
- O. E. Gerhard. *N-body simulations of disc-halo galaxies - Isolated systems, tidal interactions and merging* 1981, MNRAS, 197, 179.
- O. E. Gerhard & J. Binney. *Triaxial galaxies containing massive black holes or central density cusps* 1985, MNRAS, 216, 467.
- O. Y. Gnedin & H. Zhao. *Maximum feedback and dark matter profiles of dwarf galaxies* 2002, MNRAS, 333, 299.

-
- T. Goerdt, J. I. Read, B. Moore, & J. Stadel. *Core creation in galaxies and haloes via sinking massive objects: application to binary nuclei* 2008, ArXiv e-prints.
- J. Goodman & M. Schwarzschild. *Semistochastic orbits in a triaxial potential* 1981, ApJ, 245, 1087.
- L. Greengard & V. Rokhlin. *A fast algorithm for particle simulations* 1987, Journal of Computational Physics, 73, 325.
- V. A. Hagen-Torn, I. I. Popov, & V. A. Iakovleva. *Photometric study of the peculiar galaxy NGC 2685* 1983, Astrofizika, 19, 599.
- Y. Hashimoto, Y. Funato, & J. Makino. *To Circularize or Not To Circularize?-Orbital Evolution of Satellite Galaxies* 2003, ApJ, 582, 196.
- A. Helmi. *Is the dark halo of our Galaxy spherical?* 2004a, MNRAS, 351, 643.
- A. Helmi. *Velocity Trends in the Debris of Sagittarius and the Shape of the Dark Matter Halo of Our Galaxy* 2004b, ApJ, 610, L97.
- A. Helmi, J. F. Navarro, B. Nordström, J. Holmberg, M. G. Abadi, & M. Steinmetz. *Pieces of the puzzle: ancient substructure in the Galactic disc* 2006, MNRAS, 365, 1309.
- L. Hernquist. *An analytical model for spherical galaxies and bulges* 1990, ApJ, 356, 359.
- L. Hernquist & J. E. Barnes. *Origin of kinematic subsystems in elliptical galaxies* 1991, Nature, 354, 210.
- L. Hernquist & J. P. Ostriker. *A self-consistent field method for galactic dynamics* 1992, ApJ, 386, 375.
- G. Hinshaw, J. L. Weiland, R. S. Hill, N. Odegard, D. Larson, C. L. Bennett, J. Dunkley, B. Gold, et al. *Five-Year Wilkinson Microwave Anisotropy Probe Observations: Data Processing, Sky Maps, and Basic Results* 2009, ApJS, 180, 225.
- R. W. Hockney & J. W. Eastwood. *Computer Simulation Using Particles* 1981.
- K. Holley-Bockelmann, J. C. Mihos, S. Sigurdsson, & L. Hernquist. *Models of Cuspy Triaxial Galaxies* 2001, ApJ, 549, 862.
- E. Holmberg. *On the Clustering Tendencies among the Nebulae. II. a Study of Encounters Between Laboratory Models of Stellar Systems by a New Integration Procedure.* 1941, ApJ, 94, 385.
- E. Hubble. *A Relation between Distance and Radial Velocity among Extra-Galactic Nebulae* 1929a, Proceedings of the National Academy of Science, 15, 168.
-

-
- E. Hubble. *A spiral nebula as a stellar system, Messier 31*. 1929b, ApJ, 69, 103.
- R. Ibata, G. F. Lewis, M. Irwin, E. Totten, & T. Quinn. *Great Circle Tidal Streams: Evidence for a Nearly Spherical Massive Dark Halo around the Milky Way* 2001, ApJ, 551, 294.
- R. A. Ibata, G. Gilmore, & M. J. Irwin. *A dwarf satellite galaxy in Sagittarius* 1994, Nature, 370, 194.
- G. Illingworth. *Rotation in 13 elliptical galaxies* 1977, ApJ, 218, L43.
- C. G. J. Jacobi. *ber ein leichtes Verfahren, die in der Theorie der Skularstrungen vorkommenden Gleichungen numerisch aufzulösen* 1846, Crelle's Journal, 30, 51.
- J. R. Jardel & J. A. Sellwood. *Halo Density Reduction by Baryonic Settling?* 2009, ApJ, 691, 1300.
- I.-G. Jiang & J. Binney. *The orbit and mass of the Sagittarius dwarf galaxy* 2000, MNRAS, 314, 468.
- Y. P. Jing & Y. Suto. *The Density Profiles of the Dark Matter Halo Are Not Universal* 2000, ApJ, 529, L69.
- Y. P. Jing & Y. Suto. *Triaxial Modeling of Halo Density Profiles with High-Resolution N-Body Simulations* 2002, ApJ, 574, 538.
- K. V. Johnston, D. R. Law, & S. R. Majewski. *A Two Micron All Sky Survey View of the Sagittarius Dwarf Galaxy. III. Constraints on the Flattening of the Galactic Halo* 2005, ApJ, 619, 800.
- A. J. Kalnajs. *Polarization Clouds and Dynamical Friction* 1972, In *IAU Colloq. 10: Gravitational N-Body Problem*, vol. 31 of *Astrophysics and Space Science Library*, 13–+ (1972).
- I. Kant. *Allgemeine Naturgeschichte und Theorie des Himmels* 1755.
- N. Katz & D. O. Richstone. *Orbital characteristics of polar rings of galaxies* 1984, AJ, 89, 975.
- S. Kazantzidis, A. V. Kravtsov, A. R. Zentner, B. Allgood, D. Nagai, & B. Moore. *The Effect of Gas Cooling on the Shapes of Dark Matter Halos* 2004, ApJ, 611, L73.
- P. Kendall, J. Magorrian, & J. E. Pringle. *Active galactic nuclei and the minor merger hypothesis* 2003, MNRAS, 346, 1078.

-
- S. Khochfar & A. Burkert. *On the origin of isophotal shapes in elliptical galaxies* 2005, MNRAS, 359, 1379.
- J. T. Kleyana, M. I. Wilkinson, G. Gilmore, & N. W. Evans. *A Dynamical Fossil in the Ursa Minor Dwarf Spheroidal Galaxy* 2003, ApJ, 588, L21.
- A. Klypin, A. V. Kravtsov, J. S. Bullock, & J. R. Primack. *Resolving the Structure of Cold Dark Matter Halos* 2001, ApJ, 554, 903.
- A. Klypin, A. V. Kravtsov, O. Valenzuela, & F. Prada. *Where Are the Missing Galactic Satellites?* 1999, ApJ, 522, 82.
- J. Kormendy. *Recognizing merger remnants among normal elliptical galaxies NGC 5813* 1984, ApJ, 287, 577.
- A. V. Kravtsov, O. Y. Gnedin, & A. A. Klypin. *The Tumultuous Lives of Galactic Dwarfs and the Missing Satellites Problem* 2004, ApJ, 609, 482.
- D. R. Law, K. V. Johnston, & S. R. Majewski. *A Two Micron All-Sky Survey View of the Sagittarius Dwarf Galaxy. IV. Modeling the Sagittarius Tidal Tails* 2005, ApJ, 619, 807.
- D. R. Law, S. R. Majewski, & K. V. Johnston. *Evidence for a Triaxial Milky Way Dark Matter Halo from the Sagittarius Stellar Tidal Stream* 2009, ApJ, 703, L67.
- L. B. Lucy. *An iterative technique for the rectification of observed distributions* 1974, AJ, 79, 745.
- J. Makino. *Treecode with a Special-Purpose Processor* 1991, PASJ, 43, 621.
- L. S. Marochnik. *A Test Star in a Stellar System.* 1968, Soviet Astronomy, 11, 873.
- N. F. Martin, R. A. Ibata, M. Bellazzini, M. J. Irwin, G. F. Lewis, & W. Dehnen. *A dwarf galaxy remnant in Canis Major: the fossil of an in-plane accretion on to the Milky Way* 2004, MNRAS, 348, 12.
- M. L. Mateo. *Dwarf Galaxies of the Local Group* 1998, ARA&A, 36, 435.
- L. Mayer, F. Governato, M. Colpi, B. Moore, T. Quinn, J. Wadsley, J. Stadel, & G. Lake. *The Metamorphosis of Tidally Stirred Dwarf Galaxies* 2001a, ApJ, 559, 754.
- L. Mayer, F. Governato, M. Colpi, B. Moore, T. Quinn, J. Wadsley, J. Stadel, & G. Lake. *Tidal Stirring and the Origin of Dwarf Spheroidals in the Local Group* 2001b, ApJ, 547, L123.
-

-
- D. Merritt. *A numerical model for a triaxial stellar system in dynamical equilibrium. II - Some dynamical features of the model* 1980, *ApJS*, 43, 435.
- D. Merritt, M. Milosavljević, L. Verde, & R. Jimenez. *Dark Matter Spikes and Annihilation Radiation from the Galactic Center* 2002, *Physical Review Letters*, 88, 191301.
- D. Merritt & G. D. Quinlan. *Dynamical Evolution of Elliptical Galaxies with Central Singularities* 1998, *ApJ*, 498, 625.
- J. C. Mihos, I. R. Walker, L. Hernquist, C. Mendes de Oliveira, & M. Bolte. *A Merger Origin for X Structures in S0 Galaxies* 1995, *ApJ*, 447, L87+.
- B. Moore. *Evidence against dissipation-less dark matter from observations of galaxy haloes* 1994, *Nature*, 370, 629.
- B. Moore, C. Calcáneo-Roldán, J. Stadel, T. Quinn, G. Lake, S. Ghigna, & F. Governato. *Dark matter in Draco and the Local Group: Implications for direct detection experiments* 2001, *Phys. Rev. D*, 64, 063508.
- B. Moore, J. Diemand, P. Madau, M. Zemp, & J. Stadel. *Globular clusters, satellite galaxies and stellar haloes from early dark matter peaks* 2006, *MNRAS*, 368, 563.
- B. Moore, S. Ghigna, F. Governato, G. Lake, T. Quinn, J. Stadel, & P. Tozzi. *Dark Matter Substructure within Galactic Halos* 1999, *ApJ*, 524, L19.
- B. Moore, F. Governato, T. Quinn, J. Stadel, & G. Lake. *Resolving the Structure of Cold Dark Matter Halos* 1998, *ApJ*, 499, L5+.
- B. Moore, S. Kazantzidis, J. Diemand, & J. Stadel. *The origin and tidal evolution of cuspy triaxial haloes* 2004, *MNRAS*, 354, 522.
- T. Naab & A. Burkert. *The Formation of Disks in Elliptical Galaxies* 2001, *ApJ*, 555, L91.
- T. Naab & A. Burkert. *Statistical Properties of Collisionless Equal- and Unequal-Mass Merger Remnants of Disk Galaxies* 2003, *ApJ*, 597, 893.
- J. F. Navarro, V. R. Eke, & C. S. Frenk. *The cores of dwarf galaxy haloes* 1996, *MNRAS*, 283, L72.
- J. F. Navarro, C. S. Frenk, & S. D. M. White. *A Universal Density Profile from Hierarchical Clustering* 1997, *ApJ*, 490, 493.
- J. F. Navarro, A. Helmi, & K. C. Freeman. *The Extragalactic Origin of the Arcturus Group* 2004, *ApJ*, 601, L43.

-
- E. Opik. *An estimate of the distance of the Andromeda Nebula*. 1922, ApJ, 55, 406.
- J. Peñarrubia, A. Just, & P. Kroupa. *Dynamical friction in flattened systems: a numerical test of Binney's approach* 2004, MNRAS, 349, 747.
- J. Peñarrubia, P. Kroupa, & C. M. Boily. *Satellite decay in flattened dark matter haloes* 2002, MNRAS, 333, 779.
- S. Perlmutter, G. Aldering, G. Goldhaber, R. A. Knop, P. Nugent, P. G. Castro, S. Deustua, S. Fabbro, et al. *Measurements of Omega and Lambda from 42 High-Redshift Supernovae* 1999, ApJ, 517, 565.
- D. Pfenniger & D. Friedli. *Computational issues connected with 3D N-body simulations* 1993, A&A, 270, 561.
- C. Power, J. F. Navarro, A. Jenkins, C. S. Frenk, S. D. M. White, V. Springel, J. Stadel, & T. Quinn. *The inner structure of Λ CDM haloes - I. A numerical convergence study* 2003, MNRAS, 338, 14.
- W. H. Press & P. Schechter. *Formation of Galaxies and Clusters of Galaxies by Self-Similar Gravitational Condensation* 1974, ApJ, 187, 425.
- P. J. Quinn, L. Hernquist, & D. P. Fullagar. *Heating of galactic disks by mergers* 1993, ApJ, 403, 74.
- P. J. Quinn, J. K. Salmon, & W. H. Zurek. *Primordial density fluctuations and the structure of galactic haloes* 1986, Nature, 322, 329.
- J. I. Read & G. Gilmore. *Can supermassive black holes alter cold dark matter cusps through accretion?* 2003, MNRAS, 339, 949.
- W. H. Richardson. *Bayesian-Based Iterative Method of Image Restoration* 1972, Journal of the Optical Society of America, 62, 55.
- M. Ricotti & N. Y. Gnedin. *Formation Histories of Dwarf Galaxies in the Local Group* 2005, ApJ, 629, 259.
- A. G. Riess, A. V. Filippenko, P. Challis, A. Clocchiatti, A. Diercks, P. M. Garnavich, R. L. Gilliland, C. J. Hogan, et al. *Observational Evidence from Supernovae for an Accelerating Universe and a Cosmological Constant* 1998, AJ, 116, 1009.
- V. C. Rubin, W. K. Ford, Jr., K. M. Strom, S. E. Strom, & W. Romanishin. *Extended rotation curves of high-luminosity spiral galaxies. II - The anemic SA galaxy NGC 4378* 1978, ApJ, 224, 782.
-

-
- P. Salucci. *The constant-density region of the dark haloes of spiral galaxies* 2001, MNRAS, 320, L1.
- P. L. Schechter & J. E. Gunn. *NGC 2685 - Spindle or pancake* 1978, AJ, 83, 1360.
- M. Schwarzschild. *A numerical model for a triaxial stellar system in dynamical equilibrium* 1979, ApJ, 232, 236.
- F. Schweizer, B. C. Whitmore, & V. C. Rubin. *Colliding and merging galaxies. II - S0 galaxies with polar rings* 1983, AJ, 88, 909.
- J. A. Sellwood. *Bar-Halo Friction in Galaxies. III. Halo Density Changes* 2008, ApJ, 679, 379.
- J. D. Simon & M. Geha. *The Kinematics of the Ultra-faint Milky Way Satellites: Solving the Missing Satellite Problem* 2007, ApJ, 670, 313.
- A. Songaila, L. L. Cowie, C. J. Hogan, & M. Rugers. *Deuterium Abundance and Background Radiation Temperature in High Redshift Primordial Clouds* 1994, Nature, 368, 599.
- V. Springel. *The cosmological simulation code GADGET-2* 2005, MNRAS, 364, 1105.
- V. Springel, S. D. M. White, & L. Hernquist. *The shapes of simulated dark matter halos* 2004, In S. Ryder, D. Pisano, M. Walker, & K. Freeman, eds., *Dark Matter in Galaxies*, vol. 220 of *IAU Symposium*, 421 (2004).
- V. Springel, S. D. M. White, A. Jenkins, C. S. Frenk, N. Yoshida, L. Gao, J. Navarro, R. Thacker, et al. *Simulations of the formation, evolution and clustering of galaxies and quasars* 2005, Nature, 435, 629.
- P. Stäckel. 1890, Math. Ann., 35, 91.
- T. S. Statler. *Orbital decay in aspherical galaxies. II - Triaxial systems* 1991, ApJ, 375, 544.
- T. S. Statler, E. Emsellem, R. F. Peletier, & R. Bacon. *Long-lived triaxiality in the dynamically old elliptical galaxy NGC 4365: a limit on chaos and black hole mass* 2004, MNRAS, 353, 1.
- D. Syer & S. Tremaine. *Made-to-measure N-body systems* 1996, MNRAS, 282, 223.
- P. Teuben. *The Stellar Dynamics Toolbox NEMO* 1995, In R. A. Shaw, H. E. Payne, & J. J. E. Hayes, ed., *Astronomical Data Analysis Software and Systems IV*, vol. 77 of *Astronomical Society of the Pacific Conference Series*, 398 (1995).

-
- P. A. Thomas, J. M. Colberg, H. M. P. Couchman, G. P. Efstathiou, C. S. Frenk, A. R. Jenkins, A. H. Nelson, R. M. Hutchings, et al. *The structure of galaxy clusters in various cosmologies* 1998, MNRAS, 296, 1061.
- E. J. Tollerud, J. S. Bullock, L. E. Strigari, & B. Willman. *Hundreds of Milky Way Satellites? Luminosity Bias in the Satellite Luminosity Function* 2008, ApJ, 688, 277.
- S. Tremaine & M. D. Weinberg. *Dynamical friction in spherical systems* 1984, MNRAS, 209, 729.
- M. Valluri & D. Merritt. *Regular and Chaotic Dynamics of Triaxial Stellar Systems* 1998, ApJ, 506, 686.
- T. S. van Albada, J. N. Bahcall, K. Begeman, & R. Sancisi. *Distribution of dark matter in the spiral galaxy NGC 3198* 1985, ApJ, 295, 305.
- T. S. van Albada & J. H. van Gorkom. *Experimental Stellar Dynamics for Systems with Axial Symmetry* 1977, A&A, 54, 121.
- H. Velazquez & S. D. M. White. *Sinking satellites and the heating of galaxy discs* 1999, MNRAS, 304, 254.
- L. M. J. S. Volders. *Neutral hydrogen in M 33 and M 101* 1959, Bull. Astron. Inst. Netherlands, 14, 323.
- S. von Hoerner. *Die numerische Integration des n-Körper-Problemes für Sternhaufen. I* 1960, Zeitschrift für Astrophysik, 50, 184.
- I. R. Walker, J. C. Mihos, & L. Hernquist. *Quantifying the Fragility of Galactic Disks in Minor Mergers* 1996, ApJ, 460, 121.
- P. Wannier & G. T. Wrixon. *An Unusual High-Velocity Hydrogen Feature* 1972, ApJ, 173, L119+.
- M. S. Warren, P. J. Quinn, J. K. Salmon, & W. H. Zurek. *Dark halos formed via dissipationless collapse. I - Shapes and alignment of angular momentum* 1992, ApJ, 399, 405.
- M. L. Weil & L. Hernquist. *Global Properties of Multiple Merger Remnants* 1996, ApJ, 460, 101.
- M. D. Weinberg. *Orbital decay of satellite galaxies in spherical systems* 1986, ApJ, 300, 93.
- M. D. Weinberg. *Self-gravitating response of a spherical galaxy to sinking satellites* 1989, MNRAS, 239, 549.
-

-
- M. D. Weinberg & N. Katz. *The bar-halo interaction - I. From fundamental dynamics to revised N-body requirements* 2007, MNRAS, 375, 425.
- M. J. West, A. Dekel, & A. J. Oemler. *Profiles of clusters of galaxies - Cosmological scenarios versus observations* 1987, ApJ, 316, 1.
- S. D. M. White. *Simulations of merging galaxies* 1978, MNRAS, 184, 185.
- S. D. M. White, M. Davis, G. Efstathiou, & C. S. Frenk. *Galaxy distribution in a cold dark matter universe* 1987, Nature, 330, 451.
- S. D. M. White, C. S. Frenk, & M. Davis. *Clustering in a neutrino-dominated universe* 1983, ApJ, 274, L1.
- B. C. Whitmore. *The intrinsic orientation of S0 galaxies with polar rings* 1984, AJ, 89, 618.
- B. C. Whitmore, R. A. Lucas, D. B. McElroy, T. Y. Steiman-Cameron, P. D. Sackett, & R. P. Olling. *New observations and a photographic atlas of polar-ring galaxies* 1990, AJ, 100, 1489.
- B. C. Whitmore, D. B. McElroy, & F. Schweizer. *The shape of the dark halo in polar-ring galaxies* 1987, ApJ, 314, 439.
- M. I. Wilkinson & N. W. Evans. *The present and future mass of the Milky Way halo* 1999, MNRAS, 310, 645.
- T. Wright. *An original theory or new hypothesis of the universe* 1750. Facsimile reprint together with the first publication of "A theory of the Universe".
- R. F. G. Wyse, G. Gilmore, J. E. Norris, M. I. Wilkinson, J. T. Kleyna, A. Koch, N. W. Evans, & E. K. Grebel. *Further Evidence of a Merger Origin for the Thick Disk: Galactic Stars along Lines of Sight to Dwarf Spheroidal Galaxies* 2006, ApJ, 639, L13.
- D. G. York, J. Adelman, J. E. Anderson, Jr., S. F. Anderson, J. Annis, N. A. Bahcall, J. A. Bakken, R. Barkhouser, et al. *The Sloan Digital Sky Survey: Technical Summary* 2000, AJ, 120, 1579.
- A. R. Zentner & J. S. Bullock. *Halo Substructure and the Power Spectrum* 2003, ApJ, 598, 49.
- H. Zhao, M. G. Haehnelt, & M. J. Rees. *Feeding black holes at galactic centres by capture from isothermal cusps* 2002, New Astronomy, 7, 385.
- F. Zwicky. *Die Rotverschiebung von extragalaktischen Nebeln* 1933, Helvetica Physica Acta, 6, 110.
-

F. Zwicky. *On the Masses of Nebulae and of Clusters of Nebulae* 1937, ApJ, 86, 217.